REPORT DOCUMENTATION PAGE

Form Approved OMB NO. 0704-0188

1. REPORT DATE (DD-MM-YYYY)	2. REPORT TYPE	3. DATES COVERED (From - To)
06-04-2009	Final Report	1-Mar-2005 - 31-Aug-2008

4. TITLE AND SUBTITLE	5a. CONTRACT NUMBER
Micromechanics of Damage Accumulation in Micro- and Nano-Scale Laminates for Microelectromechanical Systems	W911NF-05-1-0064
	5b. GRANT NUMBER
	5c. PROGRAM ELEMENT NUMBER
	611102

6. AUTHORS	5d. PROJECT NUMBER
Christopher L. Muhlstein	5e. TASK NUMBER
	5f. WORK UNIT NUMBER

7. PERFORMING ORGANIZATION NAMES AND ADDRESSES	8. PERFORMING ORGANIZATION REPORT NUMBER
Pennsylvania State University Office of Sponsored Programs The Pennsylvania State University University Park, PA 16802 -	

9. SPONSORING/MONITORING AGENCY NAME(S) AND ADDRESS(ES)	10. SPONSOR/MONITOR'S ACRONYM(S)
U.S. Army Research Office P.O. Box 12211 Research Triangle Park, NC 27709-2211	ARO
	11. SPONSOR/MONITOR'S REPORT NUMBER(S)
	48355-EG.1

12. DISTRIBUTION AVAILIBILITY STATEMENT

Approved for public release; Distribution Unlimited

13. SUPPLEMENTARY NOTES

The views, opinions and/or findings contained in this report are those of the author(s) and should not contrued as an official Department of the Army position, policy or decision, unless so designated by other documentation.

14. ABSTRACT

In this program we used a combination of microscale mechanical testing methods and nanoindentation to ascertain the deformation, fracture, and fatigue properties of the materials. A variety of materials characterization tools were then used to establish the chemistry and structure of the films. Tis study has revealed that the stability of nanograined metals, especially in the presence of cyclic loading, is poor in comparison to coarser (micron-scale) grained materials. Moreover, the future of microelectromechanical systems that contain nanograined noble metals

15. SUBJECT TERMS

MEMS, Fatigue, Fracture, Composites

16. SECURITY CLASSIFICATION OF:			17. LIMITATION OF ABSTRACT	15. NUMBER OF PAGES	19a. NAME OF RESPONSIBLE PERSON
a. REPORT	b. ABSTRACT	c. THIS PAGE	SAR		Christopher Muhlstein
U	U	U			19b. TELEPHONE NUMBER
					814-865-1523

PENNSTATE

1 8 5 5

Department of Material Science and Engineering

College of Earth and Mineral Sciences

The Pennsylvania State University

University Park, PA 16802

File: 48355EG Muhlstein Final Report SUBMITTED.doc

Micromechanics of Damage Accumulation in Micro- and Nano-Scale Laminates for Microelectromechanical Systems

Christopher L. Muhlstein

Department of Materials Science and Engineering and The Materials Research Institute
The Pennsylvania State University, University Park, PA
202B Steidle Building, University Park, PA 16802;
phone: 814-865-1523; fax: 814-865-2917;
email: clm28@psu.edu

Foreward

The experimental mechanical behavior research in this program was driven by the needs of engineers at the Army Research Laboratories at Adelphi, MD to understand the properties and limitations of the materials used in the next generation of radio frequency (RF) switches. These switches are based on microelectromechanical systems (MEMS) manufactured using a state-of-the-art lead-zirconate-titanate (PZT) processing strategy. While devices have been fabricated, the mechanical properties of the individual layers (SiO_2, PZT, Au, and Pt) and their performance limitations were unknown. Similarly, the response of the multilayer, nanocomposite system and its relationship to the individual layer properties was unclear. In this program we used a combination of microscale mechanical testing methods and nanoindentation to ascertain the deformation, fracture, and fatigue properties of the materials. A variety of materials characterization tools were then used to establish the chemistry and structure of the films. Given the limited availability of specimens, our attention has been focused on the behavior of platinum thin films, although a limited number of experiments have been performed on Au-SiO_2 and Au-PZT-Pt-SiO_2 composite laminates. This study has revealed that the stability of nanograined metals, especially in the presence of cyclic loading, is poor in comparison to coarser (micron-scale) grained materials. Moreover, the future of microelectromechanical systems that contain nanograined noble metals and their long-term durability hinges on a thorough understanding of these phenomena and strategies to mitigate the degradation. Significant, additional studies will be required to mitigate this threat to the performance of MEMS in critical defense applications.

This program supported the research activities of two M.S. graduate (R.A. Meirom and A.L. Romasco) and one undergraduate (D. Hartwich) theses, and this report summarizes the more notable aspects of those efforts. The following sections of the report detail the methods and results. In the interest of brevity, the key findings, publications (1 published, 2 submitted, and 2 in preparation), presentations (12 total), and impact on the U.S. Army are summarized below.

Key Findings

1.   The unusual mechanical behavior of the films manufactured at the Army Research Laboratory (Adelphi, MD) is a byproduct of their nanoscale grain morphology and not contamination. The platinum thin films consist of (111) oriented columnar grains roughly 25-40 nm in diameter. High-resolution TEM established that the films are fully dense and no interphase regions between the grains were observed. Energy dispersive spectrometry

(EDS), electron energy loss spectrometry (EELS) and secondary ion mass spectrometry (SIMS) of the film confirmed that the films are contaminant-free

2. The films have a high strength (ultimate tensile strength ~3.4 GPa) that is correlated with the fine grain morphology.

3. The platinum films were found to have regions where the reduced modulus (~181 GPa) was low compared to what would be expected based on anisotropic elasticity and indentation theories (~211 GPa). While the origins of this behavior are still unclear, it is apparent that the low elastic moduli of thin films measured during nanoindentation are not a result of shortfalls in the experimental technique.

4. Fatigue tests conducted in laboratory air (22±2°C) established that the nanograined platinum films have an extremely limited range of stable fatigue crack growth (< 2 MPa √m), and a least squares curve fit of the data to a power law relationship between the fatigue crack growth rate da/dN and the applied stress intensity factor range, ΔK, (i.e., $da/dN = C(\Delta K)^m$) provided a large power law exponent, m, of ~10.5. This power law exponent of the nanocrystalline platinum is significantly different from its polycrystalline value of ~3.5, and means that the nanocrystalline platinum's fatigue crack growth rate behavior is similar to micrograined ceramic or ordered intermetallic materials.

5. The limited resistance to fatigue crack growth of the platinum films is accompanied by a 10-fold reduction in fracture toughness (3.45 MPa √m to 4.88 MPa √m) when compared to the bulk form of the material (K_q = 33.1 MPa √m) [1].

6. While the fatigue crack growth behavior of the platinum films was reminiscent of extrinsically toughened bulk materials (i.e., brittle ceramics and ordered intermetallics), fatigue crack closure was not observed. Therefore, the underlying mechanism of fatigue crack growth is inherently different.

7. Scanning electron microscopy of the failure surfaces of the fatigue specimens revealed that the fatigue crack path exhibited discrete transitions between inter- and transgranular propagation mechanisms as the crack accelerated. Combined with the orientation of the fast fracture failure surfaces (inclined at 45° to the loading axis), dislocation motion is believed to play a key role in the crack advance mechanism.

Publications

1.	Meirom, R.A., Clark, T., Polcawich, R., Pulskamp, J., Dubey, M., and Muhlstein, C.L., "Velocity Dependent Fatigue Crack Growth in Nanograined Pt Films." *Physical Review Letters*, 2008. 101: 85503(4).

2.	Romasco, A.L., Friedman, L.H., Fang, L., Meirom, R.A., Clark, A., Polcawich, R., Pulskamp, J., Dubey, M., and Muhlstein, C.L., "Practical Implications of Instrument Displacement Drift during Force-Controlled Nanoindentation." *Journal of Testing and Evaluation*, 2008: submitted.

3.	Romasco, A.L., Friedman, L.H., Fang, L., Meirom, R.A., Clark, T.C., Polcawich, R., Pulskamp, J., Dubey, M., and Muhlstein, C.L., "Deformation Behavior of Nanograined Platinum Films." *Thin Solid Films*, 2008: submitted.

4.	Meirom, R.A., Alsem, D.H., Clark, T., Polcawich, R., Pulskamp, J., Dubey, M., and Muhlstein, C.L., "Fatigue Crack Growth via Nanograin Coarsening and Dislocation Slip in Nanograined Platinum Films." In preparation for submission to *Acta Materialia*.

5.	Meirom, R.A., Hartwich, D., Clark, T., Polcawich, R., Pulskamp, J., Dubey, M., and Muhlstein, C.L., "Complaince eEvolution in Au-SiO2 Nanolaminate Composites during Fatigue Crack Growth." In preparation for submission to the *Journal of Microelectromechanical Systems*.

Presentations

1.	Muhlstein, C.L.*, "Micro- and Nanomechanical Behavior of Materials (Invited)," NIST, Gathersburgh, MD, 2008.

2.	Muhlstein, C.L.*, Pierron, O.N., Zapata, M.C., and Meirom, R.A., "Deformation and Fatigue of Face-Centered and Diamond Cubic Structural Films (Keynote)," 4th International Conference on Very High Cycle Fatigue (VHCF-4), Ann Arbor, MI, 2007.

3.	Muhlstein, C.L.*, Collins, J.G., Meirom, R.A., Romasco, A.L., Clark, A., Polcawich, R., Pulskamp, J., Dubey, M. and Minor, A., "Deformation and Fracture of Structural Films for Microelectromechanical Systems (Invited)," Materials Processing Defects 5, Ithaca, NY, 2007.

4. Muhlstein, C.L.*, Meirom, R.A., Romasco, A.L., Clark, A., Polcawich, R., Pulskamp, J., and Dubey, M., "Deformation and Fatigue of Platinum Structural Films in Laboratory Air," 17th U.S. Army Symposium on Solid Mechanics, Baltimore, MD, 2007.

5. Romasco, A.L.*, Bintachitt, P., Fang, L., Polcawich, R., Pulskamp, J., Dubey, M., Trolier-McKinstry, S., Friedman, L., and Muhlstein,C.L., "Nanomechanical Properties of Piezoelectric Actuator Materials," TMS Materials Science and Technology (MS&T) Conference and Exhibition, Detroit, MI, 2007

6. Muhlstein, C.L.*, "Deformation and Fatigue Mechanisms of Structural Films (Invited)," The Penn State Electro Optics Center, Freepoint, PA, 2007.

7. Muhlstein, C.L.*, "Opportunities in Ultra-Thin Structural Films (Invited)," ARL/ARO Workshop on "Fundamental of Robust and Reliable Nano/MEMS Structures and Devices", 2007.

8. Muhlstein, C.L.*, Meirom, R.A., and Romasco, A.L., "Deformation and Fatigue of Platinum Structural Filims (Invited)," Mini-workshop on MEMS/NEMS: Characterization and Modeling, Sensor and Electron Devices Directorate, ARL, Adelphi, MD, 2006.

9. Muhlstein, C.L.*, "Deformation and Fatigue Mechanisms of Structural Films (Invited)," 2nd Workshop on Characterization of Materials for MEMS/MST Devices, Tokyo Institute of Technology, Tokyo, Japan, 2006.

10. Muhlstein, C.L. *, "Performance and Durability of Materials in Small Structures (Invited)," ASM Chapter Meeting (The Pennsylvania State University), 2005

11. Muhlstein, C.L.*, "Micromechanics of Damage Accumulation in Micro- and Nano-Scale Laminates for Microelectromechanical Systems (Invited)," Army Research Laboratory Workshop in Dynamic Failure of MEMS Devices and Thin Films, Adelphi, MD, 2004.

12. Muhlstein, C.L.*, "Reliability of MEMS (Invited)," in MEMS for Military Applications sponsored by the Solid Mechanics and Structures and Dynamics Branches of the Engineering Sciences Division of the U.S. Army Research Office (ARO), June 22-24, 2004.

Impact on U.S. Army

The impact of this program on U.S. Army personnel and activities has been both direct and indirect. We have directly exchanged information with personnel at the Adelphi research labs on a number of topics including revisions to sample design, data on chemistry (purity) and grain morphology (unknown features for the people at Adelphi) of their films, and the stability and durability of their structural films. Additionally, a student (R. Kirkpatrick) from the Muhlstein research group at The Pennsylvania State University Participation interviewed for a post doctoral position at the Army Research Laboratory facility at Adelphi, MD.

Table of Contents

1   Materials and Methods

Films from a multilayer, PZT micromachining process were evaluated with a variety of structural, chemical, and mechanical characterization strategies. A large portion of this program was focused on the deformation, fracture, and fatigue degradation behavior of pure Pt films. The free-standing, 430 nm thick, Pt films on top of a 20 nm Ti adhesion layer were produced in the Army Research Laboratories. This section will detail the fabrication techniques employed by Ronald Polcawich (ARL at Adelphi, MD) for the creation of the free-standing specimens used in this study.

1.1   Film Deposition, Structure, and Chemistry

1.1.1   Deposition

The samples tested in this study were fabricated by Ron Polcawhich at the Army Research Laboratory's Specialty Electronic Materials and Sensors Cleanroom Facility in Adelphi, MD. Fabrication began with a 100mm diameter single crystal silicon wafer (100) substrate with a resistivity of 1 – 30 Ohm-cm. All films were sputtered onto the substrate using a Unaxis Clusterline 200 deposition system configured with individual chambers for Ti and Pt deposition. The first layer deposited onto the silicon substrate was a 20nm thick titanium layer. This layer served as an adhesive layer for the platinum layer to follow. The second layer deposited at the conclusion of the titanium sputtering was the 430nm platinum layer. The deposition parameters are listed in Table 1-1. All depositions occurred at 50ºC in order to prevent the formation of platinum silicides.

In order to pattern the platinum films into the specimen design, a thin film resist (Clariant AZ5200) was first spun onto the entirety of the wafer surface and exposed using contact lithography with a Karl-Suss MA/BA-6 aligner. After exposure and resulting resist development, the wafer underwent a two minute oxygen descum process in a Metroline ML4 asher to remove any residual organics. Following, the resist was cured at 220ºC along with a dose of ultra-violent radiation in an Axcellis Photostabilizer. The UV cure process improves the photoresist resistance to ion-bombardment damage during the argon ion-milling procedure. After the resist has been cured, the undesired regions of platinum were removed with argon ion-milling using a Commonwealth ion-mill system (see Table 1-2 for plasma parameters).

Each tensile specimen die had 6 individual specimens. A Disco Dicing Saw was used to separate each die on the wafer. With the wafer coated in photoresist, die separation was done using a

Disco Dicing Saw with a 150 μm wide blade using a 3 mm/s feed rate. Following the wafer sawing process, individual die were cleaned using a series of solutions: acetone, methanol, isopropyl alcohol, and deionized water. Clean die were dried using blowing nitrogen.

Next, the dry die were placed into a Xactix Xetch system to facilitate the release of the tensile specimens by removing the silicon from underneath of the specimens. In this process, 2 Torr of XeF_2 was combined with 20 T of N_2 and subsequently transferred to the wafer chamber for a 20 second etch. This process was repeated until the specimens were released from the substrate and supported by the tethers in the specimen gripping region. The packed die were then placed into individual Gel-pak[TM] carriers and delivered by courier to Pennsylvania State University for testing.

Table 1-1: Deposition conditions for all sputtered metals

Material	Ar (sccm)	O$_2$ (sccm)	Pressure (mTorr)	Temp (°C)	Power (W)
Ti	30	0	5	50	1000
Pt	50	0	5	50	500

Table 1-2: Parameters used for ion-milling Pt thin films

Item	Voltage (V)	Current (mA)
Cathode	11.5	14
Discharge	40	2.5
Beam	500	300
Accelerator	100	34
Neutralizer		500
Bias	36	
Ar (sccm)	10	10
Operating Pressure (Torr)	7×10^{-4}	7×10^{-4}
Chuck rotation (rpm)	5	5

Table 1-3: Parameters for oxygen plasma processes

Description	O_2 (sccm)	Pressure (mTorr)	Temp (°C)	Power (W)
Descum	200	525	~70	200
Resist removal (ash)	500	1000	~160	400

1.2   Film Roughness, Structure, and Chemistry

Each specimen arriving to Penn State was individually examined under an optical microscope and inspected for flaws such as surface cracks, bend contours, plastic deformation such as dents or crinkles, malformed or broken samples, improperly released samples, and surface debris. This optical characterization however, represents only a small fraction of the characterization of these specimens. Atomic Force Microscopy (AFM) was used to analyze surface roughness, X-ray diffraction (XRD) was used to determine texture, transmission electron microscopy (TEM) to determine grain and defect morphologies, and energy dispersive spectroscopy (EDS), electron energy loss spectroscopy (EELS) and secondary ion mass spectrometry (SIMS) to quantify the chemistry of the films.

1.2.1   Film Roughness

Most samples exhibited a clean and visibly flat surface devoid of flaws such as surface cracks, and were relatively flat. An atomic force microscopy study was conducted on the nanocrystalline platinum samples to gauge their roughness. The study was conducted using a Dimension 3100 atomic force microscope produced by Veeco, and using tips produced by Nanosensors. Further instrument parameters which were used to obtain the results are listed in Table 1-4. One studied sample exhibited a root mean square (RMS) value of 2.615 nm over a 1 μm2 area (Figure 1-1). As all samples came from the same chip and were deposited at the same time, the surface of all platinum samples is assumed to be nominally flat to about the same value. The features seen on the top layer of the platinum sample were measured using point to point comparison using Photoshop® CS2, a graphics editor from Adobe Systems, and found to be approximately 10nm in size. Analysis of the interior of the film detailed in a future section will show that the average size of a grain on the interior of the film is closer to 35nm, and thus, the features on the surface of the film are not indicative of the grain size in the interior.

Table 1-4: Atomic Force Microscopy Running Parameters

| Mode	Scan Size	Aspect Ratio	Scan Rate	Samples/ Line	Integral Gain	Proportional Gain
Tapping	1μm	1:1	1 Hz	512	.4	1.0
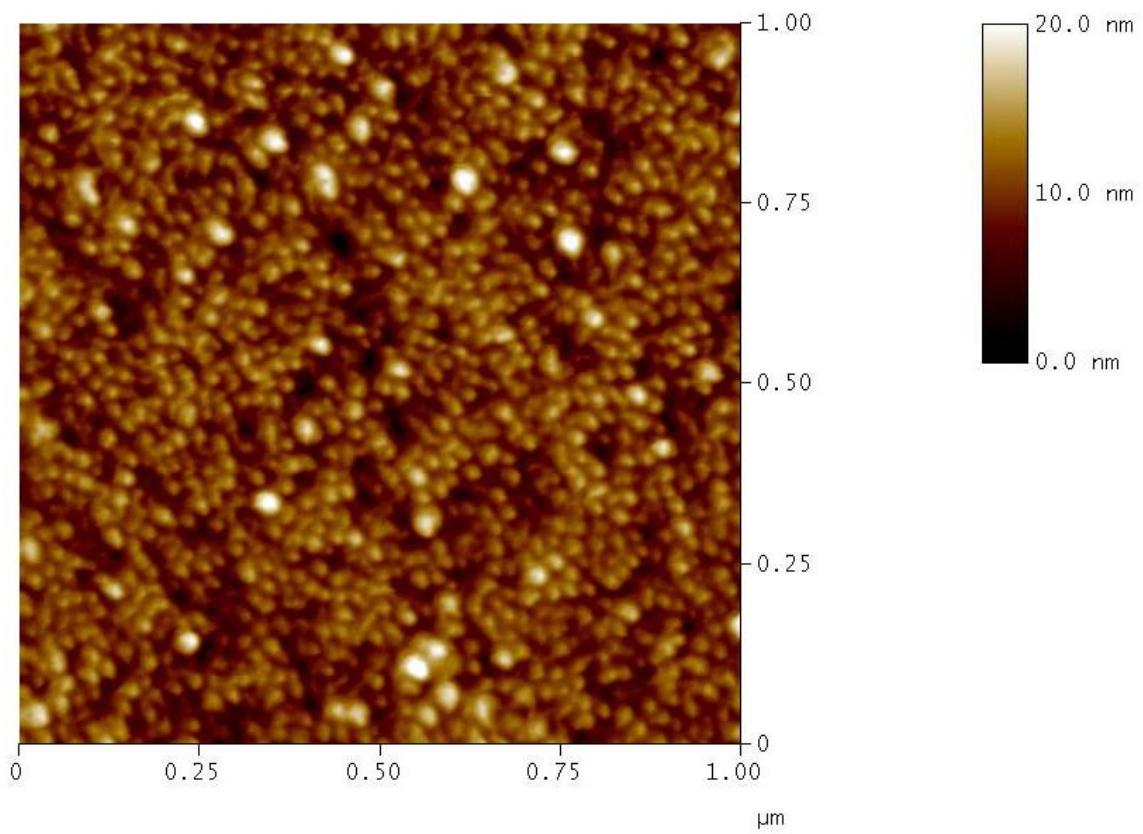
Figure 1-1: Atomic force microscope topographic map of the surface of a platinum sample. This surface has an RMS of 2.615nm and is optically pristine. The surface features shown were measured to be ~10nm and are not indicative of the grain size in the interior of the film.

1.2.2 Film Structure and Chemistry

X-ray diffraction (XRD) was used to characterize the texture of the Pt film. A theta-theta scan (10 to 120º, step size 0.02º, count time of 2.5 seconds) using a quartz sample holder (cut 6 degrees of the c-axis so as not to produce any peaks in the measured range) was conducted using a Scintag model X2 with copper Kα source. The resulting spectra shown in Figure 1-2 overlays both the theta-theta scan (shown in black) and the grazing angle scan (shown in blue). At the bottom of the spectrum are predicted peak locations for platinum (marked in red), and predicted silicon peaks (blue). Results indicated the platinum film to be primarily (111) oriented (having dominant (111) and (222) peaks) with some (311) and (331) orientation. The silicon substrate is (100) oriented, and the thin, titanium seed layer could not be characterized with this method.
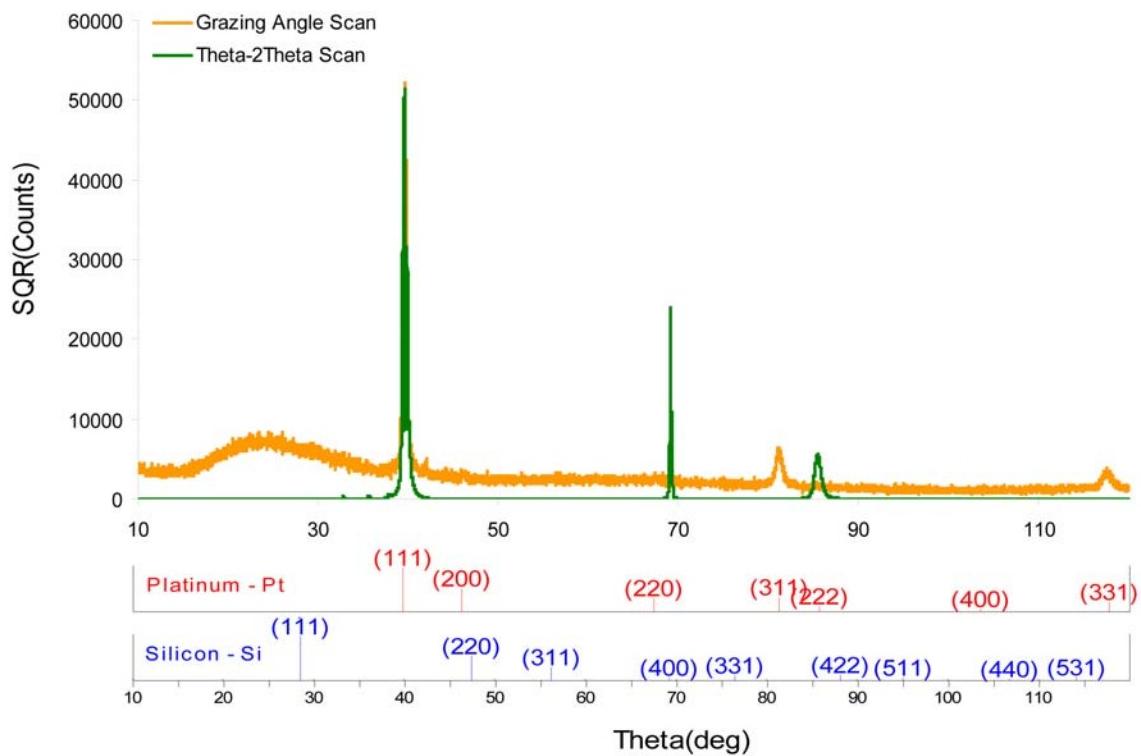

Figure 1-2: X-Ray Diffraction pattern of a theta-theta scan on the TiPt sample on a silicon substrate. This scan shows 3 primary peaks, two attributed to the (111) orientation of the platinum grains, and 1 attributed to the (100) orientation of the silicon wafer.

The nanostructure and chemistry of the Pt films were evaluated with the help of Trevor Clark (a staff member at The Pennsylvania State University), using two 200kV JEOL TEM that were outfitted with energy dispersive spectrometers (EDS): 1) a JEM 2010F, equipped with a field-emission electron source, STEM unit and Gatan Enfina electron energy loss spectrometer (EELS) and 2) a JEM 2010 equipped with a LaB_6 emitter. Electron transparent cross-sections of the film were produced with assistance from Josh Meier by using conventional mechanical and ion milling techniques in which sections were polished to approximately 10 μm thickness using a succession of diamond lapping film ranging in grit from 30 to 1 μm. After adhering the polished section to a copper TEM grid, a Gatan model 691 precision ion milling system was used to perforate the film, creating a thickness gradient emanating radially such that areas nearest the hole were electron transparent, and samples furthest from the hole retained their full thickness. Samples were then plasma cleaned for 10 minutes prior to evaluation to minimize carbon contamination of exposed surfaces.

TEM analysis on areas which were not fully electron transparent confirmed a thickness of about 450 nm for the film (Figure 1-3). Analysis on electron transparent sections revealed a columnar grain structure with grains measured by point to point comparison to be roughly 25 to 40nm in diameter (Figure 1-4). Close inspection of platinum grain boundaries did not reveal any voiding or cracking (Figure 1-5). Diffraction patterns acquired at this magnification indicate a lattice spacing of 2.26nm, matching a (111) structure in the platinum film (Figure 1-6) [2].

The chemistry of the film was evaluated in the TEM with both EDS and EELS. EDS spectra were acquired for 1200 seconds in several grain boundary locations within the film. These scans were focused on identifying the grain boundary segregation of species such as Ti, Si, and their oxides and compounds in the nanograined Pt (Figure1-7). These scans found platinum to be the only element detected within grain boundaries, when sampled near and far from the titanium adhesion layer. EELS spectra were acquired in several locations in the platinum sample, including with grain boundaries. This technique identified titanium only within the region corresponding to the titanium adhesion layer. Silicon, carbon, oxygen, xenon and titanium were below detection limits when sampling within the platinum layer (Figure 1-8).
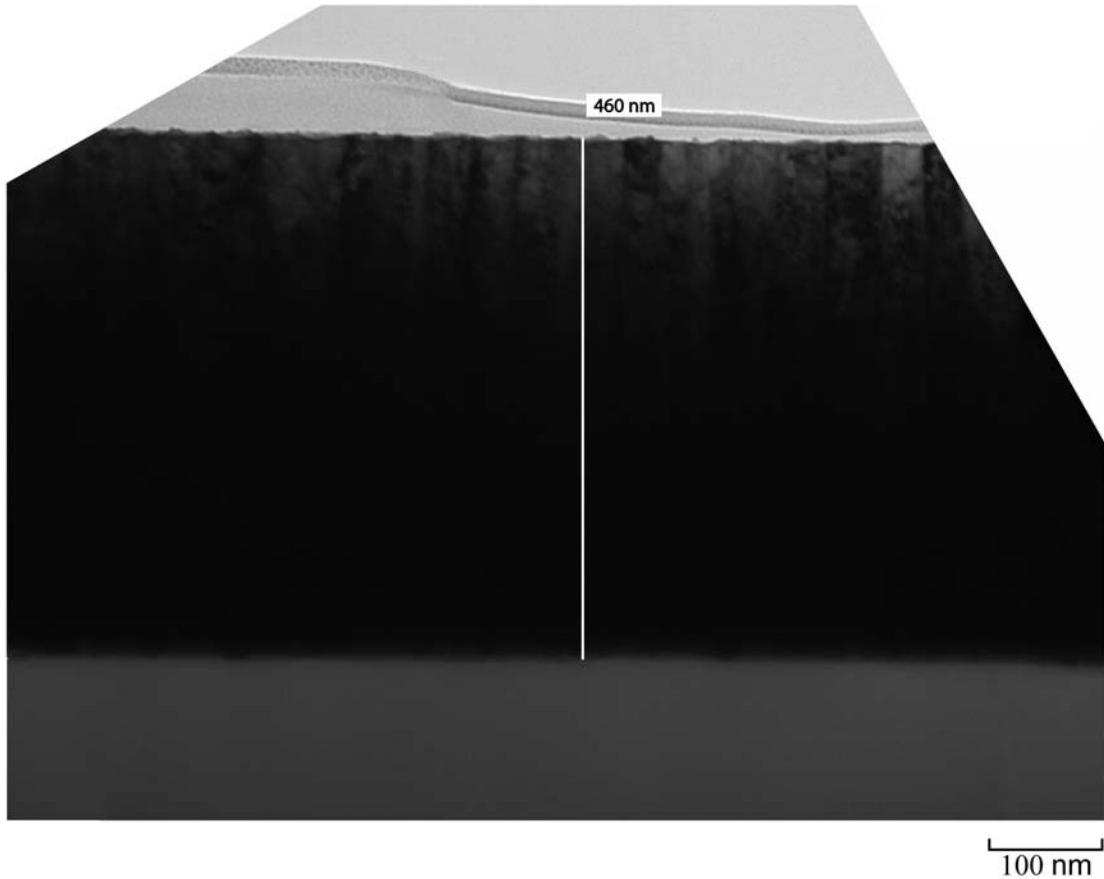
Figure 1-3: Transmission electron micrograph of pt sample which has not been thinned down. This micrograph shows the full thickness of the film. The layer at the top of the film is a residual epoxy used in the sample preparation.
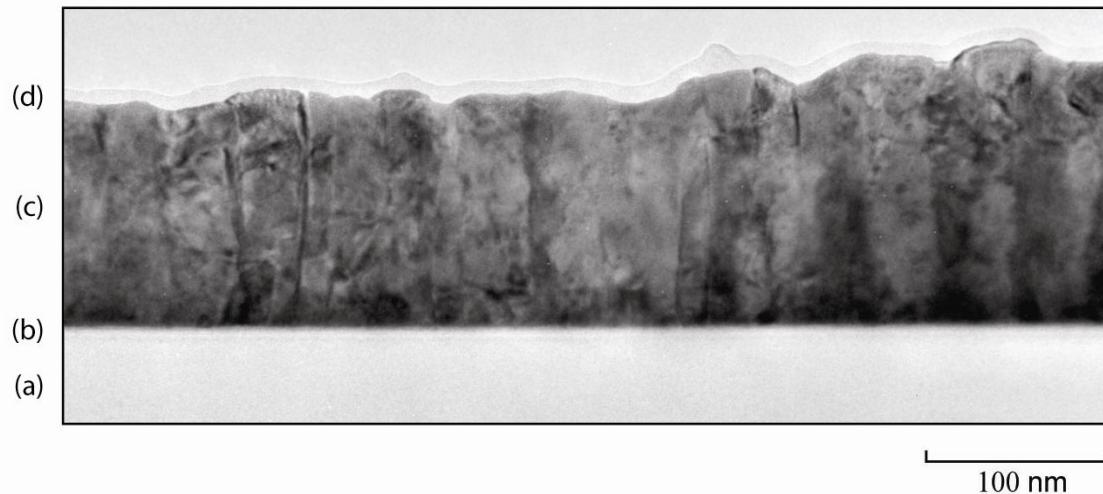
Figure 1-4: Transmission electron micrograph of a Pt sample on Si substrate that has been thinned down to electron-transparency (hence not showing full thickness). Sections (a) show the Si substrate, (b) the titanium adhesion layer, (c) the 25-40 nm diameter, nanoscale, columnar Pt grains and (d) an adsorbed oxygen layer from the thinning process.
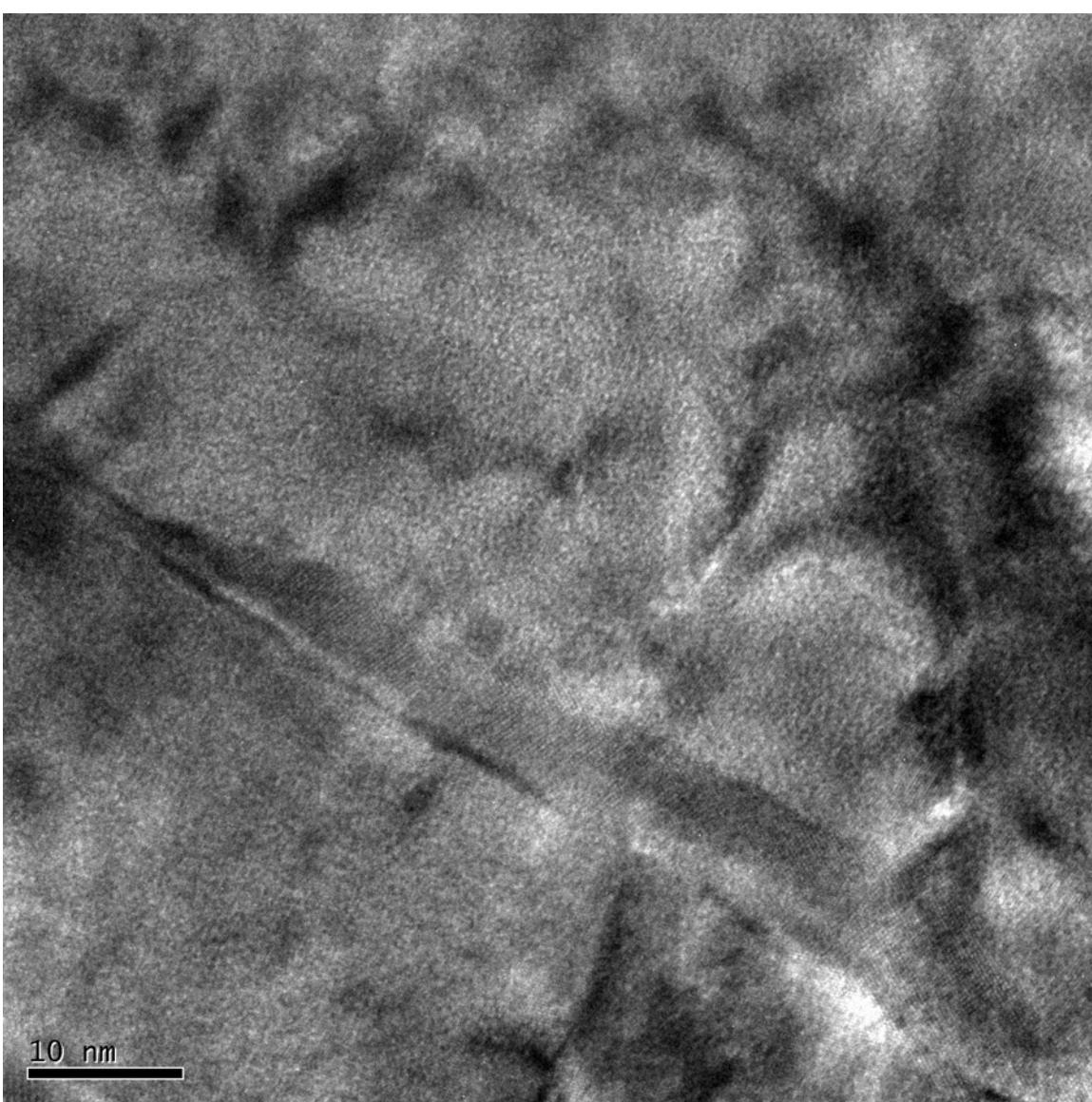
Figure 1-5: Transmission electron micrograph of a platinum grain boundary within a TiPt thin film. Lattice fringes can be seen nearest the grain boundary. No significant volume of voids can be seen.
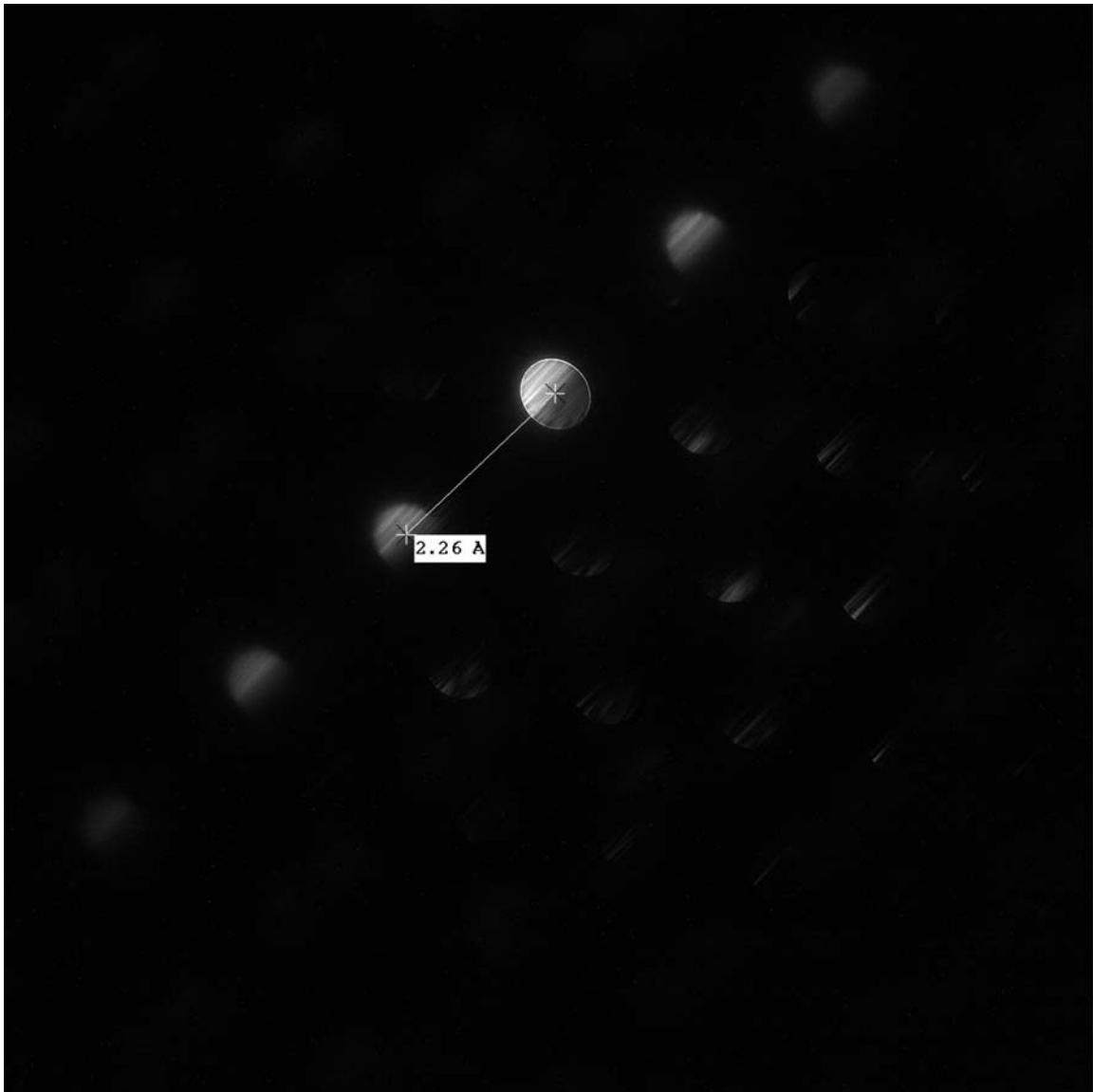
Figure 1-6: Platinum diffraction pattern produced in the TEM indicating a (111) structure in the platinum film.
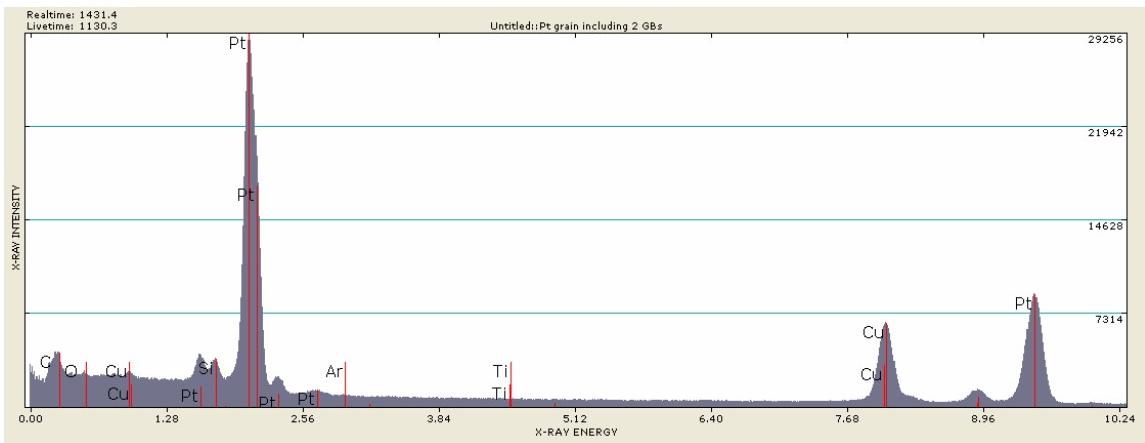
Figure 1-7: Energy dispersive spectrometry (EDS) of the film confirmed the presence of the Pt structural film and the Ti adhesion layer. Additional spectra collected within the grains, along grain boundaries, and near the Ti adhesion layer interface identified Pt as the only element present, within the 0.1 atomic % detectability limit of the techniques.
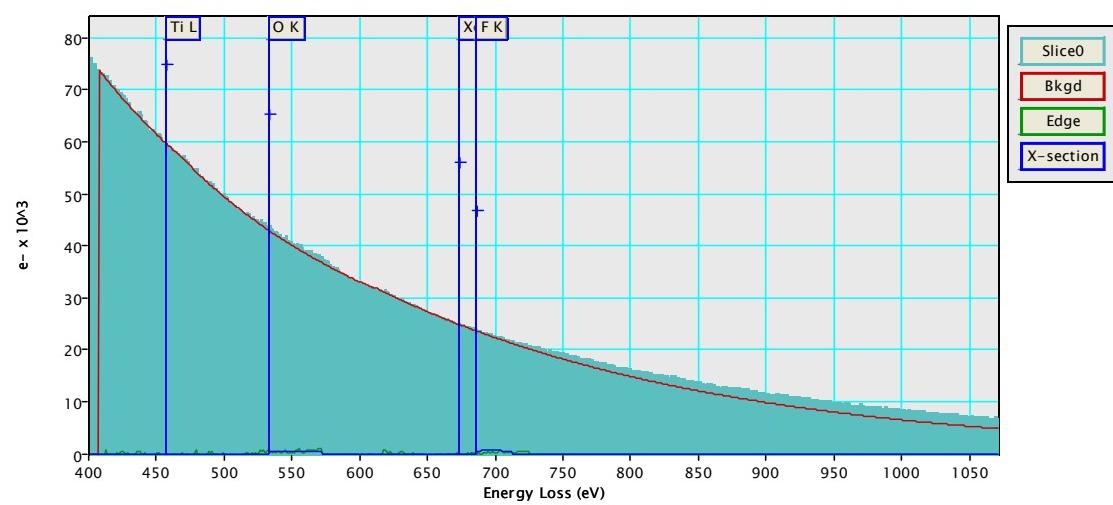
Figure 1-8: EELS Spectra of platinum grain boundary near the titanium adhesion layer. No titanium, xenon, oxygen or fluorine was detected.

Although EDS and EELS are both very accurate methods of analysis for detecting the presence of elements, secondary ion mass spectrometry (SIMS) has comparable resolution for trace elements, and has the distinct advantage of sampling the entirety of the film, whereas EDS and EELS are both localized measures. Platinum samples were sent Evans Analytical Group in East Windsor, NJ to acquire concentration depth profiles of all elements present within a section of film still adhered to the substrate. A Quadrupole Mass Spectrometer was used in two different runs such that both positive ions and negative ions could be evaluated (see Table 1-5 for parameters). Ions selected for SIMS analysis were based on their likelihood of being present. Xenon and fluorine were selected based on their use as an etchant, carbon and oxygen were selected due to the predominance in ambient environments.

Both positive (Figure 1-9) and negative (Figure 1-10) ion analysis showed that all measured elements were present at or near the detection limits of the instrument. From the surface, the initial 50 nm had erroneously high values of all measured quantities as a result of normalizing counts; this normalization was not complete until a certain number of counts was reached, resulting in an erroneous high contamination count near the surface which quickly stabilized, at a baseline value at around 50 nm. Between 50 and 400 nm, values of all measured species, carbon, fluorine, oxygen, titanium and xenon were steady or decreasing and were present at or below the detection limits of the instrument for the elements. The detection limit for each element is different, but varied between 10^{17} atoms per cm^3 and 10^{18} atoms per cm^3, equivalent to about 0.1 and .01 atomic percent. Although the titanium layer was first exposed at 430 nm, mass interference effects on other measured elements began to show around 400 nm. Although it is possible that some titanium has diffused into the platinum layer, or that the platinum layer is not as thick as predicted, the most likely explanation is that the crater associated with the destructive sputtering of the sampling was not uniformly flat causing some portion of the titanium layer to be exposed while still registering an average crater depth shallower than the minimum depth. Between 430 and 450 nm, titanium peaks, causing peaks in all elements due to mass interference, particularly in the negative ion scan. Below 450 nm, all elements but silicon quickly ebb. The sample to sample variation of concentration measurement of the SIMS analysis was reported to be approximately 20 percent. The instrument was calibrated against NIST traceable reference standards for silicon, and results for other materials are typically calibrated against consensus standards in those materials, however, no such standard exists for platinum.

Table 1-5: SIMS Sampling Parameters

Condition Number	1	2
Secondary Ion Polarity	Negative	Positive
Elements Monitored	C, O, F	Xe, Ti
Primary Ion Beam	Cs	Cs
Primary Ion Energy	4keV	4keV
Incident Angle	60°	60°
Oxygen Leak	No	No
Charge Neutralization	No	No
Surface Conductive Coating	None	None
Liquid Nitrogen Cold Trap	No	No
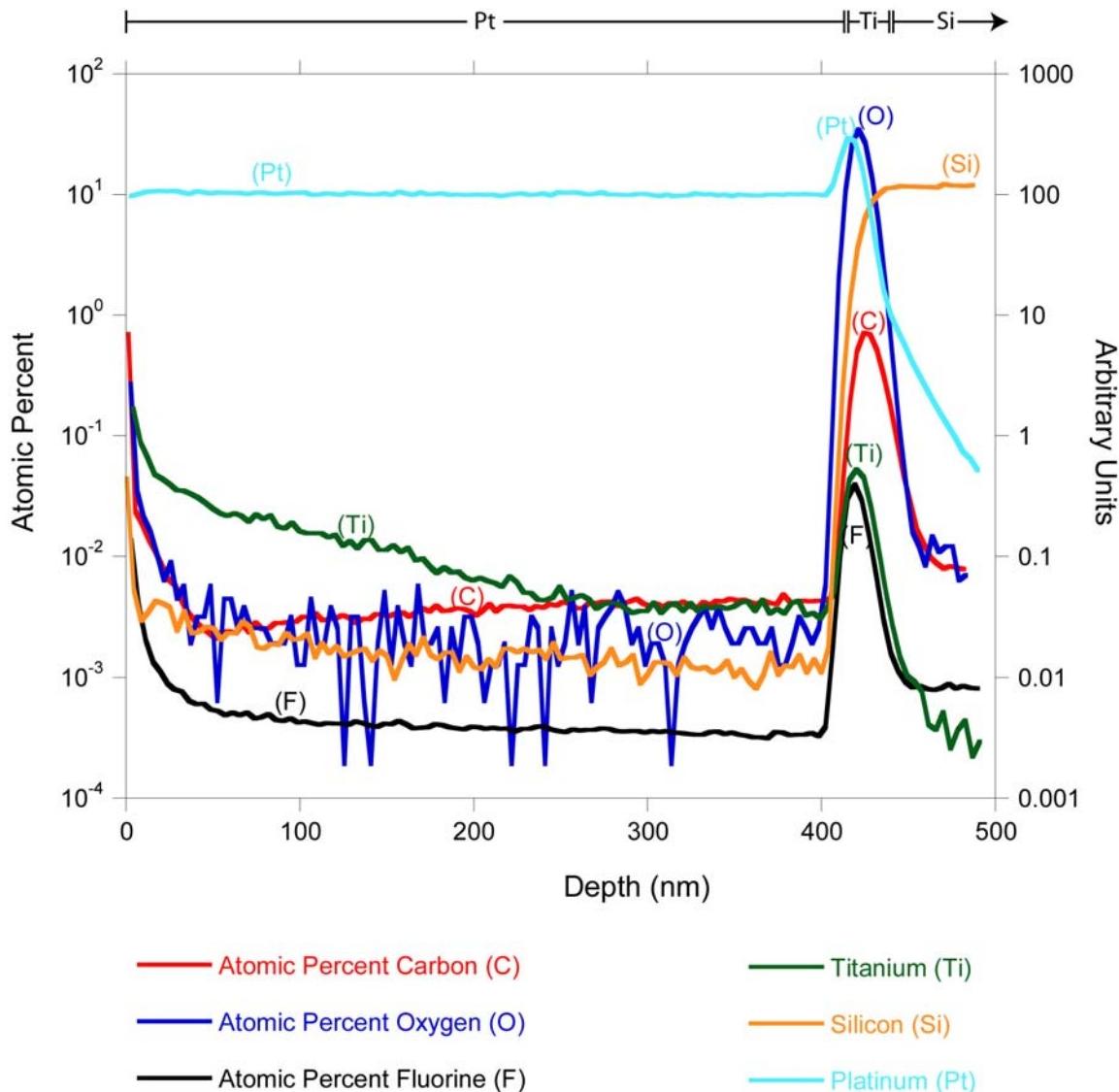
Figure 1-9: Negative ion analysis by SIMS is best for detection of carbon, fluorine and oxygen, although they are all influenced by the presence of titanium [3] – this effect is characterized by false peaks at around 440nm (the center of the titanium layer). These results confirm that carbon, fluorine and oxygen are only present at or around the detection limits of the instruments. Platinum, silicon and titanium are plotted on arbitrary units, normalized with respect to silicon counts.
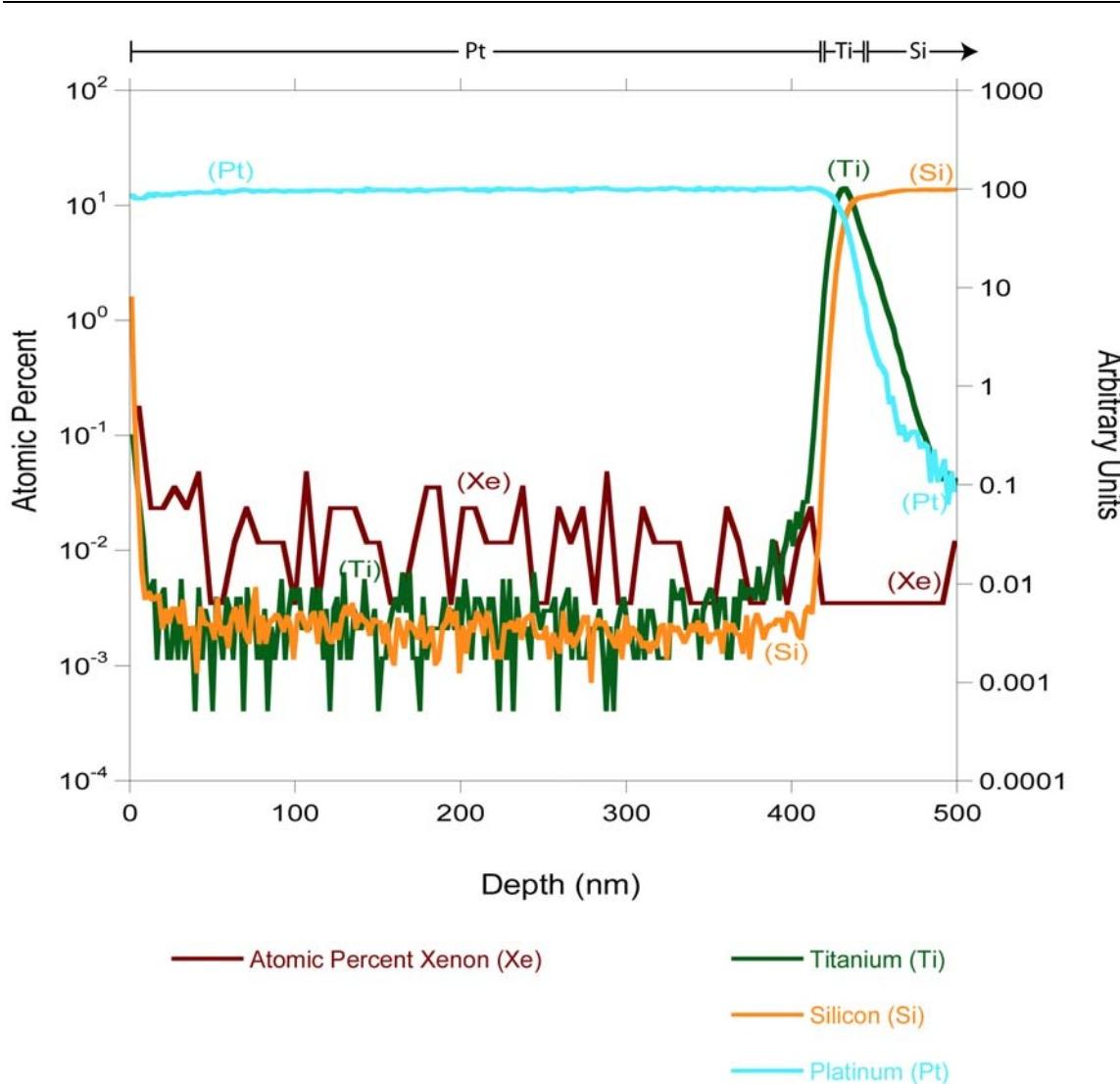
Figure 1-10: Positive ion analysis by SIMS is best for detection of titanium and xenon [3]. These results confirm that xenon is only present at or around the detection limits of the instruments within the platinum layer. Platinum, silicon and titanium are plotted on arbitrary units, normalized with respect to silicon counts.

1.2.3   Summary of Material System Characterization

Several characterization tools were used in order to evaluate the films used in this study. Using TEM, it was established the platinum films were 430nm of platinum on top of a 20 nm titanium layer. Using AFM, the top platinum layer was to found to have an RMS value of 2.615 nm. Using TEM and XRD, the platinum was found to be nanocrystalline, with columnar grains roughly 25 to 40nm with a primarily (111) orientation. EDS, EELS, and SIMS confirmed that the platinum films were free from contamination to the resolution of the instruments.

1.3   Mechanical Testing Specimen Geometry

The mechanical properties of the platinum films were investigated using sample geometry and testing methods that were established for uniaxial tension-tension of macroscopic specimens in ASTM E 647 [4]. The tensile and fatigue properties were measured using center cracked sheet specimens that were freestanding at one end and bound to a (100) single crystal silicon substrate at the other. Figure 1-11 shows a scanning electron microscope image of the sample, along with a close up of the gage section highlighting the notch. Gauge sections were 2 mm long, having 200, 160 and 100μm widths, and slots with semicircular ends which spanned 33% of the gauge widths and had a 3μm root radius. The thickness of the films was reported to be 480nm of platinum on top of a 20nm titanium adhesion layer, however, TEM, SIMS and cross-sectional scanning electron microscopy indicated the thickness of the film composite to be 450nm, and this value was used in all calculations.
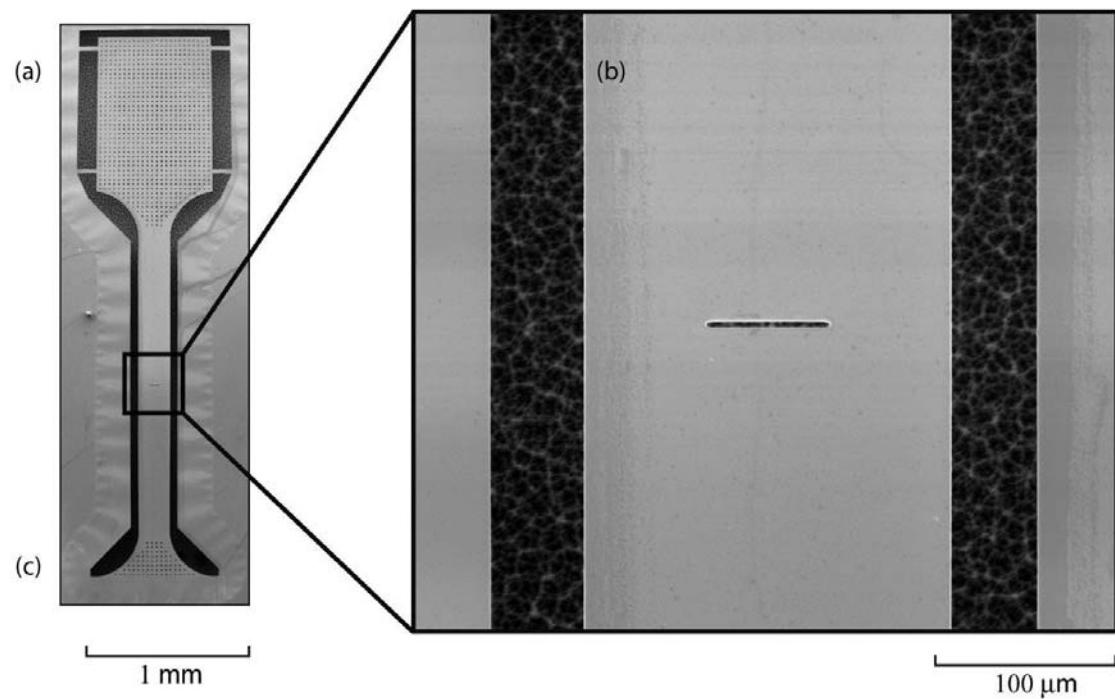
Figure 1-11: A scanning electron micrograph of a center-cracked sheet fatigue crack growth characterization specimen showing (a) the free standing grip section with tethers, (b) the free standing gauge section with slot, and (c) the 'anchor' portion attached to the substrate.

1.4   Mechanical Testing System

The testing system is comprised of three main parts: a displacement stage, a load cell, and a camera (Figure 1-12). Before a sample can be tested in either tension or fatigue, the specimen must be detached from the tethers binding it to the substrate, it must be gripped, and it must be loaded under controlled conditions. In all testing cases, the 4 tethers connecting the substrate to the film were broken prior to testing. In some cases, these tethers were broken prior to gripping the sample using a tungsten probe with a 20 μm tip diameter, and in others the sample was first gripped, and then the tethers were broken by the tensile forces applied to them by the slight motion of the specimen away from the substrate. This second method greatly reduced the number of samples damaged by tether breaking, or lost in the transfer between the probe station to the testing system. Details regarding which method was used, as well as several test-specific parameters are presented in Table 1-6.

The silicon chip containing the samples was adhered with double sided (Scotch™) tape to a piezoelectric translating stage (PI P620) providing a total of 250 μm of displacement with sub nanometer resolution, in turn mounted on a 3 axis stage capable of tilt, pitch and rotation (Newport PO80N). The displacement stage was controlled by a closed-loop external conditioning box (PI E-665) which allowed digital or manual control of the stage. A 200 μm diameter optical fiber or 20 μm tip diameter tungsten needle (see Table 1-6) was affixed to a gripping fixture, the head of an Icy Pentel 0.5 mm lead pencil for the fiber, and a pin-jack probe holder (American Technologies 745-SAI) for the needle. Initially, the optical fiber was used because it was thought that the transparency of the fiber would be conducive to curing regions of the glue underneath the fiber, however, it was discovered that the curing system was sufficiently powerful to cure all regions of the glue, even when using an opaque needle. The transition to the needle was also advantageous in creating a stiffer load train, and thus lowering system compliance. The gripping fixture was in turn connected to either a 10 gram load cell (Transducer Techniques GSO-10) capable of force measurements with 0.005 N resolution or a 50 gram load cell (Sensotec Model 31) capable of force measurements with 0.0005 N resolution (Table 1-6). This transition was made for the advantageous higher capacity and resolution of the second load cell. The load cell and attachments sit on top of two stages (Edmund Optics NT56-339, NT55-028) capable of three orthogonal displacements and rotation about the vertical axis. The sample was aligned with the grip system using all the available axes of freedom so that a uniaxial loading mode will result.

Initially, samples were mounted directly onto the flat surface of the displacement stage, i.e. at a 0° offset from the needle. Although this was thought to be ideal for the application of pure tensile forces, it was difficult attaching the fiber to the sample. The initial solution was to mount the fiber at an angle and owing to the high compliance of the fiber, the fiber and sample system would realign when stressed, thus bending the sample at the film/substrate hinge. Although this was not ideal, because no deformation was ever seen at this hinge, the results were still considered valid. However, when the transition was made to the needle, its holder did not allow for it to be mounted at an angle. As a solution to this problem, an adapter was developed so that chips could be mounted at a 10° offset from the needle. UV-adhesive glue (Dymax OP-24-REV-B) was applied to the tip the fiber or needle. It was then lowered on to the free-floating gripping region of the dog-bone. A hand held UV spot curing system (Electro-Lite ELC-410) was used for 2 minutes to completely cure the glue. The sample was then realigned by raising the sample to the point where it is flat, resulting in the ability to apply purely tensile forces.

A high resolution monochrome CCD digital camera (Pulnix TM-9701) connected to an image acquisition card (National Instruments NI PCI-1422) which sits on top of two stages (Newport m-562, Newport 813S) and damping rod (Newport 45) so that 5 axes of tilt and translation allowed the camera to be positioned perpendicular to the surface of the gage section of the sample. Long working distance Mitutoyo infinity-corrected long working distance lenses (Edmund Optics NT46), either 20× objectives having a resolution of 0.7 μm, or a 100× objectives having a resolution of 0.4 μm, were used in conjunction to the camera in order to image and record the region of interest (Table 1-6). The objective lenses were attached to the camera via an additional stage (PI P-725.2CD) which allowed vertical displacement of the objective lens using a signal sent from an external conditioning box (PI E-665). This attachment allowed the user to change the focus of the objectives whenever necessary without disturbing the system. An image of the region of interest was recorded for later calculation of the crack lengths during testing (Table 1-6). Coaxial illumination for the camera was provided by a variable intensity light source with fiber-optic guide (Dolan-Jenner DC950). The entire system was situated on top of a bench top vibration isolation system (Minus K BM-4).

The testing software was developed in LabView 7.0, with certain portions of code, primarily those developed for the control of the camera, developed by James Collins (The Pennsylvania State University). The program controlling tensile tests was based on sending voltage signals to the displacement stage's conditioning box at quick successive intervals. The conditioning box

used the voltage signals in order to determine a target displacement, and set the voltage required to do so in a closed loop format in real time. This process caused a smooth ramping of the displacement stage away from the load cell, effectively loading the sample in tension. The program was capable of accepting user input for ramp rate, and frequency of imaging. The program recorded load cell output for each displacement increase, along with user specified input. The program controlling fatigue testing has undergone numerous evolutions. Initially, the program was capable of accepting user input for frequency and displacement and was run in displacement control, in a similar fashion to the tensile test described above. The latest version of the software runs in force control, taking voltages from the force transducer to calculate appropriate motion of the displacement stage, and allows several user parameters to be entered, including force amplitude, mean force, frequency when cycling, frequency when recording, number of data points to be recorded and frequency of recording of data and images. Figure 1-13 is a simplified flowchart of program logic followed during a tensile or fatigue test.

Typically, as cracks grow during a fatigue test, samples become more compliant. This increase in compliance during a displacement controlled test is an effect known as load shedding. The resulting progressive decrease in force amplitude affect the driving force for crack progression and in turn can lead to a reduction in crack advance rate or crack arrest entirely. This effect is seen very prominently in samples which exhibit gross plastic deformation. Fortunately, neither gross plastic deformation nor load shedding was a problem in the fatigue testing of platinum; this was confirmed by recording maximum and minimum forces during fatigue tests, and is later explained in the compliance analysis section and the crack growth rate section. The first 3 tests were run using this program (Table 1-6), recording displacements, forces and images as specified. Later, the program was modified to be load controlled. The load control card (National Instruments NI PCI-7340) used the voltage signal of the load cell and several feedback parameters (Table 1-7) as input in order to calculate an appropriate output signal to the displacement stage conditioning box, all in real time. The latest version of this program was capable of accepting user input for frequency, mean load, load amplitude and imaging parameters and outputs entire waveforms for displacement and forces, as well as images, all at user specified intervals.
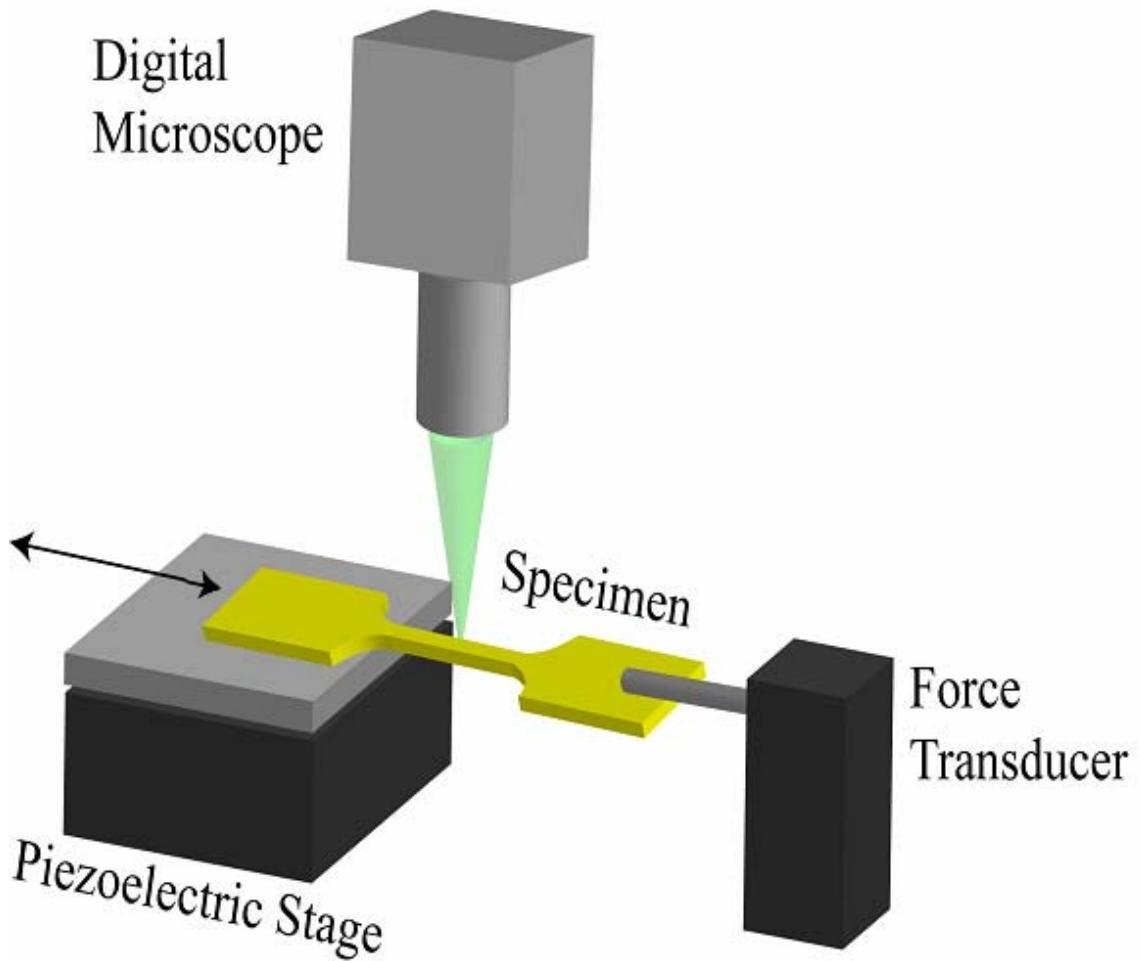
Figure 1-12: A basic schematic of the testing system showing the 3 major components of the system, a piezoelectric displacement stage to which the specimen die is affixed, a force transducer connected to the sample via an optical fiber or a needle, a digital microscope capable of imaging and recording the region of interest in real time.

Table 1-6: Test Specific Parameters

| Parameter	Tensile Test	Fatigue Test 1	Fatigue Test 2	Fatigue Test 3	Fatigue Test 4
Load Cell	GSO-10	GSO-10	GSO-10	GSO-10	Sensotec Model 31
Load Readout	SCXI	SCXI	SCXI	SCXI	Load control card
Lens	20×	20×	20×	100×	100×
Control Mode	Displacement	Displacement	Displacement	Displacement	Load
Grip	Optical Fiber	Optical Fiber	Optical Fiber	Needle	Needle
Incline	0°	0°	0°	-10°	-10°
Image Frequency	1 micron of displacement	30 seconds	Cycle	60 cycles	300 cycles
Rate	.1 µm/s	-	-	-	-
Loading Frequency	-	1 Hz	1 Hz	1 Hz	1 Hz
Load ratio	-	0.1	0.1	0.1	0.1
Loading wave	Linear ramp	Sine	Sine	Sine	Sine
Gage Width	150	200	150	100	100
Ambient Environment	Air	Air	Air	Air	Air
Temperature	22±2°C	22±2°C	22±2°C	22±2°C	22±2°C
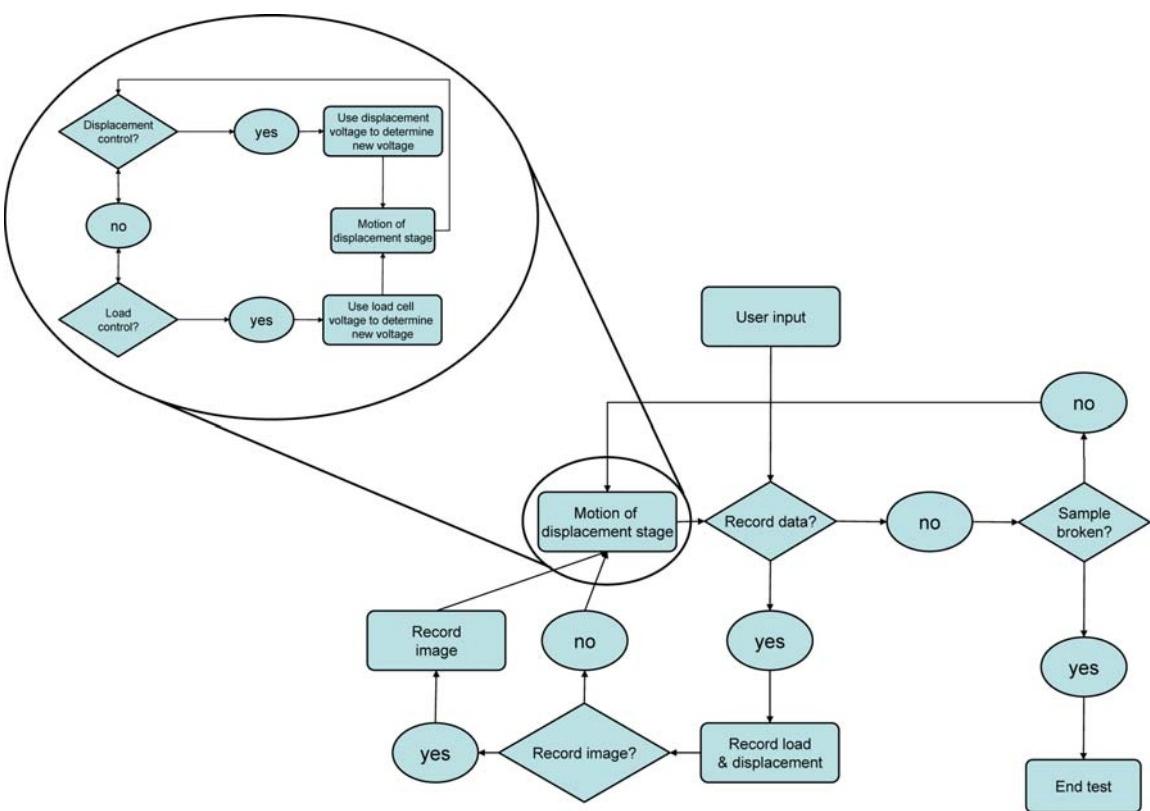
Figure 1-13: Basic flowchart of program logic followed during a tensile or fatigue test. Program begins with user input, records initial load, initial displacement, and initial image, then changes the motion of the displacement stage based on load or displacement control, either in a ramp or cyclic fashion, records data at regular intervals until the sample breaks.

Table 1-7: Feedback Parameters

Proportional Gain, Kp	5
Integral Gain, Ki	20
Integration Limit, IL	1000
Derivative Gain, Kd	0
Derivative Sampling Period, Td	0
Velocity Feedback Gain, Kv	0
Velocity Feedforward, Vff	0
Acceleration Feedforward, Aff	0

1.5   Analysis Methods

The raw recorded data (i.e. displacements, forces, and images) produced during the tests allowed for the examination of some of the basic behaviors of the films. Several analysis tools and formulas were used to organize the raw data into constitutive relationships. Analysis of data was largely performed in Excel® 2002 a spreadsheet application from Microsoft. All final curves were graphed and fitted using Levenberg-Marquardt algorithm of version 3.52 of Kaleidagraph®, a data analysis and graphic presentation software tool from Synergy Software. The following sections detail how data were analyzed.

1.5.1   Tensile Testing

All platinum samples without notches failed outside of the gauge section, presumably due to stress concentrations resulting from too high a filet angle (Figure 1-14). It should be noted that this problem was addressed in subsequent fabrication by the staff at the ARL at Adelphi, MD by reducing the taper angle. In order to overcome the fact that the platinum samples would not fail at the gauge section, a notched platinum sample was tensile tested. The stress concentration provided by the notch overcame other flaws in the material and resulted in proper fracture in the gauge section. The test was run in displacement control, at a displacement rate of 0.1 μm per second, in lab air (22±2°C). Due to the uniaxial tension nature of the experiment, stress was calculated by simply dividing the applied force by the cross sectional area of the gauge and by multiplying the applied nominal stress by the stress concentration factor of the notch (~5) [5]. This value is valid for elastic strain only, and as such, represents an upper bound for the stress concentration of the notch.
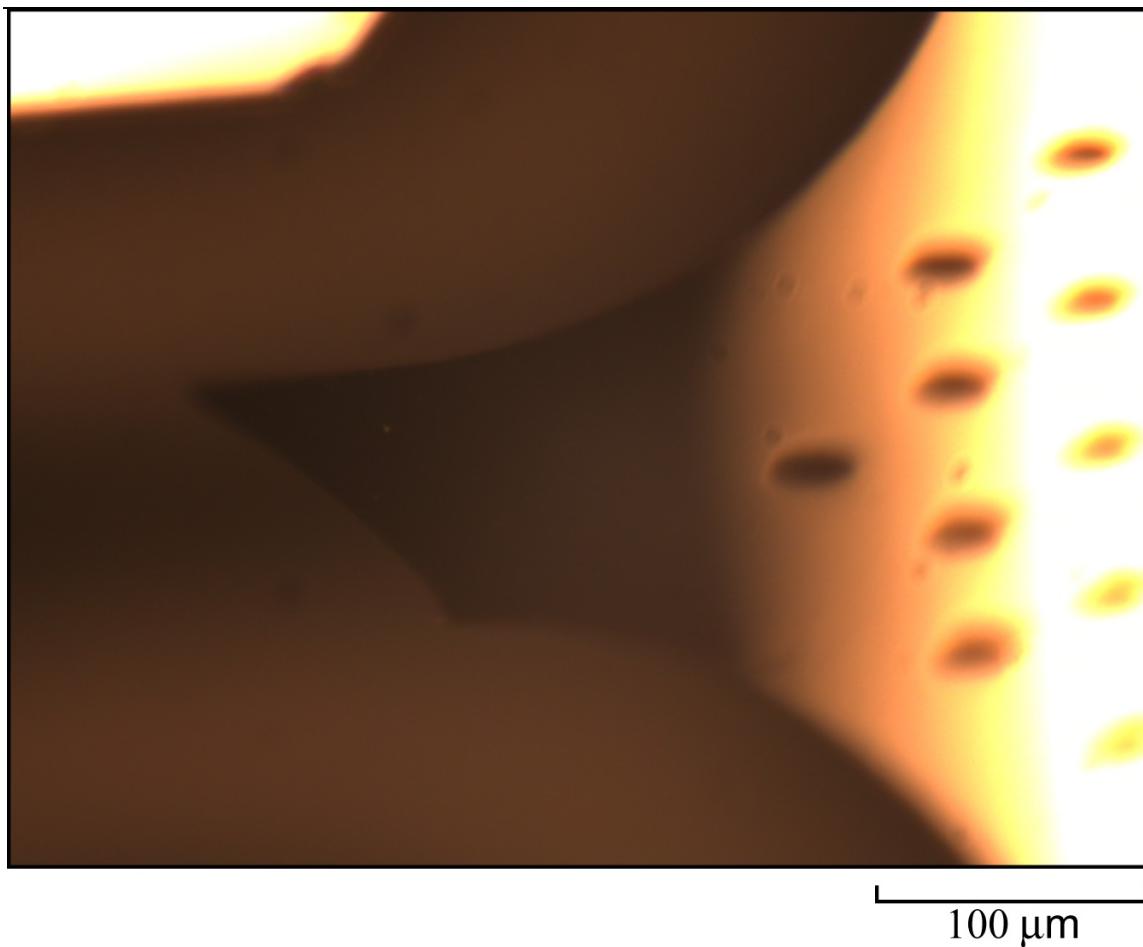
Figure 1-14: Failure outside of the gauge section, typical in platinum samples which were not notched. The distorted light reflections are strictly a result of the specimen not being parallel to the plane of the camera (i.e. it is out of focus).

1.5.2   Fatigue Testing

Four constant stress amplitude (load ratio $\sigma_{min}/\sigma_{max}$, $R = 0.1$, sinusoidal, 1 Hz) fatigue tests were conducted in laboratory air (22±2°C). In order to quantify the fatigue crack growth behavior of the samples, several components of the behavior were measured and/or calculated. The following section will detail how crack lengths were measured, and how stress intensities, crack growth rates, and crack closure were calculated.

1.5.2.1 Optical Measurements of Crack Length

Images captured for the duration of the test allowed for measurement of crack growth by optical analysis. This method is lens-specific and has a maximum resolution of 4 pixels (2 pixel from each measured end), which at the highest lens objective (100×) corresonds to 500 nanometers, close to the resolving power of the lens itself. Although this method has a very high theoretical resolution limit, it should be noted that long before this resolution limit is reached, the objectiveness of the user in determining the length to be measured comes in to play – the user must decide what he believes he should be measuring, which arguably, has a significantly higher error given picture quality, sub-surface cracking and human error.

By opening an image in Photoshop® CS2, a measurement can be taken of any line length. This measurement, in pixels, can be correlated using a known pixel-meter conversion which was found using a plate stage micrometer (VWR #82026-613) having a 0.05 micron resolution. This was performed on numerous images acquired during fatigue tests. In order to select a decent sample size from the many images acquired during each test, images were selected such that there was a measurable crack advance, i.e. at least one pixel of advance (equaling a 250 nanometer crack extension), between two consecutive analyzed images.

1.5.2.2 Compliance-Based Measurement of Crack Length

As cracks advance through a material, its compliance changed. By recording the compliance of the platinum samples as it varied through the test, it was possible to correlate the compliance value to a crack length. Compliances of the specimen and system were calculated by fitting a slope through a plot of force vs. displacement comprised of all (one hundred) recorded data points within the initial fatigue cycle. Raw measured values of compliance showed the compliance of both the system and the sample together.

Theoretical compliance of the specimen only was found using Equation **1**, a solution provided by Tada et al [6]:

$$C = \frac{1}{BE}\left[\frac{2a}{b} \times V_2\left(\frac{a}{b}\right) + \frac{h}{b}\right]$$

1

where a = crack length (initially ½ notch width), b = ½ gage width, h = ½ gage length and $V_2\left(\frac{a}{b}\right)$ was found using Equation **2**, another solution provided by Tada et al [6]:

$$V_2\left(\frac{a}{b}\right) = -1.071 + 0.250\left(\frac{a}{b}\right) - 0.357\left(\frac{a}{b}\right)^2 + 0.121\left(\frac{a}{b}\right)^3 - 0.047\left(\frac{a}{b}\right)^4 + 0.008\left(\frac{a}{b}\right)^5 - 1.071\frac{1}{\frac{a}{b}}\ln\left(1 - \frac{a}{b}\right)$$

2

By subtracting the theoretical value of specimen compliance from the measured compliance, system compliance was determined to be 5.42×10^{-5} m/N. By subtracting out the system compliance from the measured compliance, the initial value of measured compliance matches the theoretical value of specimen compliance. By multiplying the measured values of compliance by a constant, in our case, equivalent to multiplying the values of thickness and elastic modulus by 0.47, it was possible to match the theoretical compliance with the experimental compliance to a close degree. Using the measured compliance after correction, a value of crack length can be estimated from each value of compliance measured (Figure 1-15), however, the error for the estimate is dependant on the crack length, that is, error was initially large, and decreased as crack length increased. Values of compliance for the specimen showed that the initial platinum compliance was 1.33×10^{-4} m/N, and progressed throughout the test, ending at 1.40×10^{-4} m/N. This small change of compliance is the main reason why load shedding was not a significant problem in displacement controlled fatigue testing of the films.
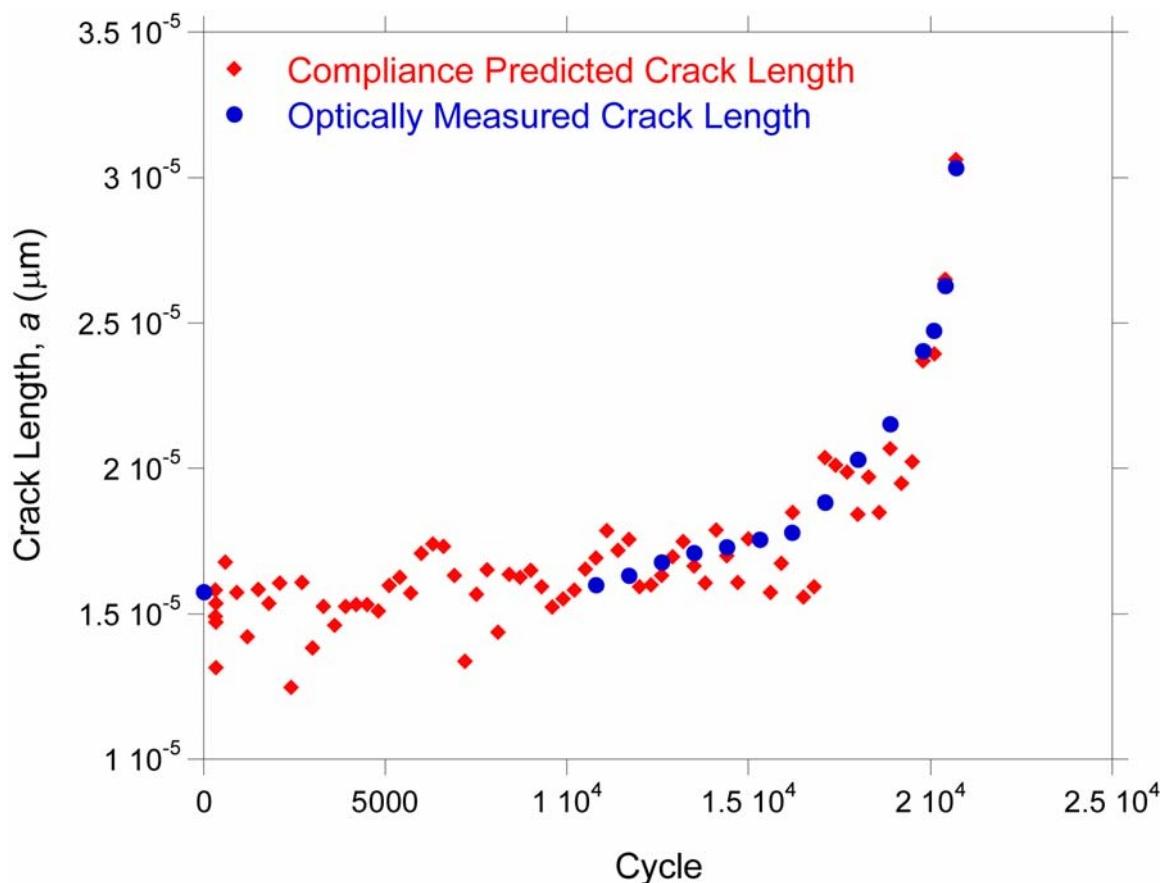
Figure 1-15: Plot of compliance-based predicted crack length (red) as a function of cycle, plotted along the optically measured crack length (blue) as a function of cycle. This plot shows that the compliance based predictions of crack length match well with the measured lengths, but show significant scatter.

1.5.2.3 Stress Intensity Factor Calculation

Stress intensity factor, a measure of the driving force of crack advance was found using Equation 1-1:

$$\Delta K = \Delta \sigma \cdot \sqrt{\pi \cdot a} \cdot f\left(\frac{a}{b}\right)$$ 1-1

where a = crack length (initially ½ notch width), b = ½ gage width, $\Delta \sigma = \sigma_{max} - \sigma_{min}$ as determined from load cell forces and $f\left(\frac{a}{b}\right)$ was found using Equation 1-2, a solution provided by Tada et al [6].

$$f\left(\frac{a}{b}\right) = \left\{1 - 0.025\left(\frac{a}{b}\right)^2 + 0.06\left(\frac{a}{b}\right)^4\right\}\sqrt{\sec\left(\frac{\pi \cdot a}{2 \cdot b}\right)}$$ 1-2

Due to the symmetric crack growth from both ends of the notch (as will be reported in a future section), the stress intensity factors from the two ends of the notch were combined to form an average stress intensity factor.

1.5.2.4 Crack Growth Rate Measurement

Crack growth rates were calculated by dividing the change in the optically measured crack length by the change in cycle (secant method, 3 point, 50% overlap [4]). Due to the noisy and scattered nature of the compliance measurement, compliance based crack lengths predictions exhibited an equally scattered nature. Although these predictions have excellent correlation to the optically measured crack lengths, the scatter hinders the secant method from being used, as negative crack growth rates ('crack healing') would be falsely computed.

1.5.2.5 Closure Analysis

It has been shown that mechanisms occurring in the crack wake can influence the driving force for crack propagation and in turn, the rate of crack advance [7, 8]. These closure mechanisms are more dominant at lower ΔK and low load ratios due to the smaller crack opening displacements. Significant crack closure would result in higher stresses generated at the initial crack opening in a cycle – a deviation from linearity having higher slopes at the lowest displacements. Closure analysis was performed for the fourth fatigue test. This analysis was performed by measuring the linearity of the full force vs. displacement curves throughout the test. This linearity measure was

taken by plotting force vs. displacement for full cycles throughout the test and fitting the resulting plot with a linear fit (Figure 1-16). The R value, a good measure of the correlation of the linear fit was recorded for cycles throughout the test.
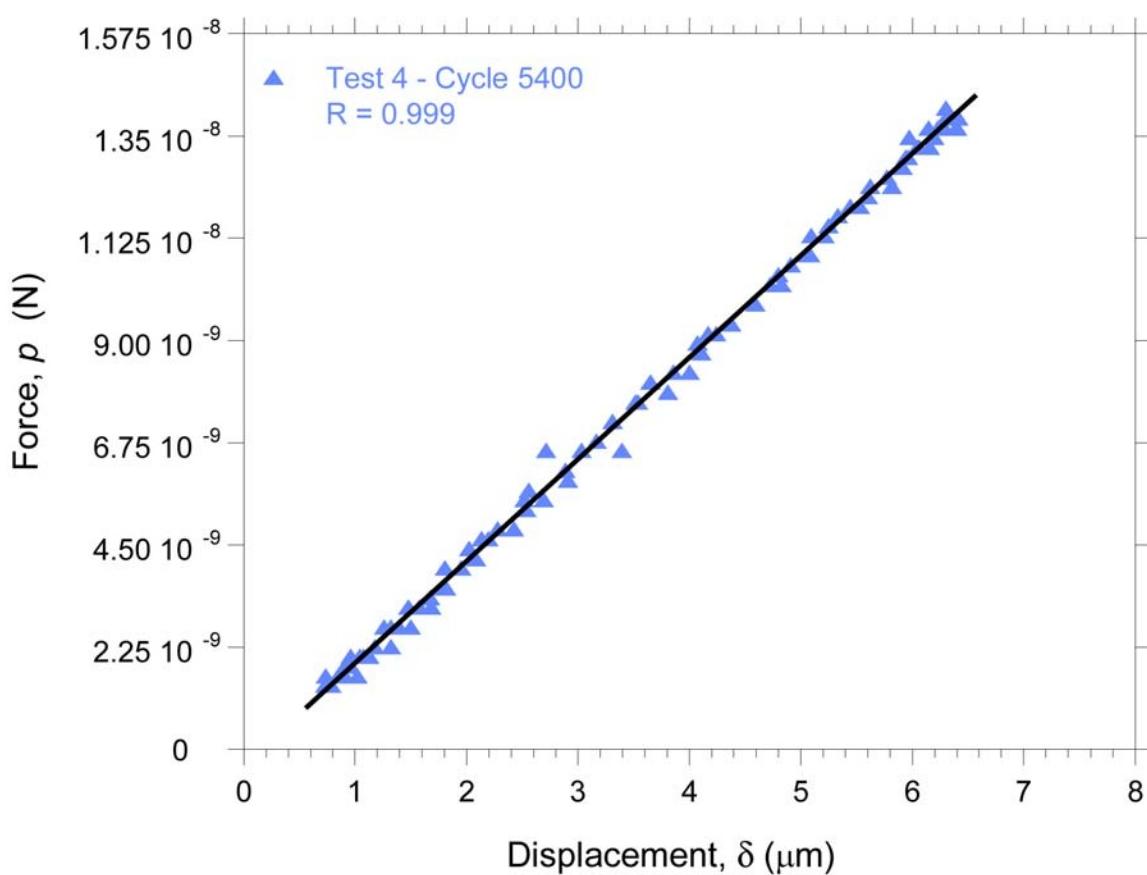

Figure 1-16: Typical force-displacement curve from fatigue test 4. Slopes and correlation values (R) were recorded for several cycles throughout the test.

1.5.3   Field Emission Scanning Electron Microscopy

After fatigue failure, resulting fracture surfaces were imaged in a field emission scanning electron microscope (FE-SEM). Two versions of the stub holding the fracture surfaces were used; neither mounting technique required alteration of the sample or fracture surfaces for image clarity. Fractography of failed specimens was performed using a JEOL JSM-6700F FE-SEM operating at a range kV (from 5 to 15, depending on best results). The following section will detail the mounting technique used to mount the fatigue fracture samples.

After several unsuccessful mounts of samples, including a fatigue sample from test 1, a sample from test 2 was successfully mounted on a 45 degree inclined aluminum stub and adhered to it with carbon glue. Viewing of the sample was difficult but was achieved via inclining the stub up to 20 degrees further within the instrument (Figure 1-17). A modified stub was created specifically for the mounting of thin film fracture surfaces on tungsten needles. Holes matching the diameter the needle were drilled into aluminum stubs which were hollowed midway through the stub, allowing needles to be placed vertically into the stub and exposing the fracture surface directly. The underside of the needle protrudes from the hollowed out end, and is further fixed in place by the application of silver paint on the underside, thus keeping the fracture surface far from any glue (Figure 1-18).
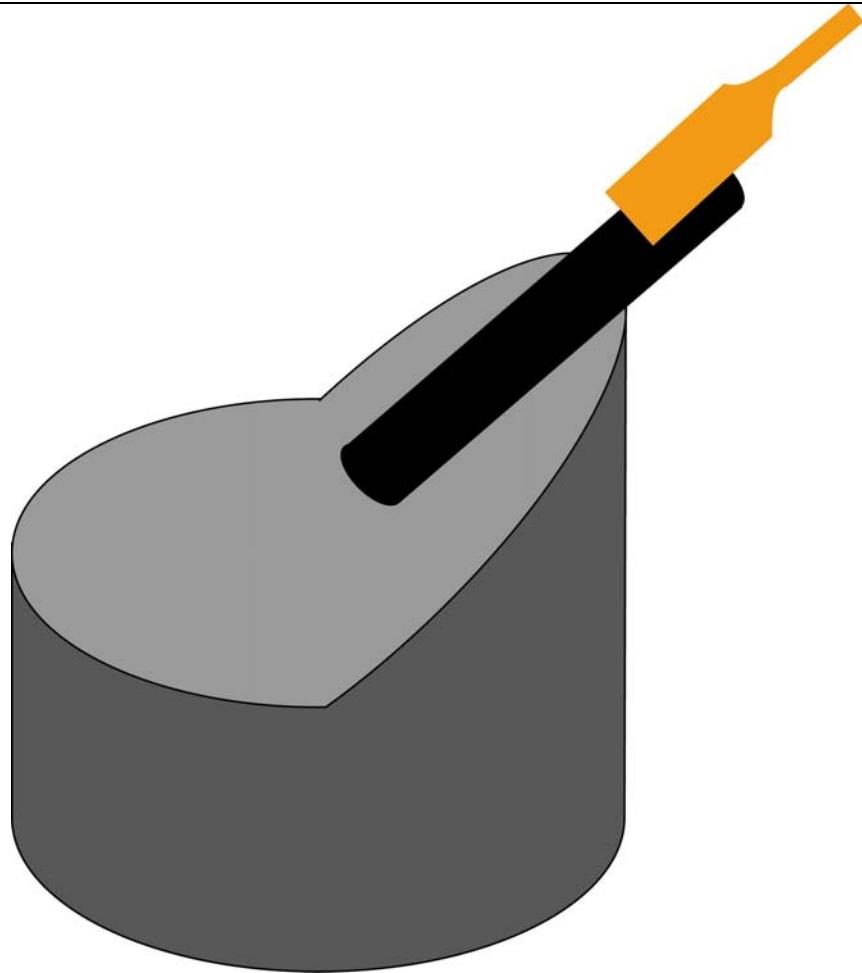
Figure 1-17: Schematic of the 45 degree inclined stub used to hold a fatigue fracture surface from test 2. Carbon glue was used in the region where the needle (shown in black) met the stub (shown in the light gray).
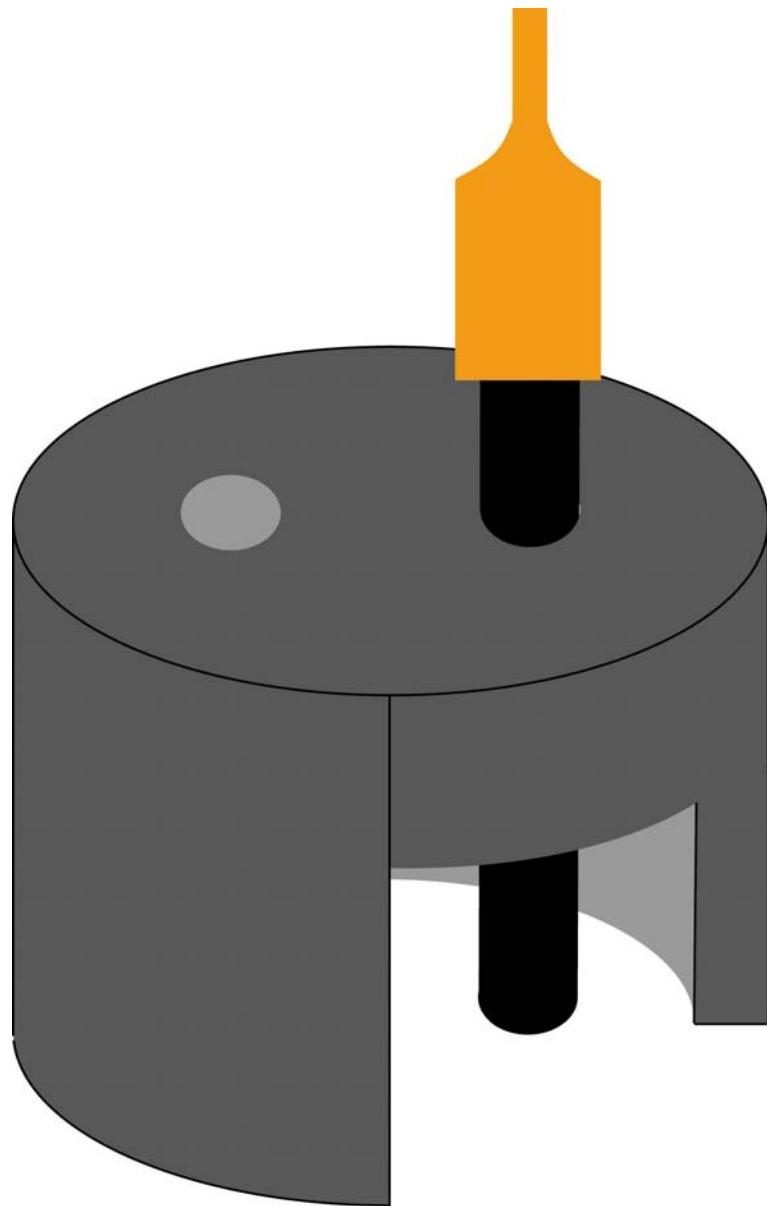
Figure 1-18: Schematic of the vertical specimen stub specifically designed to hold fatigue fracture surfaces such as those from tests 3 and 4. Silver paint was used where the needle (shown in black) protruded from the underside of the stub (not visible).

## 2	Results and Discussion

This section will open with a detailing of results from the tensile test performed on the platinum sample. Results will show the thin film nanocrystalline platinum has a higher ultimate tensile strength than microcrystalline platinum. The section will transition to reporting about the four fatigue tests performed on the platinum samples. Crack lengths tracked throughout the tests will be reported and discussed. A discussion of crack growth rates will follow. These crack growth rate curves will show that platinum behaves in an unexpected manner, unique from other FCC metals. Mechanical testing results will conclude with a discussion of crack closure for the fatigue tests. At the conclusion of results stemming directly from testing, there will be an analysis of fracture surfaces examined by FE-SEM. Results from this analysis will show that the mechanism which is driving crack growth in the nanocrystalline platinum has led to intergranular failure at low crack velocities, and transitions to transgranular fracture at higher velocities. In order to attempt to explain the results observed in this study, mechanisms will be proposed and discussed. The section will also feature an in-depth discussion of mechanisms for intergranular failure observed and predicted in metals. In addition to the literature findings, a review of the crystallography of slip relating to a (111) oriented FCC metal will follow, noting the likelihood of an alternate hypothesis which explains the apparent intergranular failure.

2.1   Tensile Behavior

This section will discuss the results of the tension test performed on a centrally notched platinum sample. By using the far field stress and the stress concentration factor of the notch, it was possible to calculate the effective stress at the tip of the notch. The general yielding of the specimen has been suppressed by concentrating the deformation at the notch roots as indicated by the linearity of the force-displacement response (Figure 2-1). Some film buckling is apparent during the test, introducing a slight, but unavoidable error into the test; buckled regions during the test appear flat after fracture, suggesting that this buckling is purely elastic. After some ductile tearing at the notch, fracture occurred via a shear mechanism that proceeded on surfaces inclined to the loading direction at an angle of about 45° (Figure 2-2).

By using the largest force recorded during the tensile test, and dividing it by the cross-sectional area, the nominal stress was found to be 681.6 MPa. By calculating the stress concentration provided by the notch [5], the maximum stress at the tip of notch was calculated. This value of ultimate tensile strength (UTS) was found to be 3.4 GPa. Because it is likely that some plastic deformation occurred at the crack tip prior to failure, this value represents an upper bound estimate on the UTS. In comparison, nanoindentation of these thin films while still attached to the substrate have found a yield strength of 1.97 GPa [9], and unpublished results of tensile testing of these free standing thin films have found a yield strength of 1.47 GPa [10], although the latter finding is based on the reported thickness of the films (500 nm) whereas our studies have measured this value directly to be (450 nm). In either way, both the experimental yield strengths, and the upper bound value of UTS is significantly larger (more than an order of magnitude) than that of microcrystalline platinum which has a yield strength of 185 MPa and a UTS of 240 MPa [11], confirming trends relating to the Hall-Petch relationship.
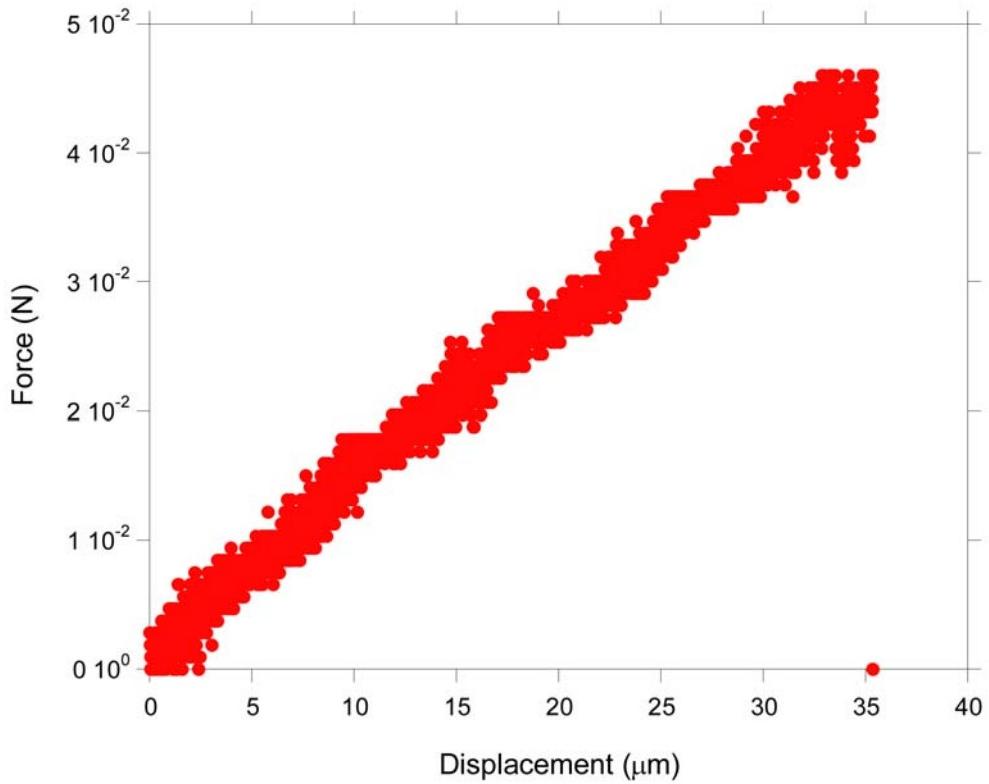
Figure 2-1: Force-crosshead displacement curve for a uniaxial tensile test conducted on a 150 μm wide, center-notched micromachined platinum specimen (the last point marks specimen failure). The upper bound for the ultimate tensile force of this specimen was calculated to be 3.4 GPa once the stress concentration factor of the notch was taken into account.
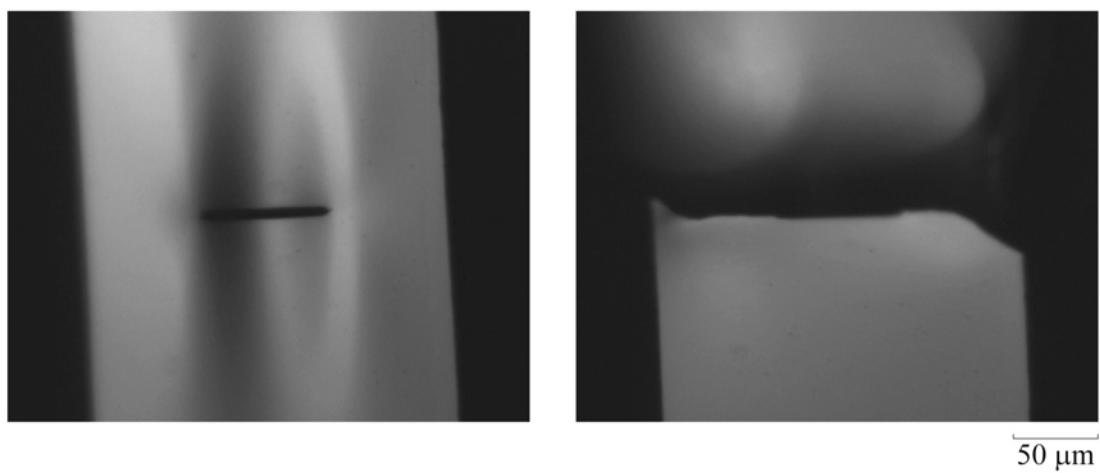
Figure 2-2: Optical micrographs of a notched tensile specimen of Pt during testing (left) and immediately after failure (right). After some ductile tearing at the notch (flat portions on either side of the notch), fracture occurred via a shear mechanism that proceeded on surfaces inclined to the loading direction (45° slanted portions on either end of the flat portions).

2.2   Fatigue Crack Length as a Function of Fatigue Cycle

This section will discuss crack extension during fatigue cycling of the platinum films. Cracks extended symmetrically from the central notch and propagated at similar growth rates. Due to the crack symmetry, average crack length, averaging crack length from both ends of the notch, is reported for two tests in which the initial notch spanned the same percent of the sample width but where stress amplitude was measurably different.

During the fatigue crack growth tests, cracks grew symmetrically from the notches and exhibited straight (i.e., nominally mode I) crack paths, and surface distortions associated with the development of the plastic zone were not observed. Final rupture of the specimens occurred on paths that were inclined 45° from the tensile loading axis after an unknown amount of stable, ductile tearing. (Figure 2-3). The symmetry of the crack extension from both ends allows for reasonable averaging of the two crack lengths. (Figure 2-4) This symmetric growth is also a testament to the uniaxial conditions of the testing setup, as well as the overall uniform material properties of the nanocrystalline platinum.

Stress amplitude, initial average crack length, final average crack length, and sample lifetime results are summarized in Table 2-1. Stress amplitude varied between 300 MPa and 332 MPa, all above the ultimate tensile strength of microcrystalline platinum, but ranging roughly between 9 and 10% of the ultimate tensile strength of nanocrystalline platinum (3.4 GPa) as was found in the previously described tensile test. Average initial crack sizes were all 33% of the gauge width, and ranged 51% to 63% of the gauge width just prior to failure. Final recorded lifetimes of samples ranged between 700 and 9900 cycles, although there may have been some final crack growth between the final recorded cycle and the actual cycle associated with failure (as not every cycle was recorded). It is apparent that an increase in initial stress intensity produces a decrease in overall lifetime as would be expected, and indicates that the testing methodology is consistent and repeatable. Figure 2-5 shows the average crack length to specimen width ratio as a function of cycle of all four platinum fatigue tests.
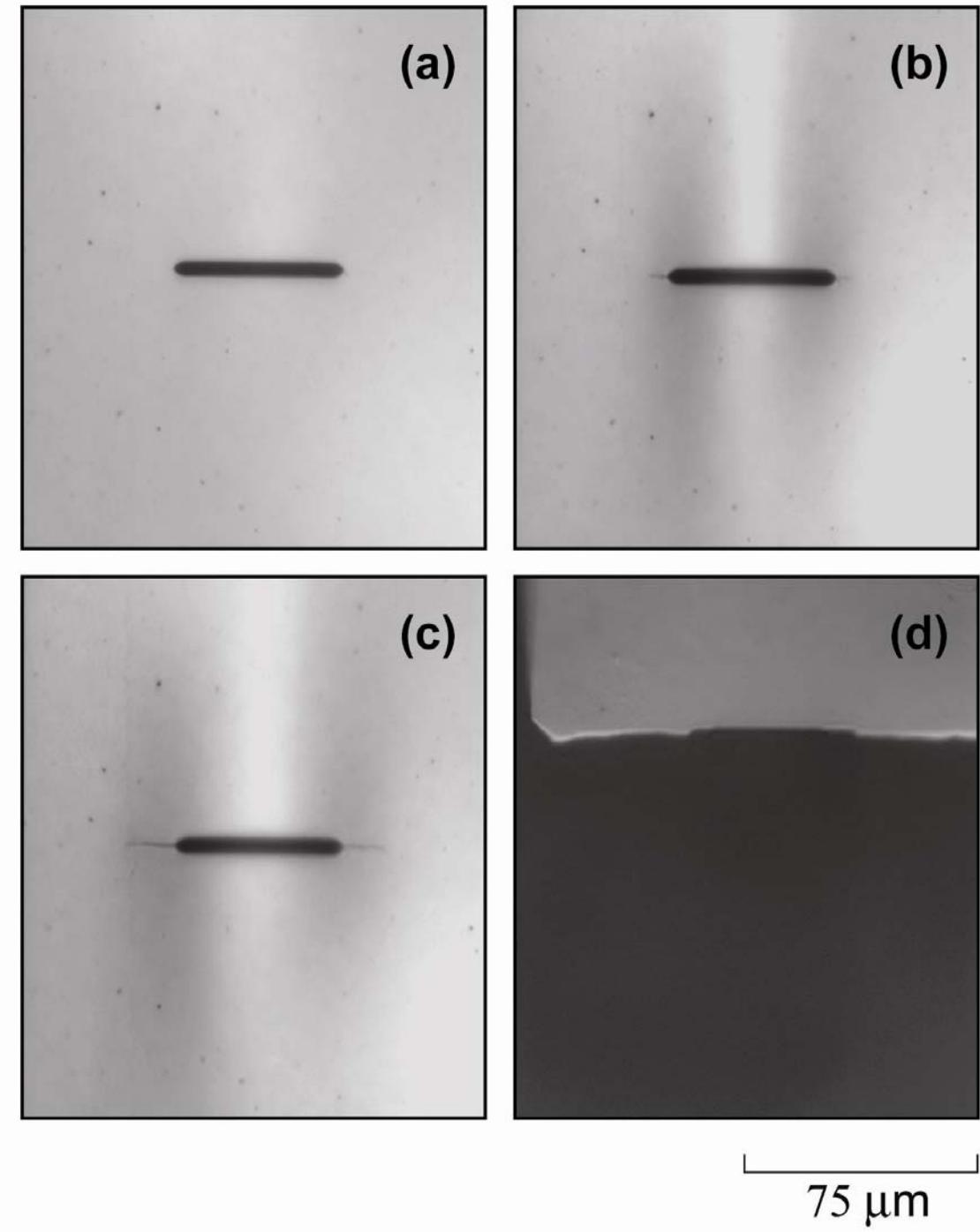
Figure 2-3: Optical images acquired during fatigue testing of a nanocrystalline Pt film (test 3) showing (a) the initial slot, (b) a crack at 50% of the critical crack size, (c) a crack at 75% of the critical crack size, (d) the sample after fracture.
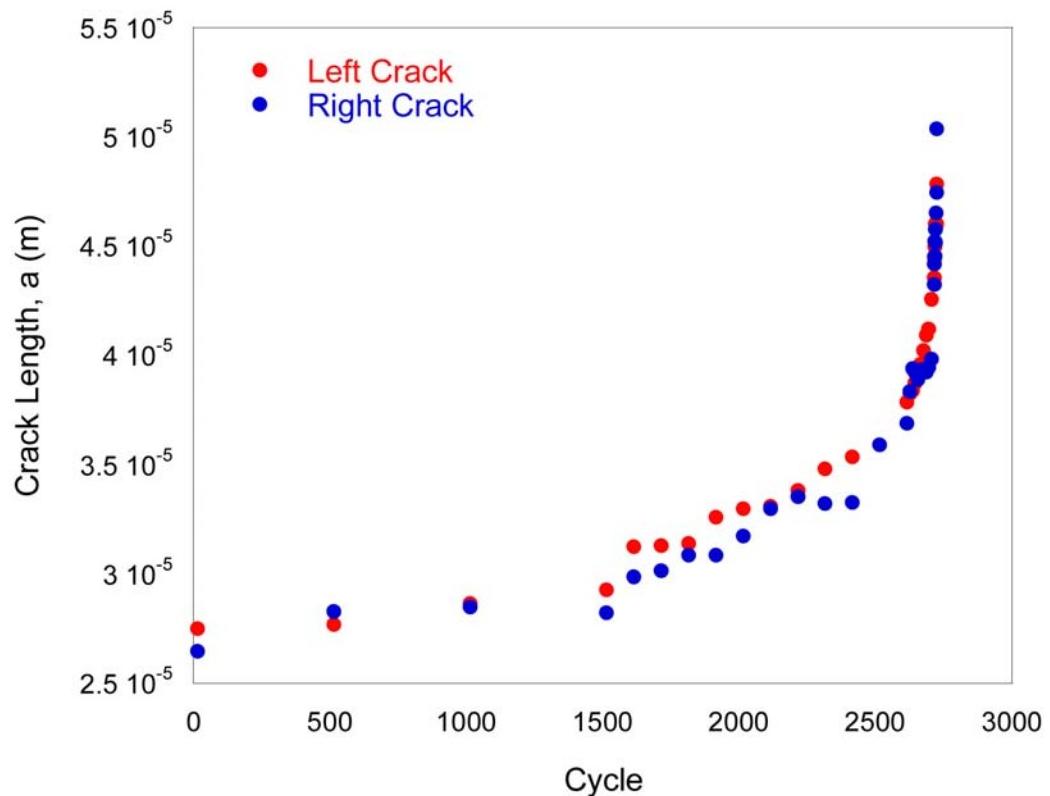
Figure 2-4: Crack Length (as measured optically) as a function of cycle in fatigue test 2 showing that cracks from both ends of the notch grew at similar rates.

Table 2-1: Summary of crack growth results of the 4 platinum fatigue tests

	Stress Amplitude, $\Delta\sigma$ (MPa)	Initial Average Crack Length, a (μm)	Final Average Crack Length, a (μm)	Final Crack Length to Gauge Width Ratio	Sample Lifetime (cycles)
Test 1	330	33.6	50.9	0.51:1	700
Test 2	300	27.0	49.1	0.61:1	2723
Test 3	332	26.2	47.6	0.61:1	790
Test 4	311	16.0	30.3	0.63:1	9900
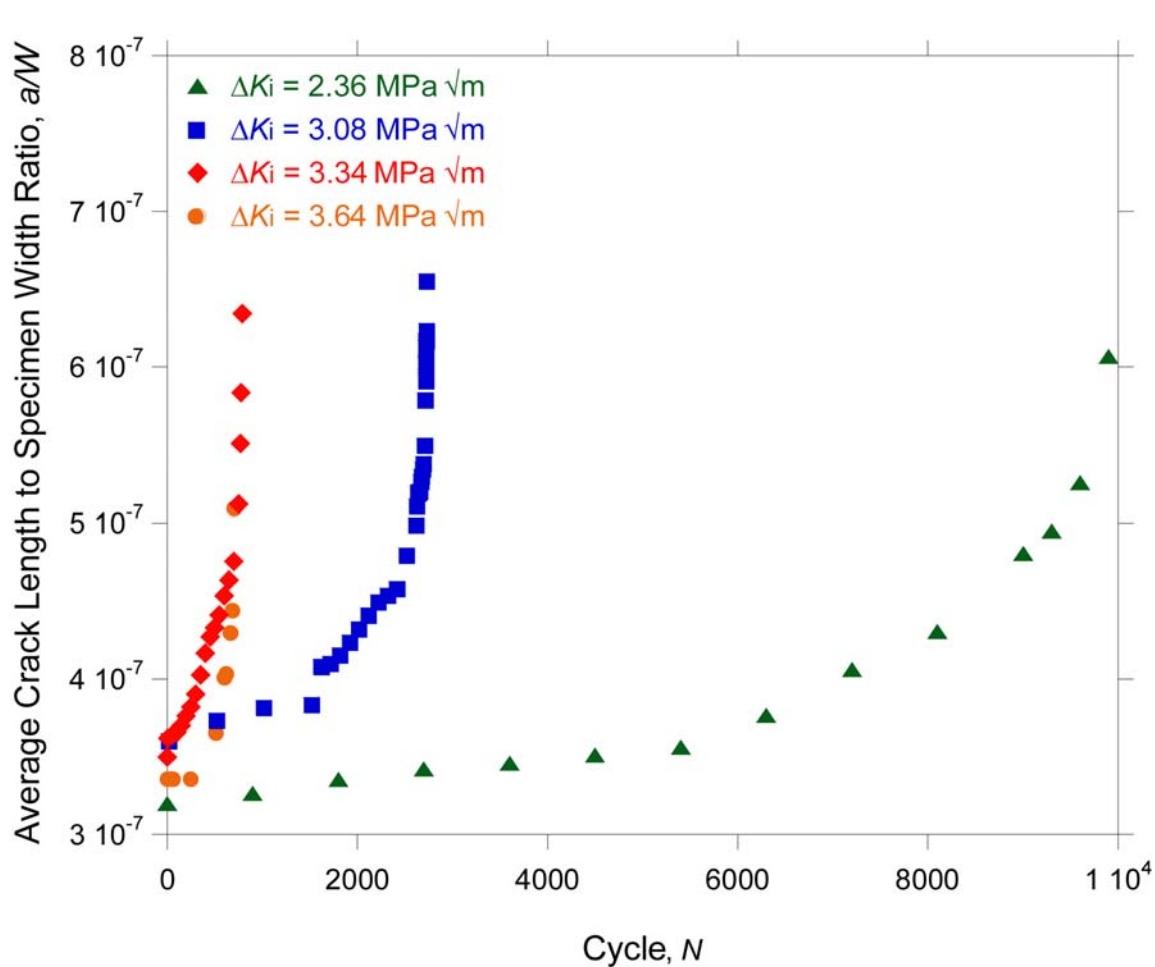
Figure 2-5: Average crack length to specimen width ratio as a function of cycle in all four platinum fatigue tests. Note the correlation between a lower initial stress intensity (ΔKi) and longer fatigue lifetime.

2.3   Average Crack Growth Rate as a Function of Average Stress Intensity Factor Range

This section will discuss the crack growth rates of the platinum films resulting from cyclic fatigue. The crack growth rate curve plotted against the stress intensity factor will be shown for each individual test. Their close agreement to each other allows the data from all 4 tests to be plotted at once; all 4 tests will be shown together and plotted beside the data for microcrystalline platinum tested in air [1]. The results will show the significant difference between the nanocrystalline and the microcrystalline platinum.

The measured fatigue crack growth rates as a function of the applied stress intensity factor ranges are shown in Figure 2-6. An extremely limited range of stable fatigue crack growth was observed (~2.5 MPa √m), and a least squares curve fit of the data to a power law relationship between the fatigue crack growth rate da/dN and the applied stress intensity factor range, ΔK, (i.e., $da/dN = C(\Delta K)^m$) provided a large power law exponent, m, with values ranging between 7.9 and 15.3. The fracture toughness, K_q, estimated from K_{max} just prior to fracture ranged from 4.45 MPa √m to 4.88 MPa √m for the first 3 tested samples, and was 3.45 MPa √m on the fourth test. It is likely that there was a significant amount of additional stable crack growth after the last recorded data point and prior to failure in the fourth fatigue test; this growth was not captured due to the fact that data as recorded less often to minimize data volume during longer fatigue tests. Stress amplitude, scaling constants, power law exponents and fracture toughness are summarized in Table 2-2.

In contrast to microcrystalline metals, the nanograined Pt films in this investigation exhibited fatigue crack growth rate trends that were reminiscent of extrinsically toughened structural ceramics and ordered intermetallics (i.e., $m > 10$). Consistent with this observation, the fracture toughness of the nanograined Pt film was exceptionally low – ~10 times less than the micrograined form of the material, (Figure 2-7).
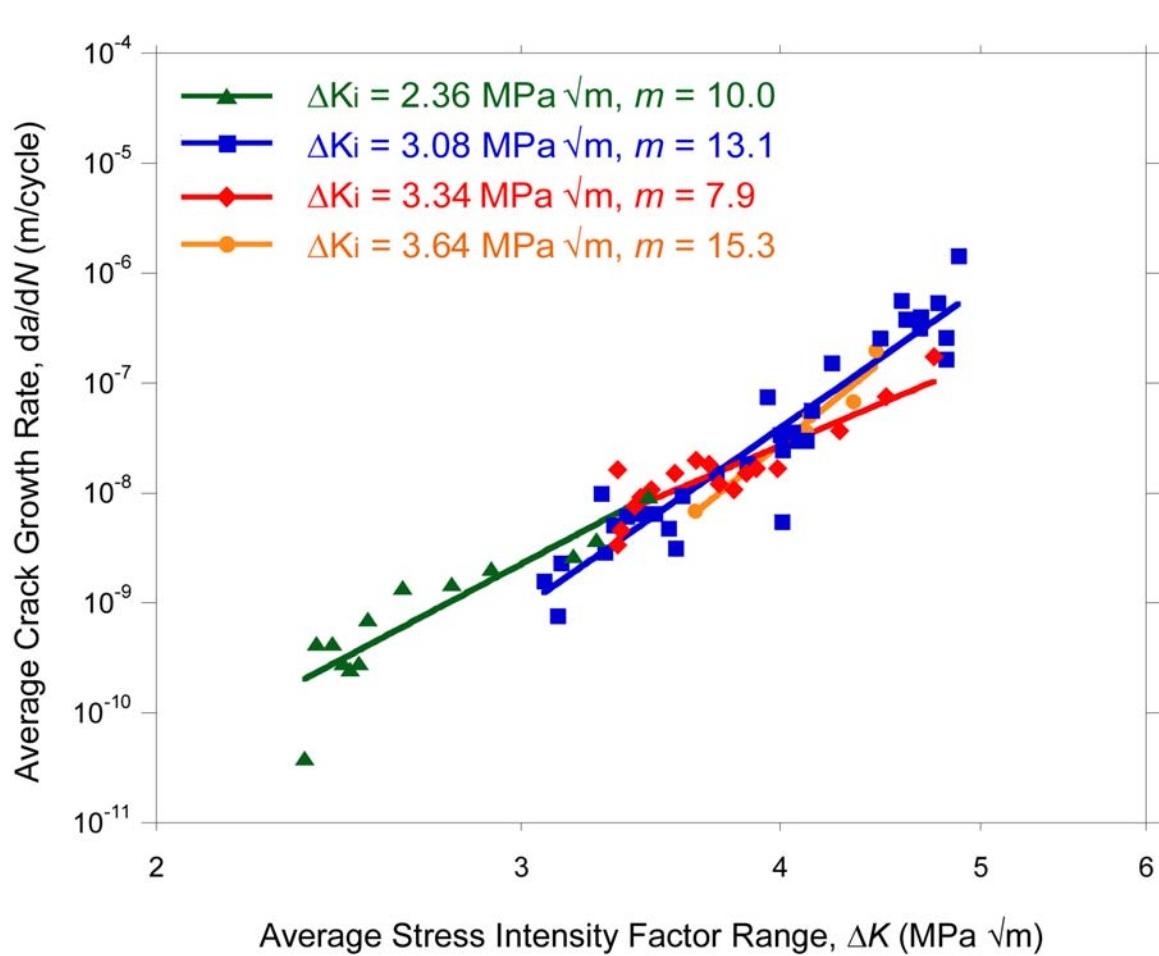
Figure 2-6: Empirically measured fatigue crack growth behavior of nanograined platinum films. Four tests are plotted individually and noted by their initial stress intensities (ΔKi). The power law fit of the nanograined Pt indicates a high power law exponent (m ranging from ~8 to ~15).

Table 2-2: Summary of crack growth rate results of the 4 platinum fatigue tests

	Stress Amplitude, $\Delta\sigma$ (MPa)	Scaling Constant, C	Power Law Exponent, m	Fracture Toughness, K_q, (MPa $\sqrt{m}$)
Test 1	330	1.80×10^{-17}	15.3	4.45
Test 2	300	4.77×10^{-16}	13.1	4.88
Test 3	332	4.59×10^{-13}	7.9	4.75
Test 4	311	3.83×10^{-14}	10.0	3.45
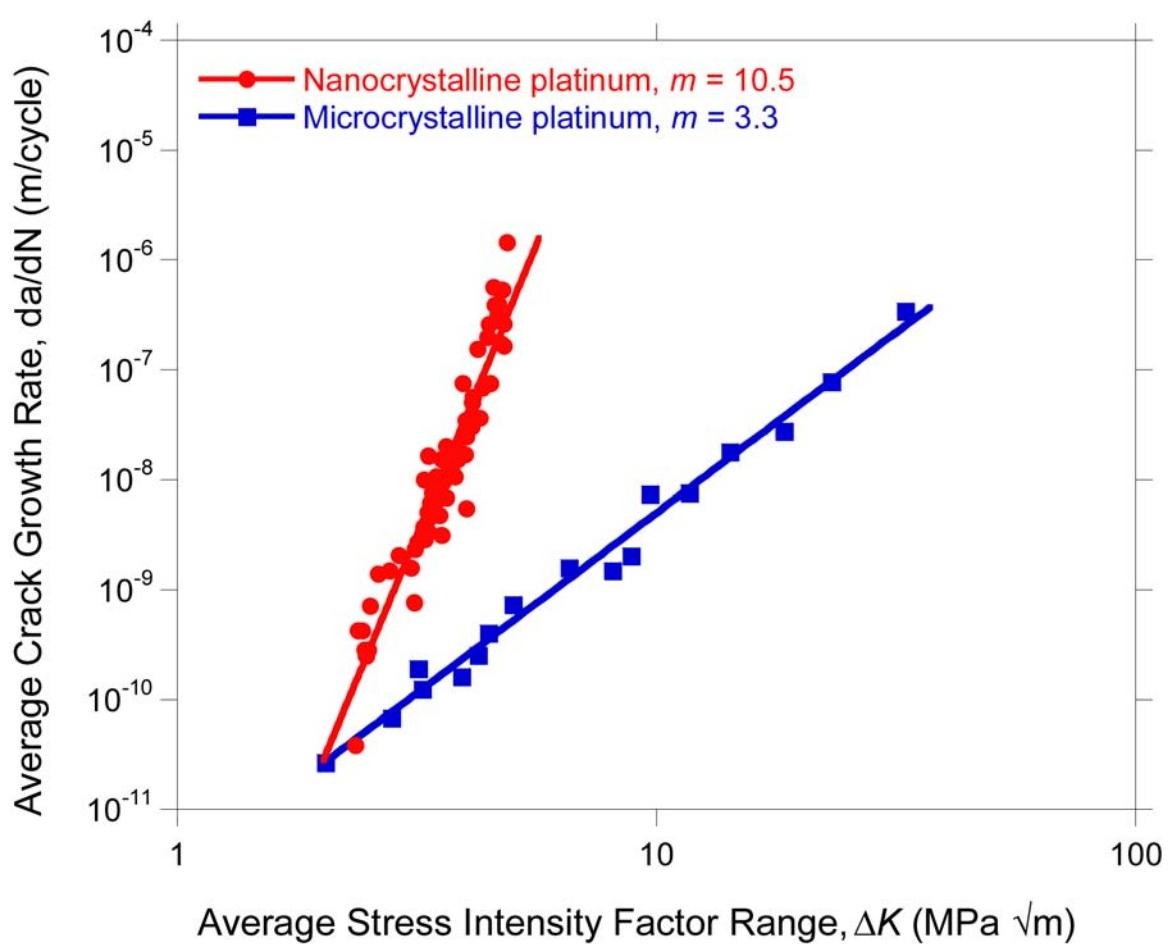
Figure 2-7: Empirically measured fatigue crack growth behavior of nanograined Pt films (red circles) compared to a power law fit of previously published data for micrograined Pt by Speidel (blue circles) [1]. The power law fit of the nanograined Pt (solid line) indicates a high power law exponent ($m = 10.5$) when compared to the microcrystalline Pt behavior ($m = 3.3$). The absence of a conventional, sigmoidally-shaped fatigue crack growth curve is readily apparent in the nanograined Pt data.

2.4   Crack Closure Analysis

Materials such as ceramics or ordered intermetallics having high crack growth exponents typically show some degree of extrinsically induced crack closure. Crack closure is a toughening mechanism which acts in the wake of the growing cracks and acts to shield the crack tip from the far-field driving forces [8]. There are several mechanisms which contribute to crack closure, such as (but not limited to) 'wedging' (debris or surface roughness induced closure) and 'bridging' (ligament or fiber induced closure). As crack closure serves to shield the crack tip at the lowest displacements, a non linearity is typically noticeable at those displacements (Figure 2-8). This closure is typically more dominant at low ΔK and lower load ratios due to the smaller crack opening displacements (and thus increased interaction of the two crack wake fronts). The overlap of the closure process zone and the crack wake grows larger as the crack grows (until stable state is reached when 100% of the process zone overlaps the crack wake) and so closure effects typically become more noticeable as the fatigue crack length increases. These effects can be observed by plotting and comparing the force-displacement curves throughout a fatigue test. The effects of crack closure on the fatigue crack growth rates are notoriously difficult to quantify due to the small fluctuations in microstructure along the path of the crack, and the dependence of crack closure on testing conditions (load ratio, environment etc.) [8]. The descriptions of the fatigue crack growth behavior in the previous sections relate the fatigue behavior of nanocrystalline platinum to the behavior of brittle ceramics which typically exhibit some crack closure effects. In order to examine this behavior further, the extent of crack closure in the nanocrystalline platinum thin films was quantified.

Data from the last fatigue test in which full force-displacement curves were available were analyzed for crack closure effects. Force-displacement data for cycles at various stages of the fatigue test were plotted. There was no apparent change in linearity in the compliance curves during a single cycle, and this linearity did not vary as the cracks extended throughout the course of the test (Figure 2-9). The linear compliance curve, measured for a relatively low load ratio of 0.1 would be indicative of a lack of crack closure effects in nanocrystalline platinum.
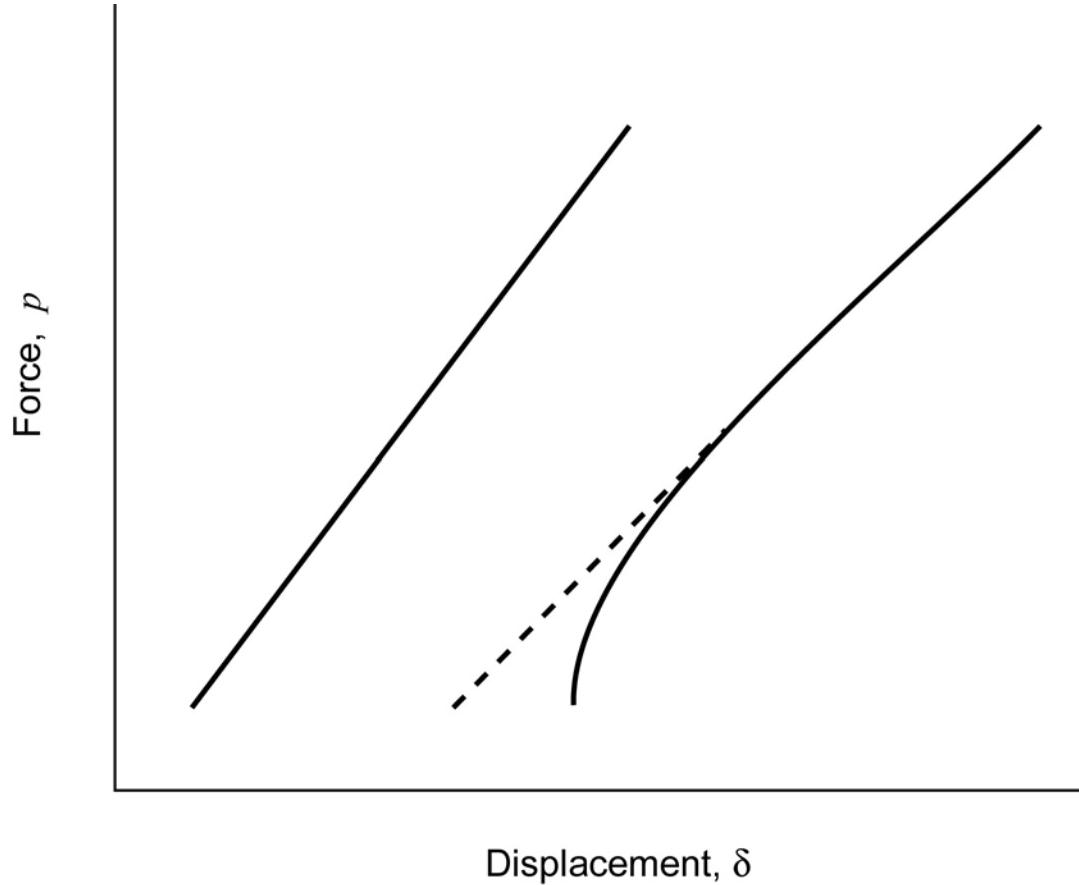
Figure 2-8: A schematic of typical crack closure effects on force as a function of displacement plot. The relationship shown at the left is of an early cycle in a fatigue test where there has not been significant crack growth; the linearity is indicative of no significant amount of crack closure effects. A later cycle within the same fatigue test is shown at the right; notice the shift in data and a reduction in slope as a result of the increasing compliance of the specimen as the cracks advance, but also note the non linearity at the low crack opening displacement, indicative of crack closure effects.
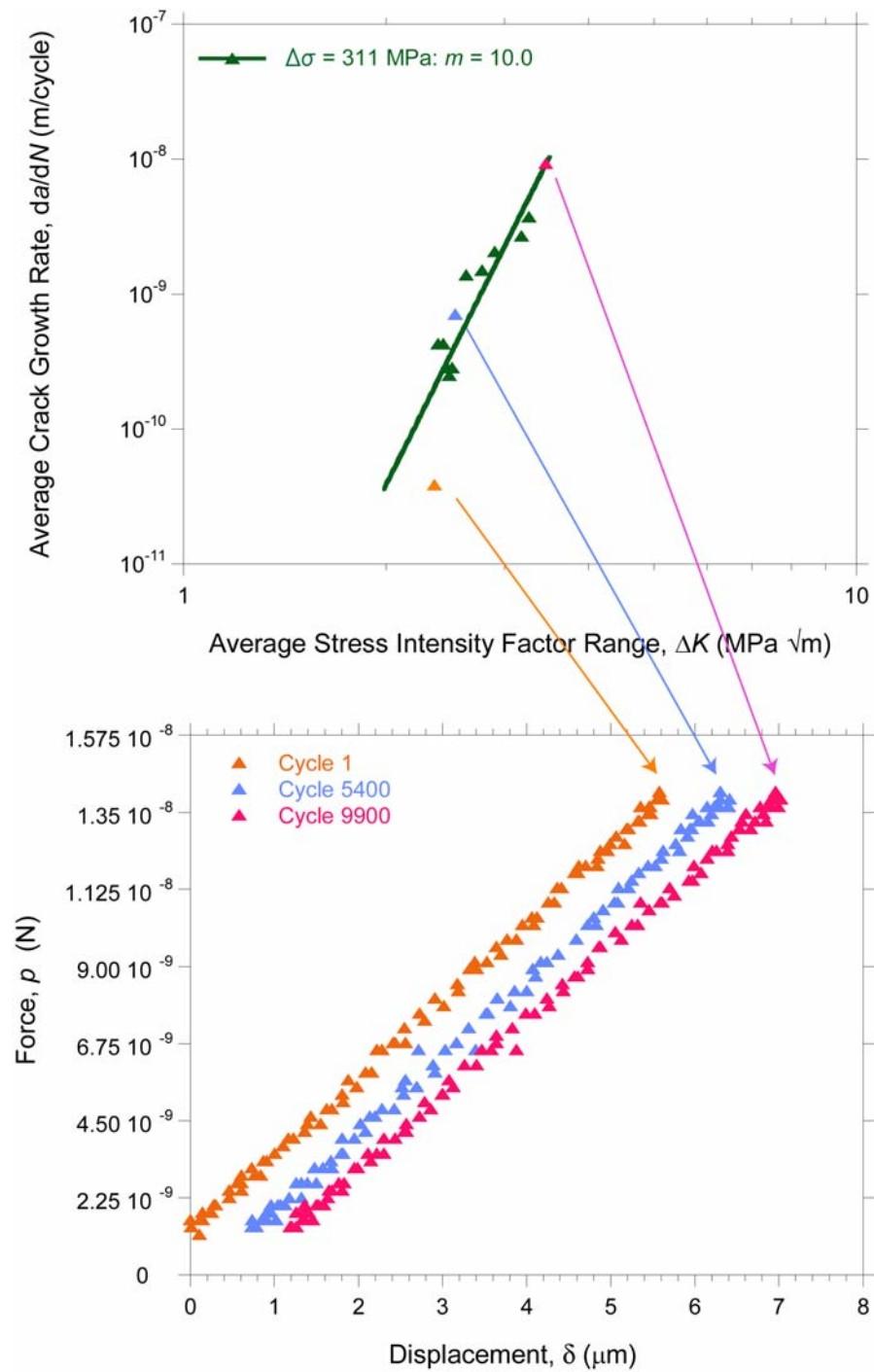
Figure 2-9: Crack closure analysis comparing early, mid, and late cycles in fatigue test 4. No significant change in linearity can be seen. The shift in the data is due to a change in compliance as a result of crack growth.

2.5   Field Emission Scanning Electron Microscopy Analysis

Fatigue fracture surfaces of the nanocrystalline platinum samples were mounted on a custom modified stub and were examined using a field emission scanning electron microscope (FE-SEM). Microscopy of the failure surfaces of the revealed that the cracks in the nanograined platinum initially followed an intergranular path and transitioned to a transgranular path at higher crack growth rates.

The fatigue crack path occurring in areas nearest the notch and analogous to the near-threshold regime (i.e., growth rates below 10^{-9} m/cycle) and up to $\sim2\times10^{-7}$ m/cycle was intergranular (Figure 2-10). Images from this region reveal visible grains and secondary cracking. As the cracks grew in length and accelerated to $\sim3\times10^{-7}$ m/cycle, they gradually transitioned to a transgranular path. During this transition, a fine ridge associated with localized transverse necking of the material developed in the center of the failure surfaces, parallel to the crack propagation direction. This relatively short section (Figure 2-11) exhibited both visible grains associated with an intergranular crack path, as well the plastic sheer lip associated with a transgranular crack path. The transgranular mode dominated the crack path at growth rates larger than 4×10^{-7} m/cycle (Figure 2-12). This crack path, most visibly designated by a central ridge associated with plastic deformation, persisted until final fracture occurred at K_{max} ~5 MPa $\sqrt{m}$. The fatigue crack growth rates of all 4 tests are correlated to the fracture surface in Figure 2-13, and the three portions of the fracture surface are shown collectively in Figure 2-14; the color scheme is consistent between the two aforementioned figures.
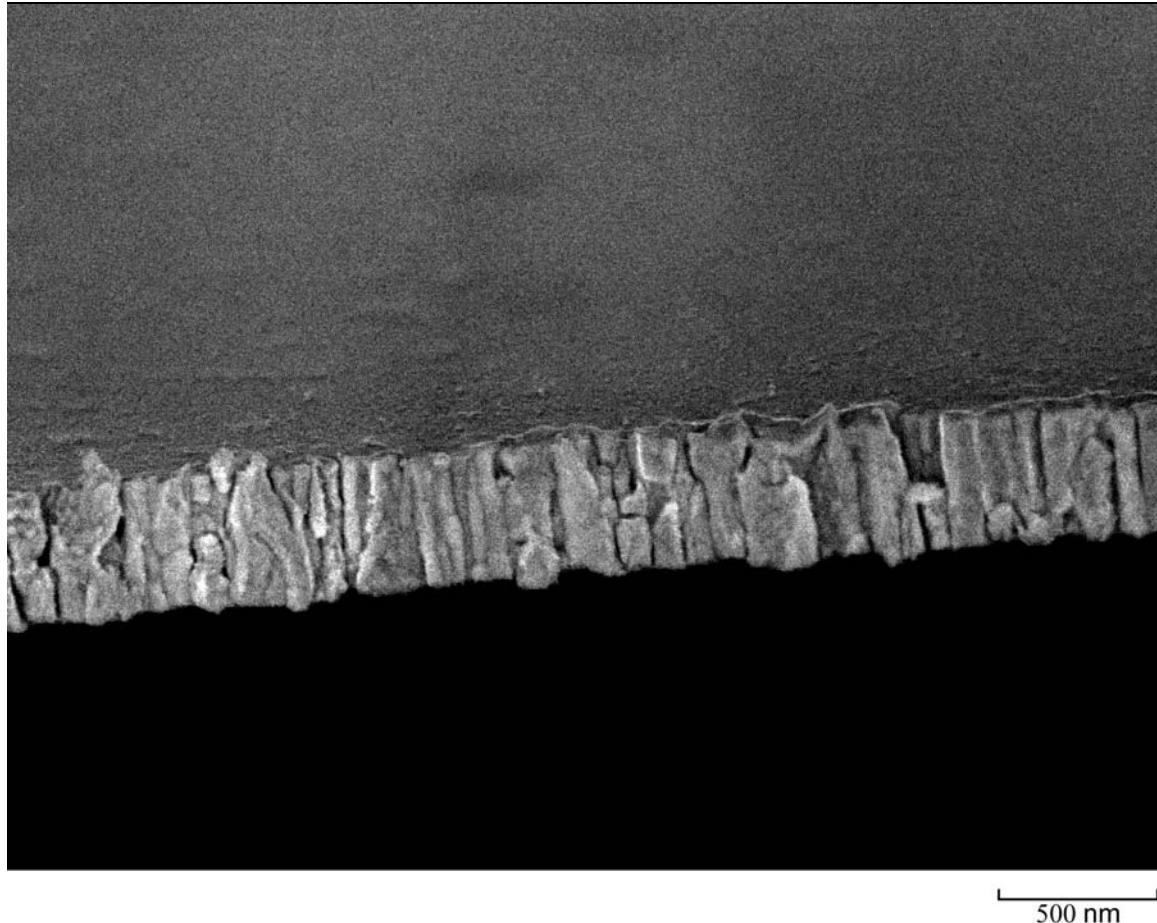
Figure 2-10: Intergranular failure in an area roughly 3 μm from the notch. This crack path is characterized by visible columnar grains and microcracking. This image is representative of the early portions of crack growth. Taken from Test 3 (ΔK = 3.02 MPa $\sqrt{\text{m}}$, da/dN = 7.62×10^{-9})

500 nm
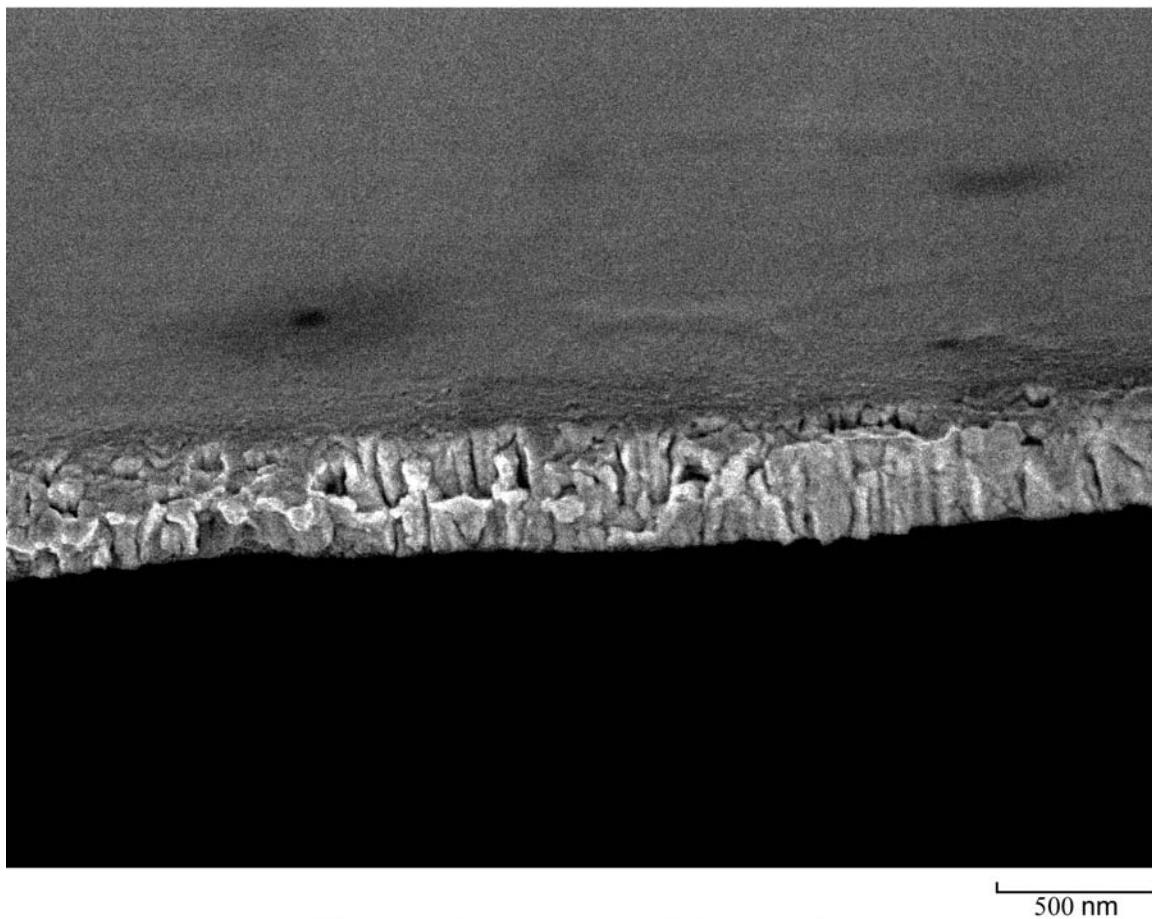
Figure 2-11: Transitional cracking behavior in an area roughly 17 μm from the notch. This crack path is characterized by a gradual transition from an intergranular crack path to a transgranular one. Taken from Test 3 (ΔK = 4.05 MPa $\sqrt{}$m, da/dN = 1.78×10^{-7})
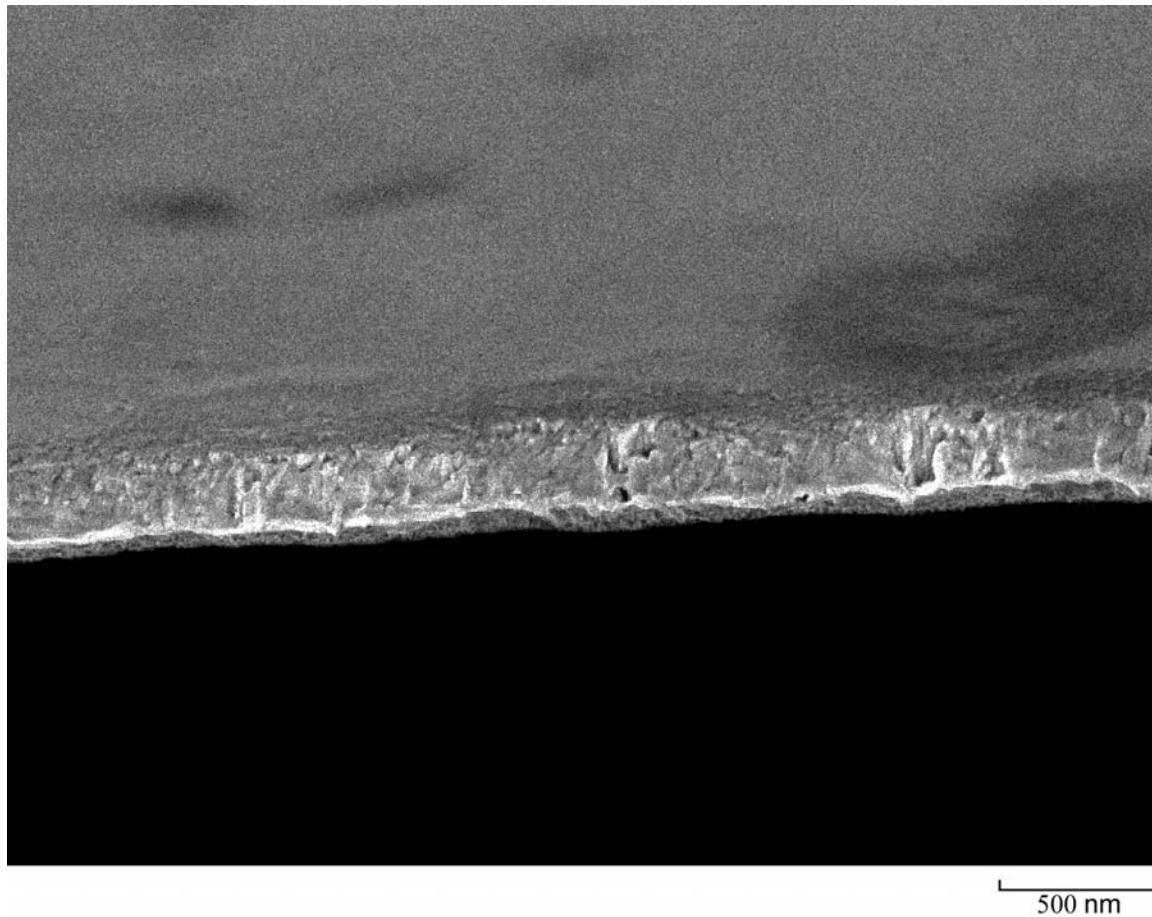
Figure 2-12: Transgranular failure in an area roughly 21 μm from the notch. This crack path is characterized by a lack of apparent grain structure and a plastic sheer lip running across the center of the fracture path. This image is representative of the later portions of crack growth. Taken from Test 3 (ΔK = 4.27 MPa $\sqrt{m}$, da/dN = 3.13×10^{-7})
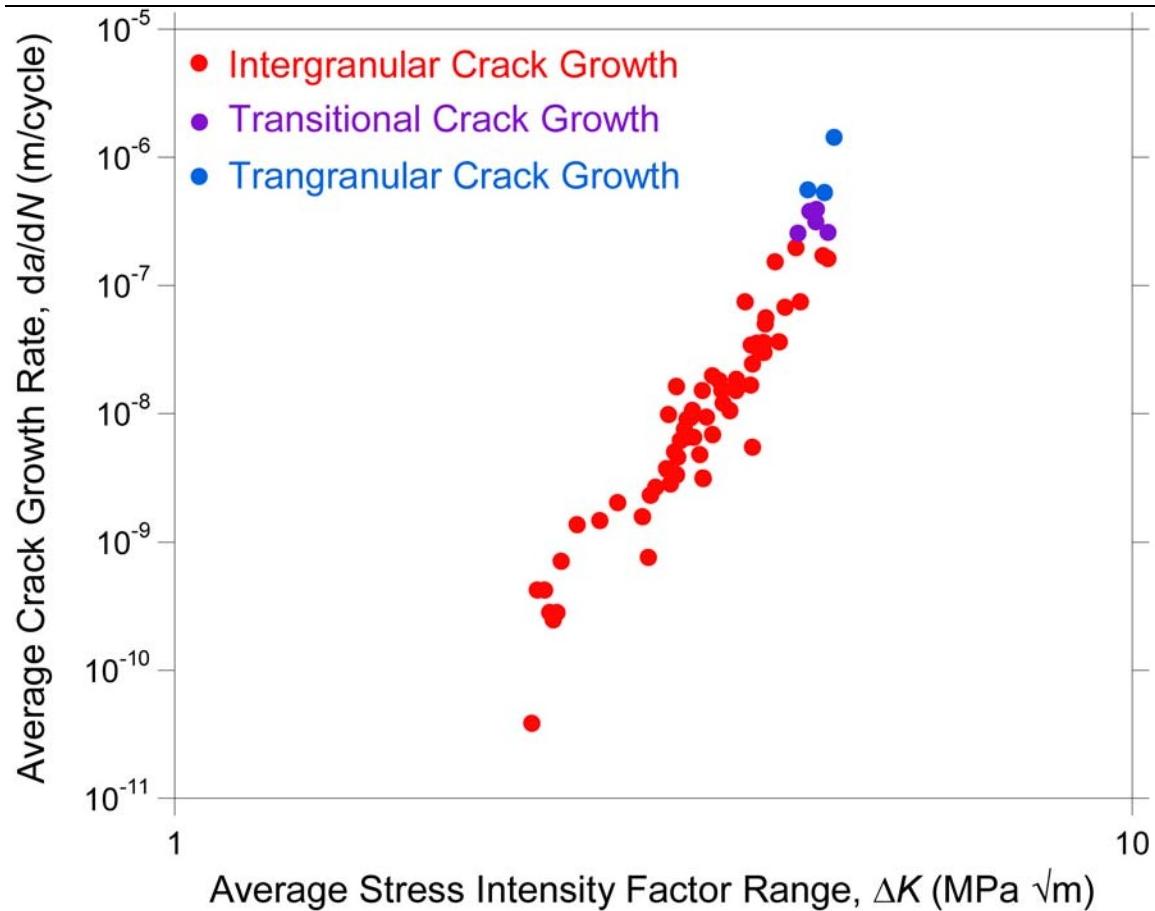
Figure 2-13: Crack growth rate curves highlighting crack advance mechanisms: intergranular advance (red), transitional advance (purple), and transgranular advance (blue).
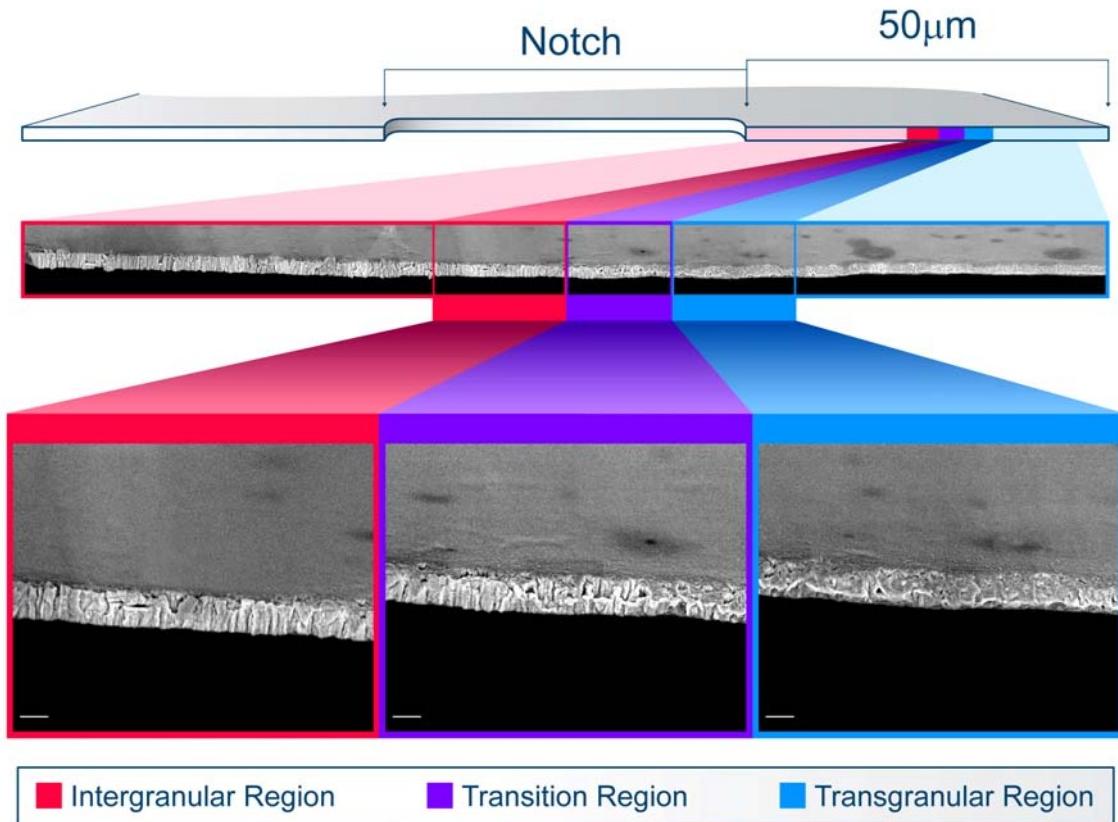
Figure 2-14: Scanning electron micrographs of a typical Pt film fatigue failure surface in relation to the original sample. As the crack advanced from left to right, the crack propagated via an intergranular path (red). As the fatigue crack growth rate reached $\sim 2 \times 10^{-7}$ m/cycle, the growth mode transitioned to a mixed inter- and transgranular morphology (purple). Above $\sim 3 \times 10^{-7}$ m/cycle, the crack path was transgranular (blue) with a central ridge that was associated with localized necking. The scale bar in the images corresponds to 300 nm.

3   Proposed Fatigue Mechanisms

Intergranular failure modes in face-centered cubic (FCC) metals are usually associated with boundaries that have been weakened by the presence of a secondary phase or atomic species [12], "active" (i.e., corrosive) service environments [13], or gross structural defects such as cracks and voids [14]. Extensive analysis by EDS, EELS and SIMS has revealed secondary phases at or below detection limits of the instruments, which means they are an unlikely cause of the unusual crack mechanism. No gross quantity of cracks or voids was detected by TEM. The high tensile strength confirms the film is strong. The transition from an intergranular crack path to a transgranular one indicated that the mechanism may be velocity dependant and not resulting of an impure or defective film.

3.1   Intergranular Failure in Literature

In order to better understand the mechanisms giving rise to intergranular cracking, an overview of reports of intergranular failure in metals, across all length scales, is presented in this section. The proposition that face centered cubic metals may fracture intergranularly is not foreign to the literature, but experimental accounts are few, and mechanistic explanations conflict with each other and with modeling work. Several investigations found evidence of intergranular cracking resulting from cyclic fatigue of polycrystalline copper [15-18]. These investigations cited the source of this intergranular cracking was a result of void coalescence at grain boundary and persistent slip band (PSB) junctions, citing that the theoretical shear stresses necessary to create voids at grain boundary and PSB junctions in polycrystalline copper are less than the real sheer stresses operating within a PSB. However, these studies also found that a reduction of grain size functioned to stifle this intergranular cracking. An additional investigation of the mechanism operating at the interaction of PSB with a grain boundary complemented their fatigue testing polycrystalline copper with a numerical model after closely studying the cracking under a scanning electron microscope [19]. By calculating the degree of misorientation of grain boundaries, Liu et al showed that grain boundaries having the highest misorientations were the most susceptible to intergranular cracking due to the impingement of PSBs against the grain boundaries. Their model estimated that the minimum theoretical shear stress which is required to act in the PSBs for causing intergranular cracks were always smaller than the real shear stresses operating within a PSB. Like other models, this model failed to explain why not all PSB-grain boundary regions formed intergranular cracks. A later investigation on the same material system concluded that the intergranular cracking was a result of environmental reasons, citing no such cracking when this oxidation was limited by cathodic polarization [20]. These reports of intergranular failure in a microcrystalline metal are confined to copper, and have been shown to be a cause of environmental reasons. These findings are unlikely to relate to the mechanisms operating in nanocrystalline platinum due to the significant difference in grain size, and platinum's natural resistance to oxidation.

The experimental reports of intergranular cracks are limited to grain sizes in the micrometer range. Several experimental investigations on nanocrystalline and ultra-fine grain metallic system which did not directly report intergranular cracking have cited the possibility of grain boundary dominated plastic deformation for their unexpected results. Deviations from expected behavior in nickel [21], in gold [22], in aluminum and palladium [23], and copper and nickel [24] have all been attributed to a change in plastic deformation mechanism due to an increase in grain boundary dominated mechanisms such as grain boundary reorientation, sliding and creep. The investigation

reported on this thesis would go to suggest that these models may be partially correct. In testing free standing nanocrystalline platinum samples, a plastic deformation mechanism which appears to be grain boundary dominated spans a large portion of the stable fatigue crack growth. However, in our study, this mechanism changes as the crack growth rate increases to become a grain interior dominated deformation mechanism, a transition which no experimental work has shown and no modeling work has predicted.

3.2   Crystallography of Slip

An alternate hypothesis that the fracture surfaces produced are in fact not intergranular, and rather faceted surfaces produced by typical crystallographic slip will be explored in this section. The most common mode of plastic deformation in metals is by the process of dislocation slip. Dislocation slip is the process whereby a dislocation will move through the material as a result of the gliding of close packed planes over one another. In face centered cubic (FCC) metals such as platinum, the close packed plane is the (111) plane; it has the greatest quantity of atoms per unit area. Slip generally proceeds along the close packed direction within a close packed plane, in the case of the (111) plane, the 110 direction is the close packed direction [25]. Dislocations may slip from one close packed direction to another within the same plane; the 110 direction within a (111) plane are 60° rotated from one another, suggesting that within a plane, facets of up to ±60° (exactly) can be created as dislocations pass across the grain. The slip deformation process is hindered by obstacles in the lattice such as grain boundaries, necessitating a change in the direction of crack growth to an alternate close packed plane or close packed direction. The close packed planes in a textured film such as the platinum films used in this study suggests that (111) planes in different grains are parallel, however, the close packed directions within them are not necessarily parallel, and due to the three-fold rotational symmetry of the plane, may be as much as 30° off from one another (Figure 2-15). This crack advance method suggests that the crack path will be serrated, having teeth-like features across the fracture surface.

This explanation for crack advance is consistent with the fracture portions tied to low crack growth rates. This mechanism assumes that the slip direction will change across grain boundaries in order to maintain the direction requiring the least amount of energy for slip, however, nearer the end of the test, more energy is available per area (as a result of a reduced area ahead of the crack tip), and maintaining this mode of cracking may not be necessary; dislocations may have enough energy to slip in multiple directions, eliminating the faceted features of the crack path. This explanation is also consistent with the lack of facets towards the end of the testing, when crack growth rates are highest. Although this theory explains the features seen when viewing the

fracture path with no tilt angle, additional information becomes available when viewing a fracture surface with tilt. Viewing the sample at angle allows for easier interpretation of the angles associated with the fracture as this viewing mode allows the three-dimensional nature of the fracture surface to be seen (Figure 2-16).

Figure 2-17 shows the fracture path of a fatigued platinum sample (test 2). Using this angled view, it is apparent that some features cannot be explained strictly using the crystallographic slip explanation. Some facets are angled, almost circular, and other are much sharper than the predicted maximum of 15°, suggesting that the fracture path is more likely to be intergranular.
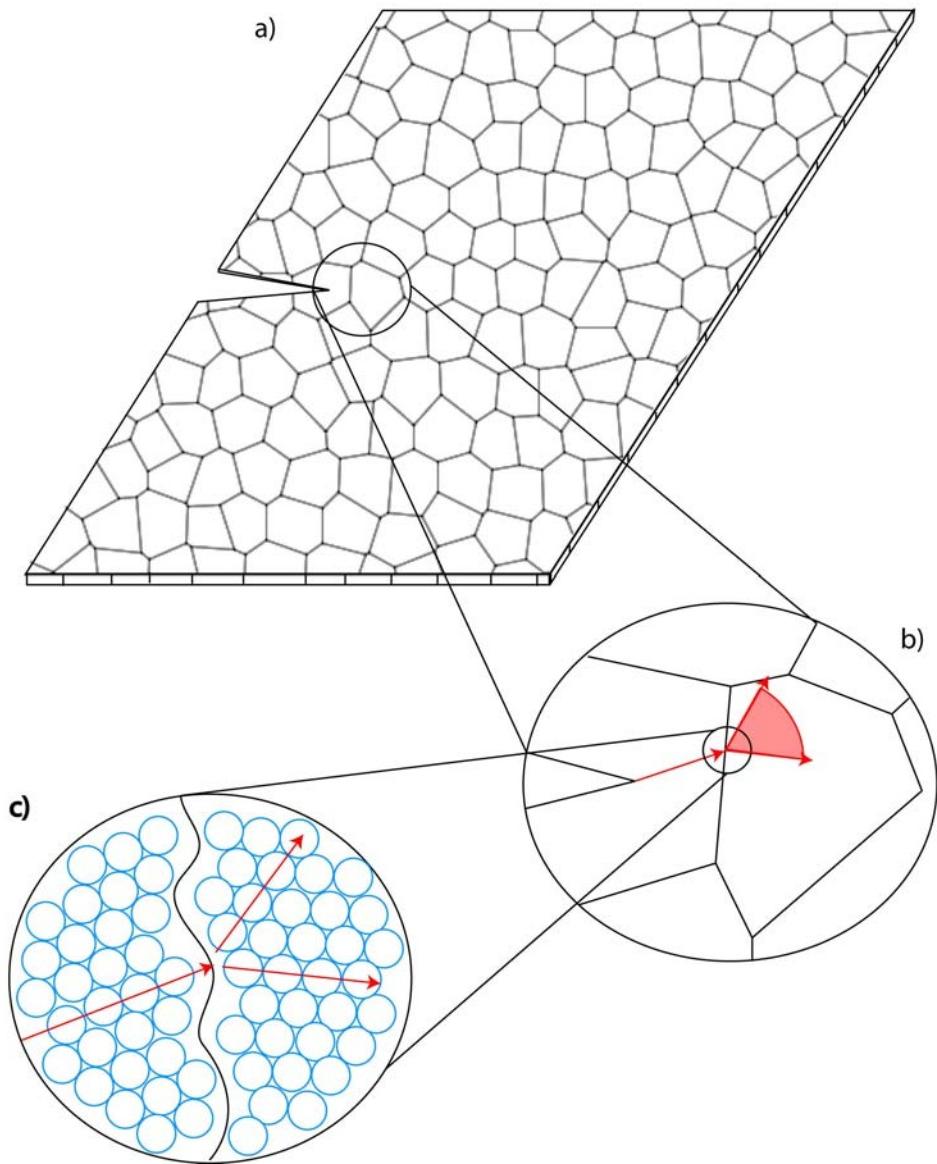
Figure 2-15: A schematic of the microstructure within a columnar, (111) oriented film. The schematic in section a) shows the grain distribution within the polycrystalline film (not drawn to scale). The schematic in section b) is a close-up of the microstructure near the tip of an advancing crack and shows that the crack may deflect as much as 30º one way or another when crossing the grain boundary. The schematic in section c) is a close up of a grain boundary showing atomic distribution within an FCC lattice; this schematic highlights the maximum 30º misalignment of the 110 direction within the (111) plane that can occur across grain boundaries.

Fracture surface viewed head on

Fracture surfaces viewed at an angle
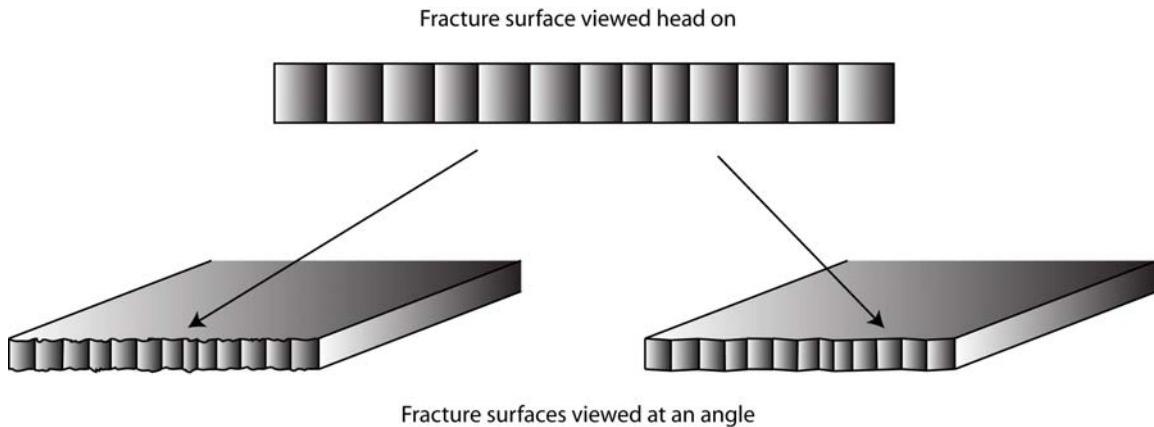
Figure 2-16: Above, the fracture surface is shown as typically imaged – with no tilt; it is impossible to tell what angles are associated with the fracture surfaces. At the angled views beneath it, surfaces associated with the fracture can be seen. At the bottom left, fracture appears to have left jagged and convoluted surfaces behind it, suggesting it followed grain boundaries. At the bottom right, the surfaces are faceted and all angles are less than or equal to 30°, suggesting that crystallographic slip was the failure mechanism.
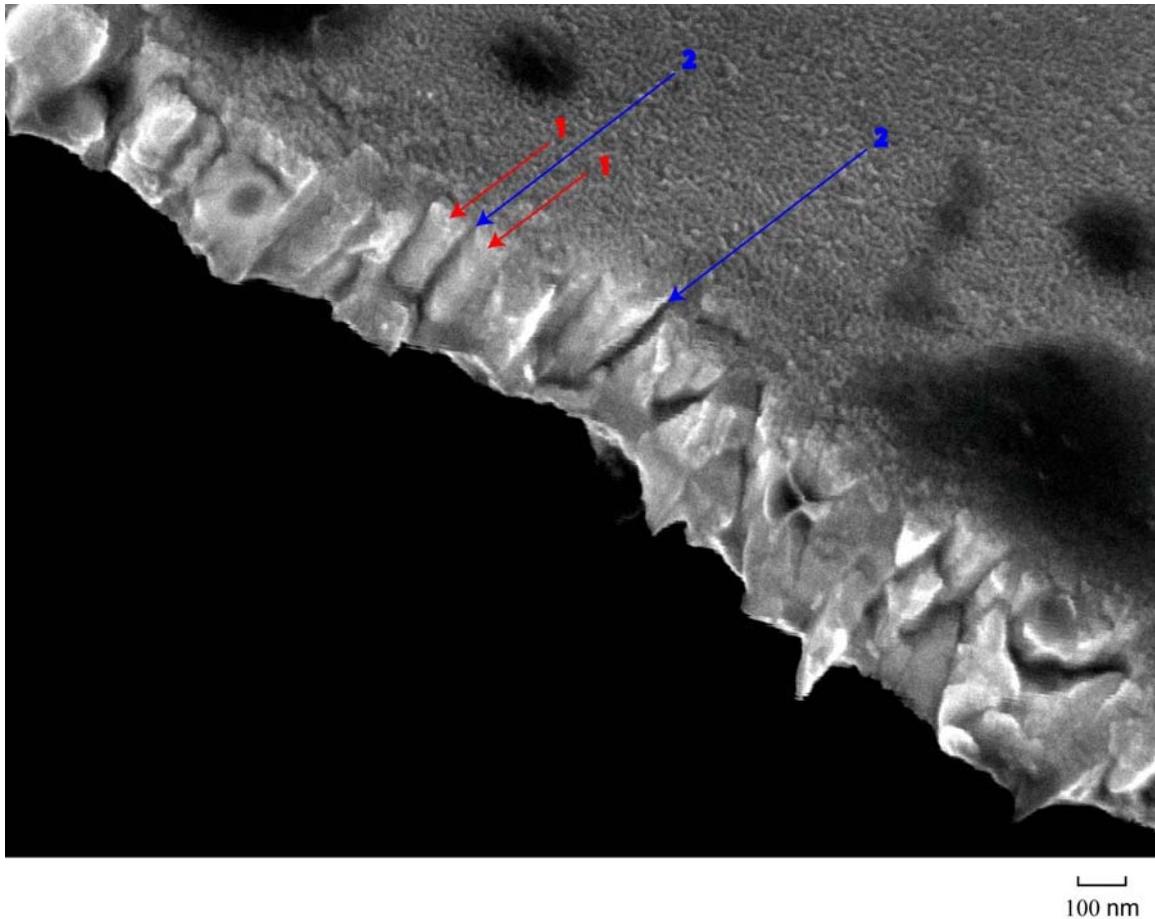
Figure 2-17: An FE-SEM image showing features that are unlikely to be explained by typical crystallographic slip. The features marked "1" point to rounded features in the fracture surface, and those marked by "2" point to facets having larger than 60º offsets. These features would be harder to detect when not viewing the fracture surface at such an acute angle (typical fracture surfaces are observed 'head on', at a 0º angle offset).

4   Summary and Conclusions

A study was conducted to determine the fatigue behavior of a nanocrystalline platinum thin film having a titanium adhesion layer. Microstructural analysis was performed on the samples to characterize their texture and crystallography. One tensile test and four constant stress amplitude fatigue tests were conducted on free standing platinum film specimens containing a central notch. Crack growth behavior and fracture toughness were evaluated from the fatigue tests. Following fracture of the specimens, fracture surfaces were examined with scanning electron microscopes to characterize the causes and mechanisms for the behavior.

1.   Deposition conditions allow the fabrication of flat, 430nm platinum films having primarily (111) oriented columnar grains roughly 25-40 nm in diameter on a 20 nm titanium adhesion layer, in both a free-standing form and on top of a <100> oriented silicon chip. High-resolution TEM of the film established that the material was fully dense (i.e., no nanoscale voids or cracks were found) and no interphase regions between the grains were observed. Energy dispersive spectrometry (EDS), electron energy loss spectrometry (EELS) and secondary ion mass spectrometry (SIMS) of the film confirmed purity of the platinum structural film and the presence of a titanium adhesion layer. Additional spectra collected within the grains, along grain boundaries, near the Ti adhesion layer interface and a top-down scan of the whole microstructure identified Platinum as the only element present, within the detectability limits of the techniques.

8.   A tensile test performed at a rate of 0.1 μm per second was performed on centrally notched sample. An upper bound estimate for the ultimate tensile strength of the platinum using a calculation for the stress concentration of the notch was found to be 3.4 GPa. This upper bound value is consistent with nanoindentation studies [9] and tensile testing studies of the same films [10].The tensile strength value is more than order of magnitude higher than the microcrystalline value of 240 MPa [16] and even as an upper bound, indicates that the films are not inherently weak.

9.   Constant stress amplitude (load ratio $\sigma_{min}/\sigma_{max}= R = 0.1$, sinusoidal waveforms at 1 Hz) fatigue tests were conducted on four samples in laboratory air (22±2°C). During the fatigue crack growth tests, cracks grew symmetrically from the notches and exhibited straight (i.e., nominally mode I) crack paths, and surface distortions associated with the

73

development of the plastic zone were not observed. Final rupture of the specimens occurred on paths that were inclined 45° from the tensile loading axis after an unknown amount of stable, ductile tearing. An extremely limited range of stable fatigue crack growth was observed (< 2 MPa √m), and a least squares curve fit of the data to a power law relationship between the fatigue crack growth rate da/dN and the applied stress intensity factor range, ΔK, (i.e., $da/dN = C(\Delta K)^m$) provided a large power law exponent, m, of ~10.5. This power law exponent of the nanocrystalline platinum is significantly different from its polycrystalline value of ~3.5, and means that the nanocrystalline platinum's fatigue crack growth rate behavior is more similar to a ceramic or ordered intermetallic growth rate behavior than a pure metal.

10. The fracture toughness, K_q, estimated from K_{max} just prior to fracture ranged from 3.45 MPa √m to 4.88 MPa √m for the tested samples. The range of stable of fatigue crack growth and fracture toughness were radically different from the behavior observed for micrograined platinum (K_q = 33.1 MPa √m) [1]. This nearly 10 fold reduction in K_q, is likely to be associated with the nanocrystalline microstructure of the thin films.

11. No crack closure was observed for nanocrystalline platinum. The linearity of the force-displacement plot which was carefully measured during the fourth fatigue test showed no indication of a significant change throughout the life of the fatigued sample. The lack of crack closure is indicative that intrinsic damage mechanisms are the dominant damage accumulation mode, despite a fatigue crack growth curve which is more similar to that of brittle materials where extrinsic toughening is dominant.

6. Scanning electron microscopy of the failure surfaces of the fatigue specimens revealed that the fatigue crack path from the near-threshold regime (i.e., growth rates below 10^{-9} m/cycle) up to ~2×10^{-7} m/cycle was *intergranular*, and secondary cracking was observed. As the cracks accelerated to ~3×10^{-7} m/cycle, they gradually transitioned to a transgranular path. During this transition, a fine ridge associated with localized (transverse) necking of the material developed in the center of the failure surfaces, parallel to the crack propagation direction. This transgranular mode with a central ridge persisted until final fracture occurred at K_{max} ~4 MPa √m. The observation of intergranular fatigue crack paths in a refractory, noble metal such as platinum demonstrates that fatigue crack growth mechanisms that operate in micrograined metals will not always persist as the grain size of the material is reduced to the nanoscale. This

behavior may become more important as nanograined alloys are developed and the high strength of the grains further biases fatigue damage segregation to grain boundaries.

5   Nanoindentation Methods

A series of indents were performed on the platinum films. Details about the Oliver-Pharr method used to analyze the indentation tests are given in Section 5.2. Details about the experimental methods used in the indentation tests are given in Section 5.3. As regards error analysis and error depiction graphs, all stated errors and error bars represent the standard error for all indents of a given testing condition [26], except where noted otherwise.

5.1   Fabrication and Characterization

Given the importance of surface conditions to nanoindentation, more involved analyses were used.   The surface roughness average, S_a, which represents the average height/depth of surface features, was measured from a tapping mode atomic force microscopy (AFM) image, where the scan rate was 0.73 Hz on a 10 by 10 μm (256 by 256 pixels) region unaffected by indentation tests. The S_a parameter of the surface was 1.3 nm, as determined through the following equation:

$$S_a = \frac{1}{M} \sum_{i=0}^{M-1} |z_i - \mu|$$

5-1

where M was the number of pixels in the image, i was the pixel number, z was the height of the pixel, and μ was the average height of the image. Alternatively, the surface roughness root mean square, S_{RMS}, was found to be 3.2 nm, where S_{RMS} was defined as:

$$S_{RMS} = \sqrt{\frac{1}{M} \sum_{i=0}^{M-1} |z_i - \mu|^2}$$

5-2
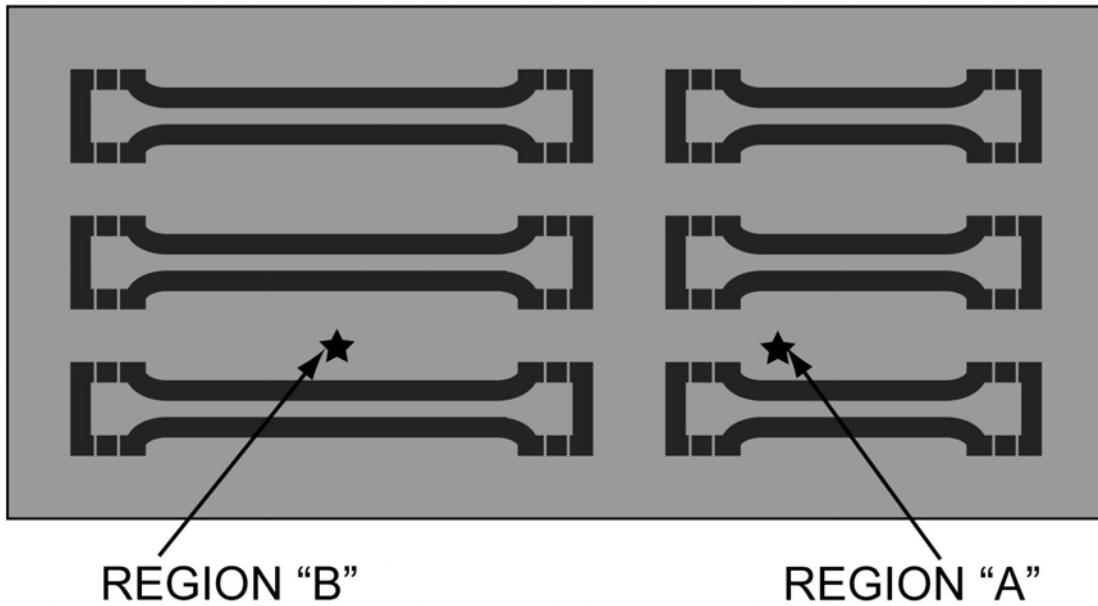
Figure 5-1Schematic of 430 nm thick platinum film on {100} silicon substrate. Indents at 1, 10 and 100 μN/s were performed in region "A". Indents at 10, 25, 50, 75, and 100 μN/s were performed in region "B". Indentation drift measurement tests were also performed in region "B". Black regions indicate areas with no platinum where the silicon substrate was also etched to release the tensile bar samples. Gray areas show areas with platinum fully adhered to the silicon substrate.

5.2   Analysis Methodology

The Oliver-Pharr method was used to evaluate the data. Through the Oliver-Pharr method, the reduced elastic modulus, E_r, and hardness, H, can be calculated. To assure the best accuracy, several corrections must be made to the Oliver-Pharr method. Specifically, area function, compliance, and pile-up corrections must be made to obtain reliable results. The specifics of the implementation of the Oliver-Pharr method and the techniques for correcting the area function, compliance and pile-up will be detailed in this section.

5.2.1   Oliver-Pharr Implementation

In this section, the implementation of the Oliver-Pharr analysis method is discussed. To analyze the instrumented indentation data, user-created Matlab® (The MathWorks, Massachusetts) scripts were created. First, the raw data was read in from files created by the Hysitron Triboscan software (Triboscan®, Hysitron Inc.). The raw displacements were already drift corrected by the Triboscan software so that:

$$h' = h - \dot{h}_{drift} \cdot t$$

5-3

where h' was the drift corrected displacement, h was the raw displacement, $\dot{h}_{drift}$ was the drift rate, and t was the time. The raw displacements are also compliance corrected, so that

$$h'' = h' - C_m \cdot P$$

5-4

where h'' was the drift and machine compliance corrected displacement, h' was the drift corrected displacement, C_m was the machine compliance, and P was the force. The procedure to determine the machine compliance is discussed in Section 5.2.3. The Triboscan software set $t{=}0$ as the start of the test and $h{=}0$ when 2 consecutive data points have forces above the user-determined preload. For all the indentation tests in this study, the preload was set to 1.0 μN.

The data was then parsed by time to find the loading, hold, and unloading portions of each indentation test. Once the unloading period was identified, the data was searched for the maximum force, P_t. The maximum indentation depth, h_t, was taken as the displacement at the maximum force. After the data is parsed, the unloading curve is then fit using Matlab's ® *nlinfit* script. To fit the equation, the top 5 and bottom 20 percent of the data removed to eliminate artifacts due to tip stiction and friction issues that can occur at those points in the indentation tests. The residual depth parameter, h_r, was found from fitting the equation (as opposed to using

the displacement when *P*=0 on unloading). The stiffness of the material, *S*, was found by taking the displacement derivative and evaluating it at *h=h_t*.

From the stiffness, maximum force, and maximum depth, the contact depth, h_p, was calculated. The maximum depth used was from parsing the data (as opposed to extrapolation). The intercept factor, ε, was set at 0.75. The contact depth represents the length of the indenter tip that is in contact with the sample material. However, because the material "piled-up" around the indenter tip, the contact depth from the Oliver-Pharr method did not accurately represent the tip-sample contact. This was corrected by calculating the pile-up height, h_{pu}, and adding this value to the contact depth. The methodology for calculating the pile-up height is discussed further in the following sections. The contact depth (with pile-up included) was then used to calculate the projected contact area. The contact area as a function of contact depth was calibrated on a known reference standard was of a power law form. Further details of the contact area calibration are given in the following sections. Finally, the contact modulus and hardness can be determined with knowledge of both the contact area, the contact stiffness, and the maximum force. When calculating the contact modulus, the shape parameter, β, was set as 1 for a conospherical tip.

All data fitting was accomplished using *nlinfit* tool in Matlab®, except for the linear fit for the machine compliance calibration. The linear fit was found from a least squares program written in Matlab code based on the method described in reference [27].

5.2.2   Area Function Correction

The contact area A_c as a function of the plastic (or contact), h_p , was calibrated through a series of indents with maximum target displacements ranging from 10 to 300 nm in 10 nm increments on Corning C1737F glass, where the reduced elastic modulus of 74.5 GPa was a well-known parameter [28]. Ten indents were performed at each maximum target displacement, where a displacement-controlled mode was used to move the indenter tip to the maximum displacement at a constant loading rate of 10 nm/s, hold it at the maximum displacement for 10 s, and then unload it at the same constant rate as during loading. The indents were placed on a 17 μm square grid, to ensure that the spacing between indents was greater than ten times the lateral extent of the largest indent. Since the reduced modulus of Corning C1737F glass was well-known, the relationship between stiffness, area, and indenter geometry was inverted to solve for the contact area. The contact area was then be related to the plastic (or contact) indentation depth, h_p, which was defined as the vertical height of the indenter tip that was in contact with the sample at the start of unloading. The relationship between contact area and contact depth was fitted to the form:

$$A_c = C_0 h_p^2 + C_1 h_p + C_2 h_p^{1/2} + C_3 h_p^{1/4} + C_4 h_p^{1/8} + C_5 h_p^{1/16}$$

5-5

where C_i were the area function coefficients. Matlab's ® *nlinfit* was used to fit the above equation.

5.2.3 Compliance correction

The raw data were also corrected for machine compliance, C_m, which was determined from the same tests on C1737F used to determine the area function. The machine compliance was set as the y-axis intercept of the linear fit to the plot of $1/S$ versus $1/h_p^{1/2}$:

$$\frac{1}{S} = b \frac{1}{\sqrt{h_p}} + C_m$$

5-6

where b was a fitting parameter. The y-axis intercept was found using a least squares method (as in [27]) to fit a linear line of the contact depth versus stiffness. Only contact depths greater than 50 nm were used to prevent larger scatter in the data at lower indentation depths from acting like a lever on the linear fit. Once the y-intercept was obtained, the raw displacement was then adjusted for the new compliance by changing the displacement with the following relationship

$$h' = h - C_m P$$

5-7

where h' was the corrected displacement, h was the raw displacement and P was the raw force. The area function calibration was performed again with the new displacement values. This data was again calibrated for machine compliance. This process was repeated iteratively until the changes in the machine compliance from iteration to iteration were less than 0.01 nm/mN, which is less than 0.5% of the total machine compliance of 2.36 nm/mN. The total machine compliance was taken as the summation of the iterated machine compliances, and the area function was taken as the values obtained when the raw displacement data is corrected by the total machine compliance.

5.2.4 Pile-up correction

The Oliver-Pharr method is very useful for describing systems where the material around the indenter tip "sinks-in". However, it cannot accurately determine the contact area when the material around the indenter tip "piles-up" due to plastic flow [29]. In order to obtain accurate material properties, the pile-up height must be included in the plastic indentation depth, especially

for deeper indents. To determine the pile-up height, h_{pu}, the *in-situ* image obtained immediately after an indentation test was used. First, the image was flattened using the *plane correction* tool in Scanning Probe Image Processor (SPIP) software (Image Metrology A/S, Denmark) where a 3rd order polynomial fit was used over the entire image, and the bearing height was set as zero. A Matlab computer program was written to find the minimum point on the image, and then search for maxima by parsing outwards from the minimum point along eight evenly spaced radii using Matlab's *min* and *max* functions. These maxima along with the maxima from each of the indent images for the same test conditions were averaged to determine the pile-up height. Average pile-up heights for each indentation condition that were smaller than 4 nm were discarded, which was a conservative way of eliminating all pile-up heights that were larger than the S_{RMS}. This ensured that all pile-up heights captured were indicative of pile-up and not of the material's surface roughness. To verify that the blunt probe tip did not cause distortion in the image, a 550 and 3100 μN image was compared to images taken of the same indent with an atomically fine tapping mode cantilever with a Digital Instruments Dimension 3100 Atomic Force Microscope (AFM). The images obtained from the AFM were 3.5 by 3.5 μm, with a pixel density of 350 by 350 (zoomed in from a larger image). A scanning rate of 6.72 μm/s with a frequency of 0.66 Hz was used. The pile-up heights determined from the *in-situ* image and from the AFM image were within 10% of each other (less than 2 nm variation). Given the accuracy of the *in-situ* images, they were used for the pile-up correction because the blunt tip shape effectively represented the pile-up height maxima.
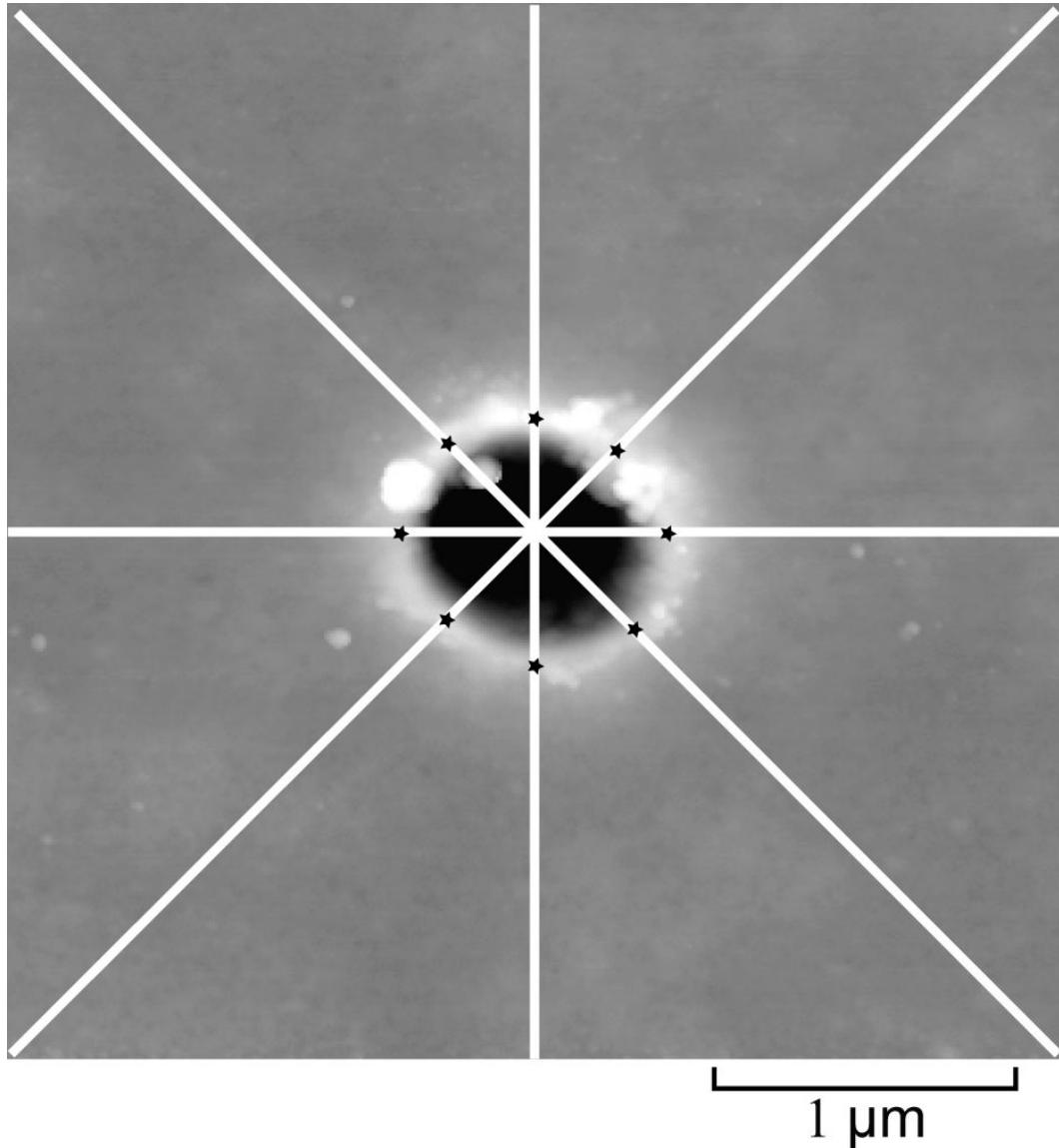
Figure5-3 AFM image of an indent performed on 430 nm platinum film at 100 μN/s loading rate with a maximum load of 3100 μN. The lines radiating outward show the parse lines to find the maximum pile-up height along the line (shown with black stars).

5.3   Nanoindentation testing methodology

Several different tests were run on the platinum thin film to determine the time dependent properties. To determine if the platinum films exhibited a strain rate sensitivity or viscoelastic response, symmetric loading rate tests were performed at a variety loading rates. By performing asymmetric tests as well, the influence of loading history on the Oliver-Pharr analysis can be evaluated. Finally, some system limitations were evaluated by performing a variety of drift rate tests. The methods used for each of these tests are discussed in the following sections. A summary chart of all indents performed on the platinum sample is presented in Table 5-1.

5.3.1   Symmetric loading rate tests

Force-controlled indentation tests were performed using diamond, conospherical indenter tip with a nominal radius of 500 nm. The force on the indenter tip was increased at a constant loading rate, held at the maximum force for 10 s, and then unloaded at the same rate as during loading. For these indents, maximum forces of 550, 1500, and 3100 μN were used, and loading/unloading rates of 1, 10 and 100 μN/s were used for each peak load condition. These trapezoidal loading functions are shown in Figure 5-, Figure 5-5 and 5-6. The maximum forces were chosen to correlate to indentation depths that were approximately 7, 17, and 35 percent of the film thickness. Ten indents were performed for each combination of maximum force and loading rate. The indents were placed on an 11.5 μm square grid, to ensure that the spacing between indents was greater than ten times the lateral extent of the largest indent (thereby preventing interaction between individual measurements).

To evaluate spatial variations in the material, the 10 and 100 μN/s loading/unloading rates were repeated in a disparate geographic region of the platinum film that was several millimeters away from the initial test site. The initial test site is shown as region "A" in Figure 5-1, and the new tests were performed in region "B". Three additional loading/unloading rates were also explored in this second region. The tests were still performed in force-control with loading/unloading rates of 25, 50, and 75 μN. Again, ten indents were performed at 550, 1500, and 3100 μN maximum forces for each loading rate. Plots of the loading functions for each test are shown in Figure , Figure 5-, and Figure 5-9. The indents were still spaced on an 11.5 μm square grid.

During the indentation tests, a preload of 1.0 μN was used to determine the location of the surface. Once on the surface, the indenter was held for 60 s at 1.0 μN. The last 30 s of this hold time were used to calculate the instrument's displacement drift rate. Displacement drift rates in all tests were found to be between ±0.1 nm/s. Immediately prior to the drift measurement and

immediately following the indentation test, an *in-situ* image of the topography indentation surface area was obtained using the indenter tip as a probe. The image size was set as 1.5 by 1.5, 2.5 by 2.5 and 3.5 by 3.5 μm for the 550, 1500 and 3100 μN maximum indentation force conditions, respectively (all images were 256 by 256 pixels). These images were used to verify that the indentation areas for all indents were free of debris or other gross defects prior to the indentation test and to quantify the amount of piled-up around the indenter tip during the indentation test.

5.3.2   Asymmetric loading rate tests

To evaluate the role of loading history in the Oliver-Pharr analysis of instrumented indentation tests results, asymmetric loading tests were performed. The tests were again force-controlled with a nominal 500 nm radius diamond, conospherical indenter tip. Two separate asymmetric tests were performed at maximum forces of 550, 1500, and 3100 μN. The first increased the force at a constant rate of 100 μN/s, held at the maximum force for 10 s, and the decreased the force at a constant rate of 10 uN/s. The second was the inverse: the force was increased at a constant rate of 10 μN/s, held for 10 s, and decreased at a constant rate of 100 μN/s. The force function for these two tests are shown in Figure 5-10 and Figure . Ten indents were performed at each loading condition and maximum force. As in the symmetric tests, the indents were placed on an 11.5 μm square grid to ensure sufficient spacing between indents. These indents were also performed in region "B" shown in Figure . All the parameters used for surface sensing, drift measurement, and in-situ imaging were the same as above for the symmetric tests.

5.3.3   Drift measurement tests

Given the limitations of extrapolating a short-term displacement drift correction measurement to a long-duration experiment, an extended evaluation of the system stability was performed. Indentation tests were performed with 10 μN/s loading and unloading rate and a 3000 s hold time. The first test had a maximum force of 10 μN. A 1 μN force was used to sense the surface. The drift rate was determined by holding on the surface at 1 μN for a 60 s drift monitoring time. The last 30 s were the drift analysis time used to find the drift rate. Five indents were performed with these conditions, with an hour hold before each indent.

However, the preload, drift monitor and analysis time, and maximum force can affect the results seen. If the preload is not sufficiently high enough to accurately sense the material surface, then false drift rates will be recorded. To eliminate this as a source of error, three additional tests were done as above, except the preload was increased to 2.0 μN. If the drift monitor and analysis time are not long enough, the system would not properly stabilize, and the drift rate would not

accurately reflect the drift rate during the actual experiment.   To verify that any changes in drift rate were not due to an insufficient drift monitoring and analysis time, a set of three indents were performed as in the first set above, but with the drift monitor time increased to 500 s and the drift analysis time increased to 60 s. The preload was 1.0 µN during this third test set. Finally, a high maximum force can cause plastic deformation and creep. The creep would be undistinguishable from system drift. In order to assure that creep does not occur, two additional tests sets were performed.   Maximum forces of 1.0 and 2.0 µN were used with 1.0 and 2.0 µN preloads, respectively. The drift monitor time was 60 s and the drift analysis time was 30 s for both tests. The hold periods of the resulting force-displacement curves from all above tests were then used to quantify the long-term displacement drift of the system. All of the above indentation force-time curves can be seen in Figure 5-9 and a summation of the drift measurement methods can be seen in Table 5-2.

Maximum Force (μN)	Loading Rate (μN/s)	Hold Time (s)	Unloading Rate (μN/s)	Preload (μN)	Drift Monitor Time (s)	Drift Analysis Time (s)	Region	# of Indents
550	100	10	100	1	60	30	A	10
1500	100	10	100	1	60	30	A	10
3100	100	10	100	1	60	30	A	10
550	10	10	10	1	60	30	A	10
1500	10	10	10	1	60	30	A	10
3100	10	10	10	1	60	30	A	10
550	1	10	1	1	60	30	A	10
1500	1	10	1	1	60	30	A	10
3100	1	10	1	1	60	30	A	10
550	10	10	10	1	60	30	B	10
1500	10	10	10	1	60	30	B	10
3100	10	10	10	1	60	30	B	10
550	10	10	100	1	60	30	B	10
1500	10	10	100	1	60	30	B	10
3100	10	10	100	1	60	30	B	10
550	25	10	25	1	60	30	B	10
1500	25	10	25	1	60	30	B	10
3100	25	10	25	1	60	30	B	10
550	50	10	50	1	60	30	B	10
1500	50	10	50	1	60	30	B	10

3100	50	10	50	1	60	30	B	10
550	75	10	75	1	60	30	B	10
1500	75	10	75	1	60	30	B	10
3100	75	10	75	1	60	30	B	10
550	100	10	100	1	60	30	B	10
1500	100	10	100	1	60	30	B	10
3100	100	10	100	1	60	30	B	10
550	100	10	10	1	60	30	B	10
1500	100	10	10	1	60	30	B	10
3100	100	10	10	1	60	30	B	10
10	10	3000	10	1	60	30	B	5
10	10	3000	10	2	60	30	B	3
10	10	3000	10	1	500	60	B	3
2	10	3000	10	2	60	30	B	1
1	10	3000	10	1	60	30	B	1

Table 5-1 All indents series performed on platinum film, with respective maximum forces, loading and unloading rates, hold times, and drift monitoring and analysis times with number performed in either region "A" or "B".
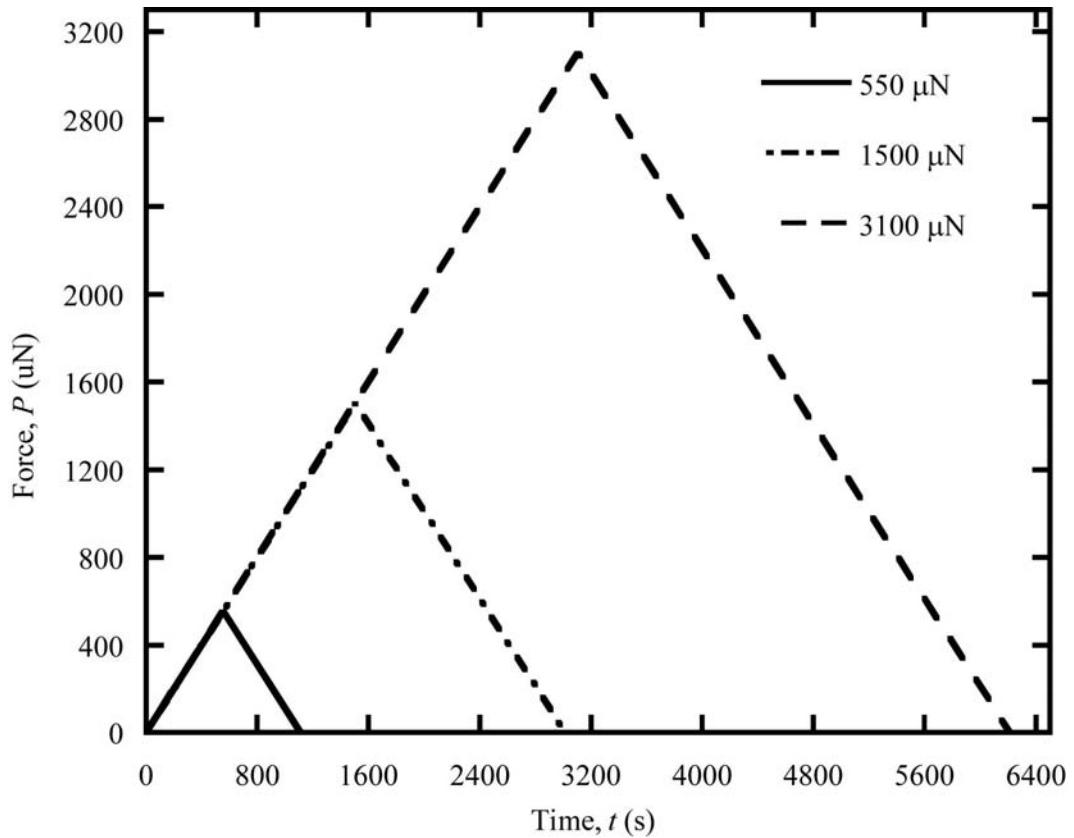
Figure 5-3 Force-control loading profile for a series of 1 μN/s indents with maximum loads of 550 (solid line), 1500 (dash-dot line), and 3100 (dashed line) μN. While these lines represent the command function and are not experimental data, the system control maintained the force to within 2 μN of the command function.
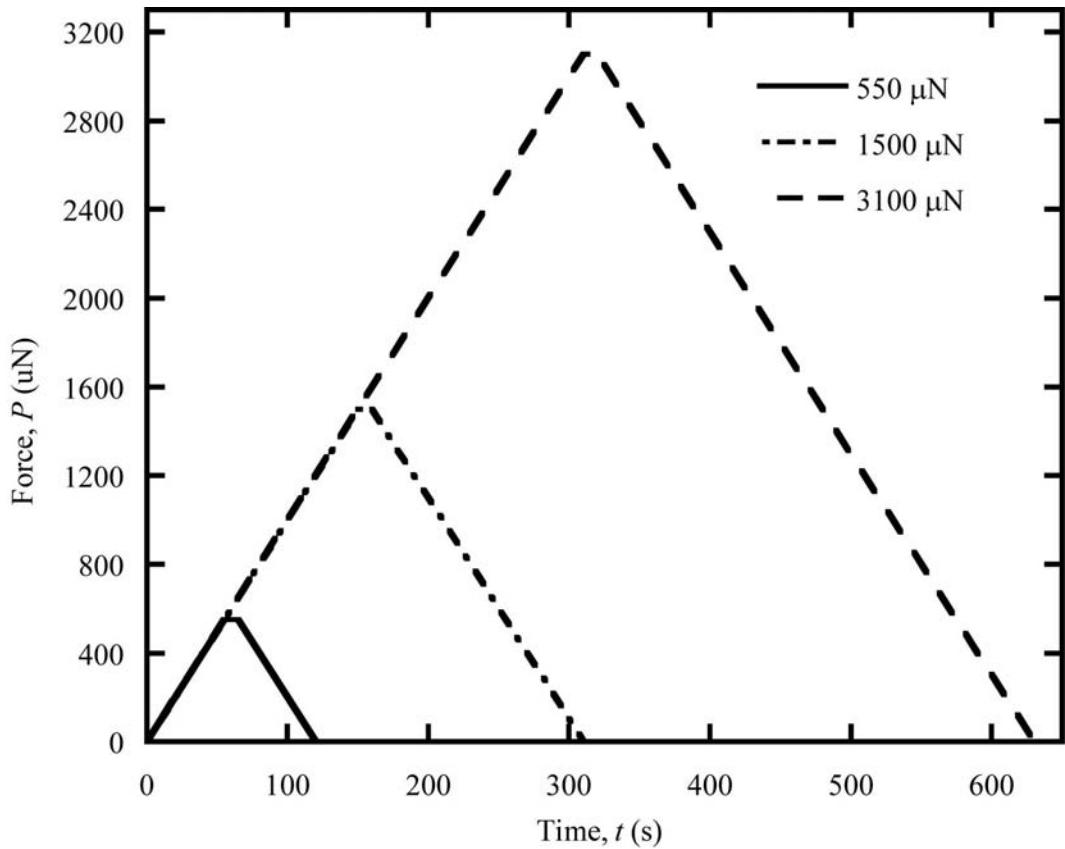
Figure 5-4 Force-control loading profile for a series of 10 μN/s indents with maximum loads of 550 (solid line), 1500 (dash-dot line), and 3100 (dashed line) μN. While these lines represent the command function and are not experimental data, the system control maintained the force to within 2 μN of the command function.
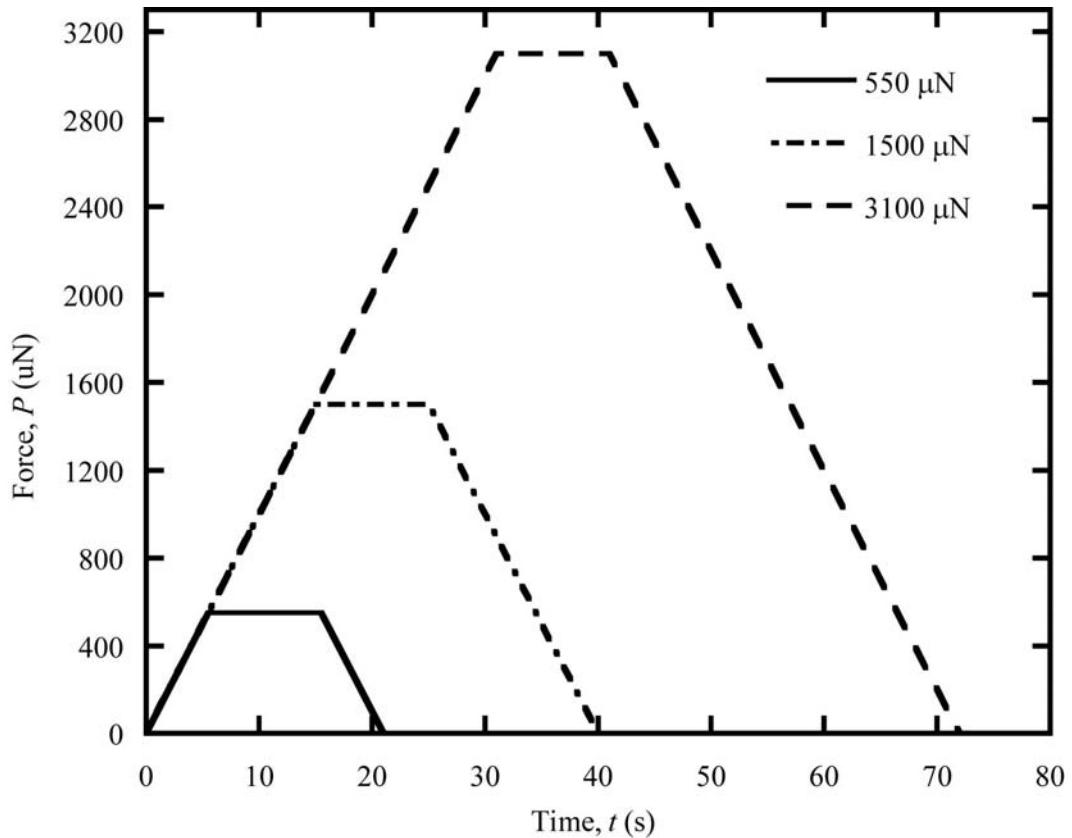
Figure 5-5 Force-control loading profile for a series of 100 μN/s indents with maximum loads of 550 (solid line), 1500 (dash-dot line), and 3100 (dashed line) μN. While these lines represent the command function and are not experimental data, the system control maintained the force to within 2 μN of the command function.
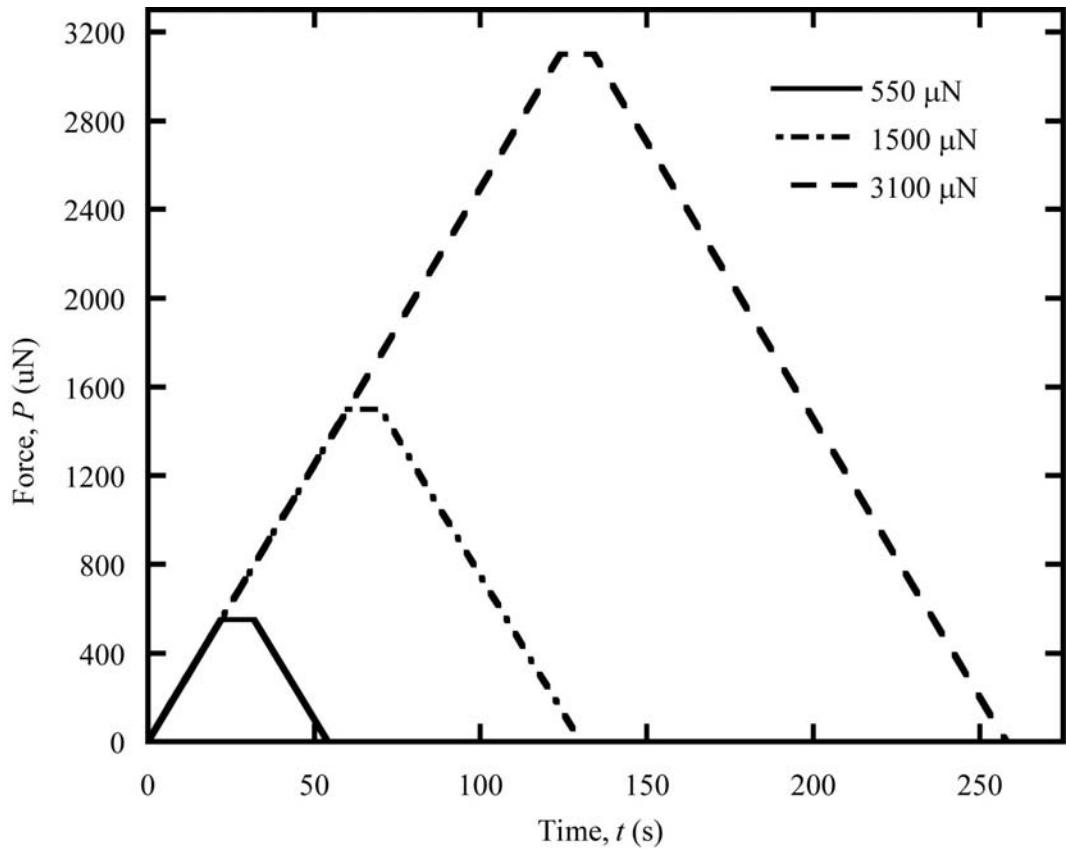
Figure 5-6 Force-control loading profile for a series of 25 μN/s indents with maximum loads of 550 (solid line), 1500 (dash-dot line), and 3100 (dashed line) μN. While these lines represent the command function and are not experimental data, the system control maintained the force to within 2 μN of the command function.
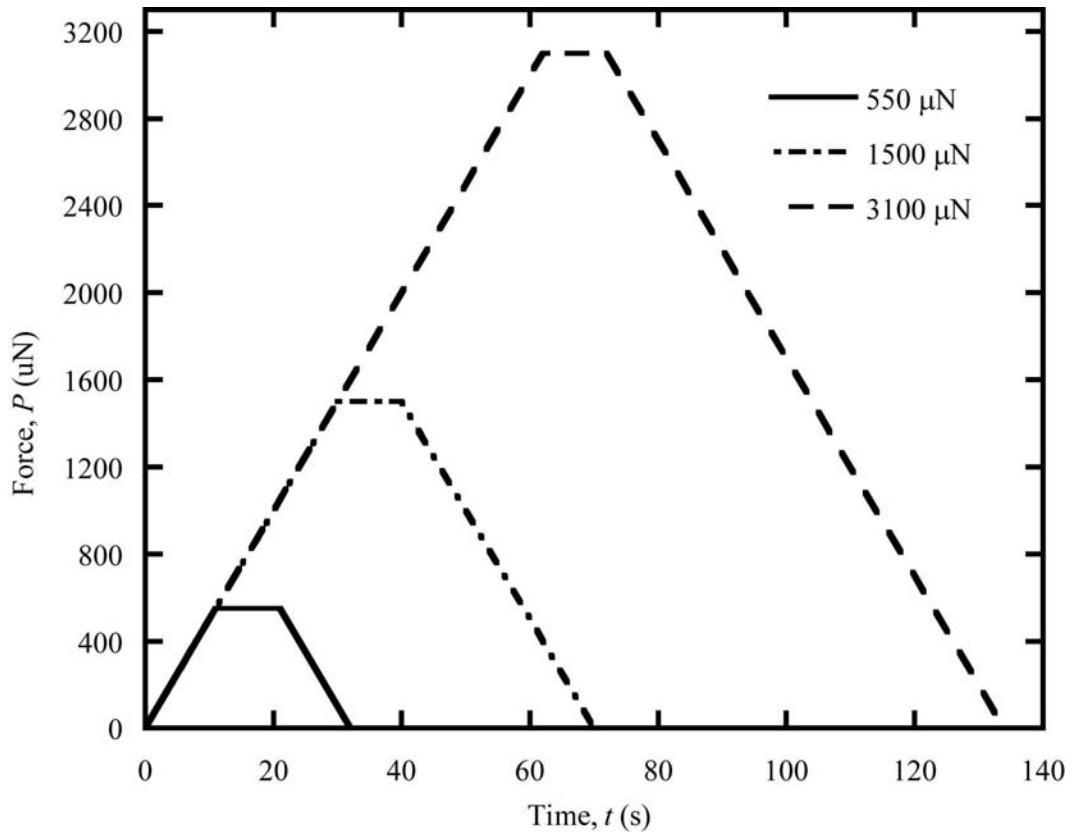
Figure 5-7 Force-control loading profile for a series of 50 μN/s indents with maximum loads of 550 (solid line), 1500 (dash-dot line), and 3100 (dashed line) μN. While these lines represent the command function and are not experimental data, the system control maintained the force to within 2 μN of the command function.
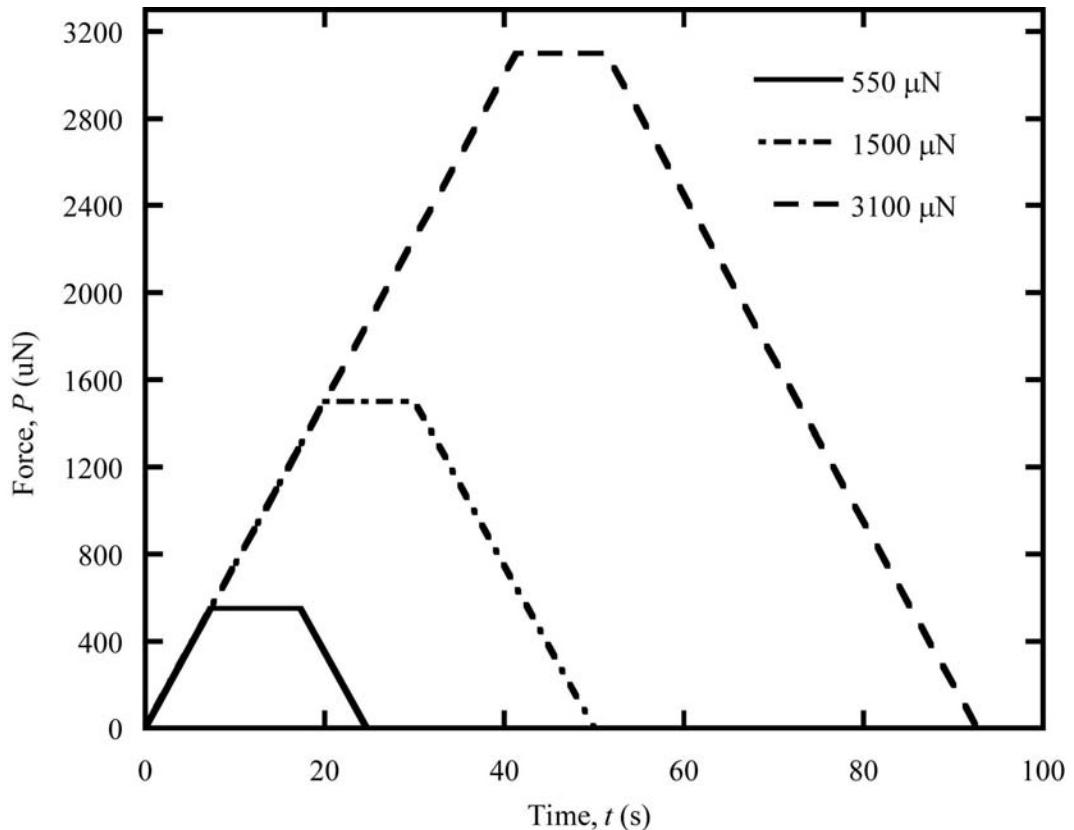
Figure 5-8 Force-control loading profile for a series of 75 μN/s indents with maximum loads of 550 (solid line), 1500 (dash-dot line), and 3100 (dashed line) μN. While these lines represent the command function and are not experimental data, the system control maintained the force to within 2 μN of the command function.
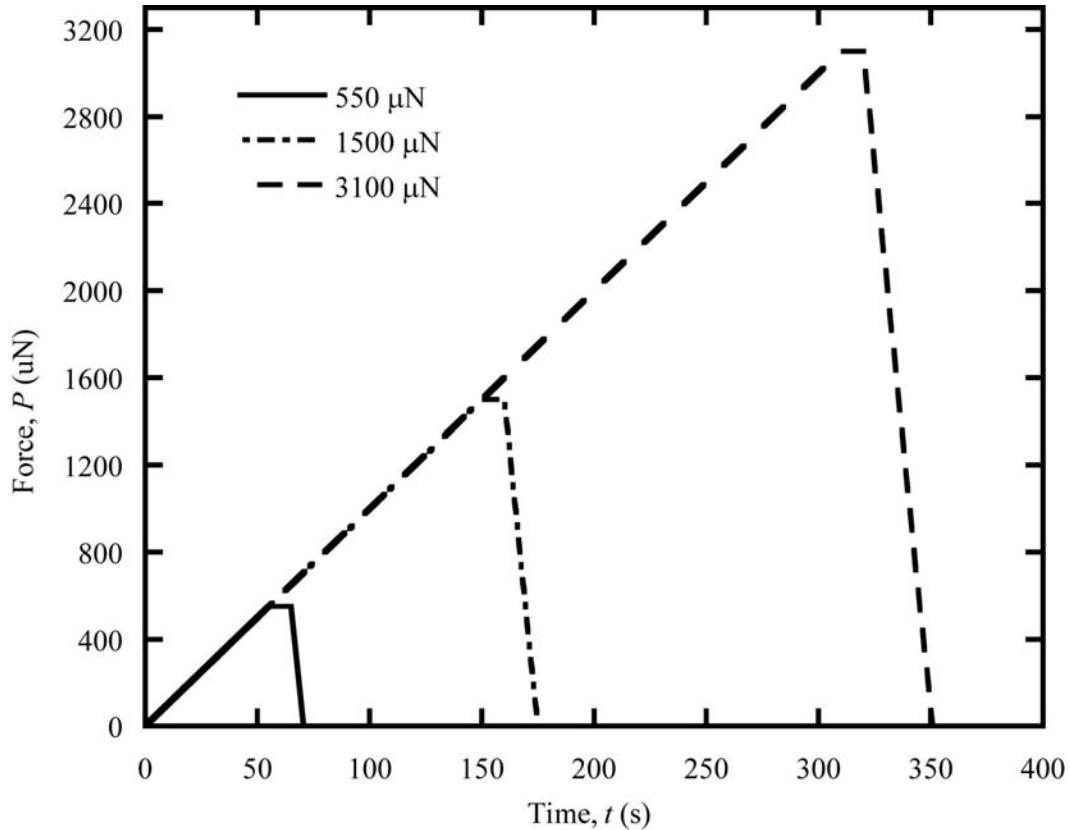
Figure 5-9 Force-control loading profile for a series of indents with a 10 μN/s loading rate and 100 μN/s unloading rate. Maximum loads of 550 (solid line), 1500 (dash-dot line), and 3100 (dashed line) μN are shown. While these lines represent the command function and are not experimental data, the system control maintained the force to within 2 μN of the command function.
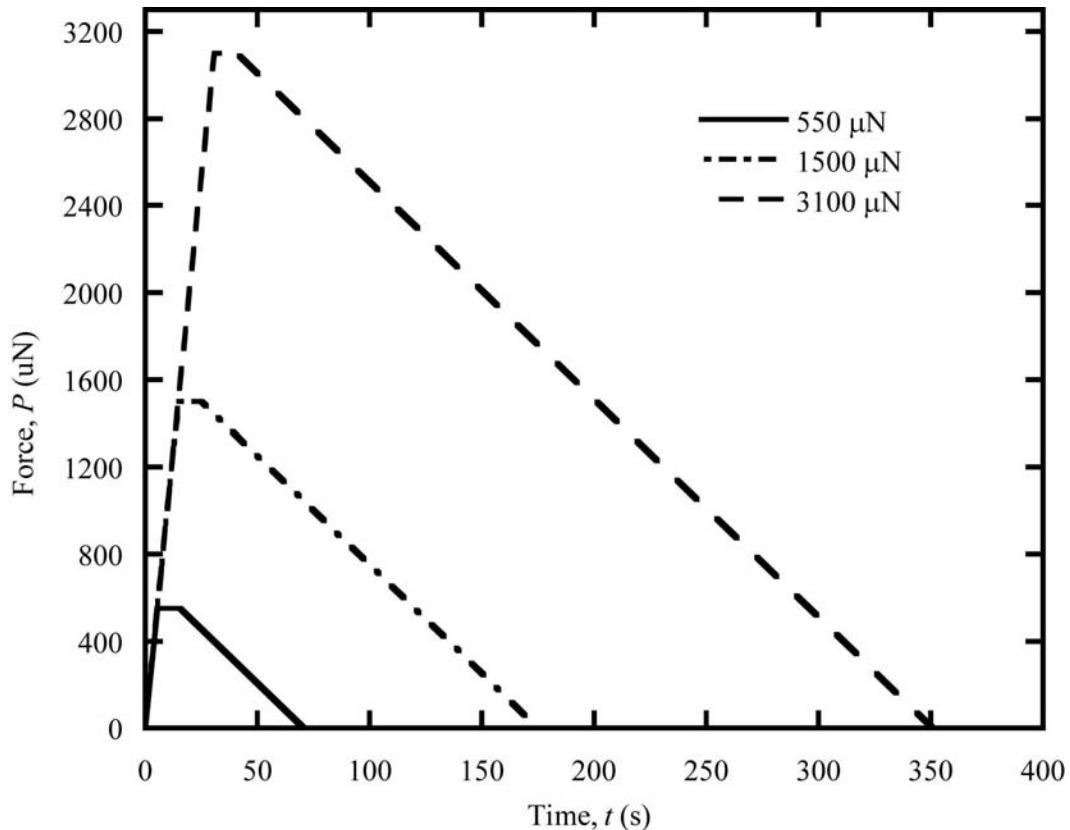
Figure 5-10 Force-control loading profile for a series of indents with a 100 μN/s loading rate and 10 μN/s unloading rate. Maximum loads of 550 (solid line), 1500 (dash-dot line), and 3100 (dashed line) μN are shown. While these lines represent the command function and are not experimental data, the system control maintained the force to within 2 μN of the command function.
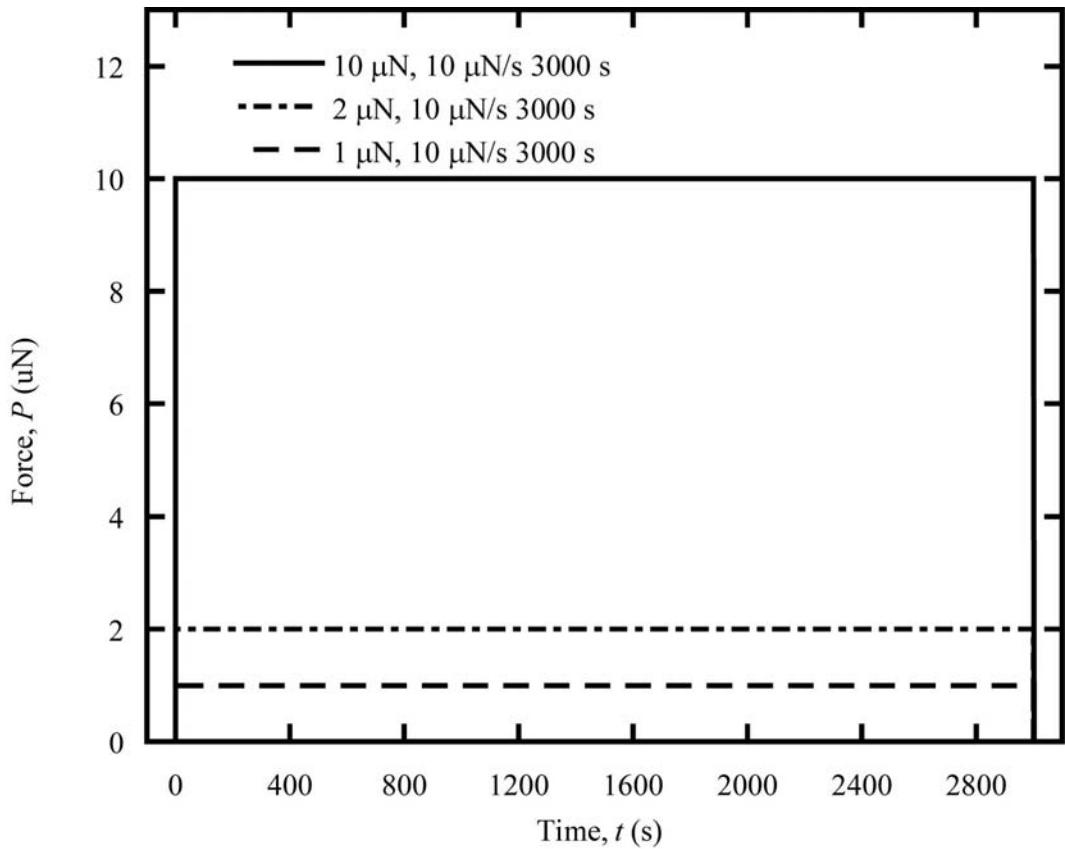
Figure 5-11 Force-control loading profile for a series of drift measurement tests. The solid line shows the indents that had a maximum force of 10 μN. At this maximum force, five indents were done with a 1.0 μN preload, 60 s drift monitor time and 30 s drift analysis time. Three indents were done with a 2.0 μN preload, 60 s drift monitor time, and 30 s drift analysis time. Three additional indents were done with a 1.0 μN preload, 500 s drift monitor time, and 60 s drift analysis time. The dashed-dotted line shows the one indent that was performed with a maximum force of 2.0 μN. The preload was 2.0 μN, and the drift monitor and analysis times were 60 and 30 s, respectively. The dashed line shows the one indent that was performed with a maximum force of 1.0 μN. The preload was 1.0 μN, and the drift monitor and analysis times were 60 and 30 s, respectively.

6   Nanoindentation Results and Discussion

Symmetric and asymmetric tests were performed in two different regions of the platinum film. The results are examined for viscoelastic responses and spatial variations in mechanical properties. Additionally, anomalous results from a test that required a long test time prompted an investigation into the validity of drift rate measurements. Reasons for the anomalous results, specifically accumulated drift and variable drift rates, are evaluated.

6.1   *Symmetric Test Results*

Symmetric tests were performed in two different regions over a variety of loading rates. Five different rates (10, 25, 50, 75, and 100 μN/s) were examined to try to determine the viscoelastic response of the material. These tests were performed in two different regions. When the test results from the different regions did not correlate to each other, possible spatial variation causes were explored.

6.1.1   Region "A" findings

The symmetric tests performed in region "A" of Figure were first analyzed via the methods above. After a traditional Oliver-Pharr analysis of the data was performed, factors that could have affected the results were evaluated to determine if the elastic moduli reported by previous studies were experimental artifacts or truly low moduli. To start, we determined the effect that anisotropy, pile-up, substrate constraints, microcracking and/or delamination, and viscoelastic behavior could have on the experimental results. Traditional Oliver-Pharr analysis of the data showed a reduced elastic modulus, E_r, of 181 GPa at the shallowest depths, as shown in 6-1. Assuming the Hashin-Shtrikman polycrystalline aggregate bounds for Poisson's ratio of 0.396 [30] (as suggested from application of Vlassak-Nix solution Vlassak [31, 32]), the Young's modulus was 153 GPa. Previous nanoindentation studies of thin film platinum reported the Young's elastic modulus as 160 GPa [33-35] (in reference [36], only the contact modulus and a modified Gao substrate solution were presented, with extremely varying results). This study's Young's modulus of 153 GPa was 4.5 percent below other indentation tests. Tensile testing of similarly processed platinum films was performed by Sharpe and his research group at Johns Hopkins University, and they found the elastic modulus of the platinum film to be 140 GPa [37].

While the reduced modulus correlated well with other testing methods, the reported elastic moduli for this and the other indentation tests in the literature were much lower than the expected values for either bulk polycrystalline platinum or <111> textured platinum. As noted in the

introduction, the average of the polycrystalline aggregate Hashin-Shtrikman bounds of the Young's modulus for pure platinum was calculated to be 177.5 GPa [30]. The indentation of a <111> textured film should be 1.6 percent above this polycrystalline aggregate value [31, 32] (180 GPa). The value obtained for Young's modulus in this study (153 GPa) were 13.8 and 15 percent off the Hashin-Shtrikman bounds and the <111> orientation indentation modulus, respectively. The Young's moduli for the indentation tests reported in this study were calculated using the polycrystalline aggregate value for Poisson's ratio from application of the Vlassak-Nix solution [31, 32] Similarly, tensile tests conducted on the same films oriented such that the tensile axis was within the {111} were 24.3 percent below the expected Young's modulus (~185 GPa). In this manner, all elastic moduli values reported were lower than what elasticity theory predicted. However, factors such as pile-up or delamination, could have reduced apparent elastic modulus of the films.

The indentation modulus could also be affected by a lack of inclusion of pile-up in the calculations. The inclusion of pile-up increased the contact depth, thus increasing the contact area. Since the stiffness remains the same, the elastic modulus is decreased when pile-up heights are included. For the platinum sample, it was found that at the shallowest indentation depths, pile-up height was not an important effect since the pile-up height was within the surface roughness. Therefore, despite the fact that pile-up was not included in the other studies [34-36, 38], they should have correlated well with the shallowest indentation depths, where pile-up height was non-existant or indistinguishable from the surface roughness. However, when evaluating post-indentation test *in-situ* images of the indentation area for deeper indents, it became clear that substantial amounts of pile-up existed around the indenter tip (Figure 6-2). The piled-up material surrounding the indent represented a substantial percentage of the indentation depth, and could thus not be neglected when using the Oliver-Pharr method. At the deepest indentation depths, the pile-up height averaged 19.5 percent of the plastic indentation depth. The pile-up height as a function of normalized indentation depth is shown in Figure 6-3. The values obtained for the reduced elastic modulus, E_r, when the plastic indentation depth, h_p, included pile-up height, h_{pu}, were up to 15 GPa lower than those obtained when the pile-up height was not included (an 11 percent difference). A similar effect occurred in the hardness calculations. The average hardness calculated with pile-up was 1.3 GPa, or 20 percent lower than the hardness without pile-up. This effect is shown in Figure 6-1 for reduced elastic modulus and Figure for hardness. This same trend was seen for the slower (10 μN/s) loading rate as well, as can be seen in the line scan from *in-situ* images taken immediately after an indentation test in Figure 6-2. Because the inclusion of pile-up served to lower the elastic modulus for the deeper indents, it was unable to explain the

low experimental elastic modulus values. However, significant errors would have resulted if pile-up was not included in deeper indents on platinum.

Several studies have found that indentation modulus values of thin film materials can be significantly affected by substrate effects [39-41]. The platinum film was on a {100} silicon substrate, which had a reduced elastic modulus of 141 GPa. Therefore, as deeper indentation depths were probed and the substrate effect increased, the measured elastic modulus should have decreased. Gao and Doerner and Nix developed models of the substrate effects on the measured elastic moduli values and extracted a "film-only" modulus [39-41]. However, due to the limited number of depths that were sampled and the number of parameters that need to be fitted, the models could not be reliably used in this study. Instead, care was taken to ensure that the shallowest indentation depths were less than 10 percent of the film thickness. Indentation depths shallower than 10 percent of the film thickness are generally thought to exhibit only film properties and to not exhibit substrate effects [41, 42]. Therefore, the shallowest indentation depths should have approximated film-only properties well. Despite this, the elastic modulus was still low with respect to the expected value.

Regarding possible delamination or microcracking, if the film delaminated from the substrate or if microcracking occurred in the sample, the material stiffness would have decreased, causing low elastic modulus values. However, *in-situ* images of the indentation surface showed no evidence of microcracking. One would also not expect delamination for a variety of reasons. First, the interface had been specifically designed with a titanium adhesion layer to create a strong interfacial bond between the sample and substrate. Since there was a rather large compressive stress in the film (-695 MPa), delamination would have released a large amount of strain energy, causing abnormalities in the loading curve. However, there were no large discontinuities or unusual shapes to the loading curves (Figure 6-5). Also, if the material underwent a delamination, one would expect the *in-situ* image to have shown an unusually large indent or an indent much larger than the Oliver-Pharr predicted contact radius, which was not the case. The indent radii found from the *in-situ* images was never greater than 10 percent above the Oliver-Pharr predicted contact radii, suggesting that there was no delamination at the film-substrate interface. Thus, microcracking and/or delamination were not likely causes for the low measured elastic moduli.

Traditional strain rate sensitivity seen in metals cannot explain the low elastic modulus observed in this study. If there was strain rate sensitivity, one would expect the elastic modulus to have remained invariant with respect to the unloading rate, while the hardness would have increased

since hardness correlates with yield strength (e.g., the Tabor approximation [43] or any other appropriate yield strength-hardness relationship).   However, the hardness was not strongly affected by changes in strain rate, as shown in Figure 6-4, and in some cases exhibited sensitivity that was the opposite of what would be expected in a metallic material. For example, at shallow indentation depths, the hardness for the 100 μN/s unloading rate was approximately 11 percent lower than for the 10 μN/s loading rate. At larger indentation depths, the expected increase in hardness for a strain rate sensitive material at faster loading rates was observed. The weak strain-rate sensitivity of the hardness of the platinum films was a departure from the behavior reported for most nanocrystalline FCC metal films [44-48].

In contrast to the invariance of the hardness, the indentation elastic moduli were a function of the unloading rates. As shown in Figure 6-4, when the unloading rate was decreased by an order of magnitude, the reduced elastic modulus also decreased. A maximum difference of 15 GPa (11 percent) was found between the two unloading rates. However, one would not have expected the elastic parameters to vary significantly with varying unloading rates, since the elastic modulus was a function of the interatomic bond stiffness and not of dislocation mobility, grain boundary sliding, or other plastic deformation processes. Jayaganthan et al. noticed a similar effect in nanocrystalline nickel, and suggested it may be due to creep during the holding time [46]. Since the displacement during the hold time varied with loading rate and maximum force (as seen in Figure 6-6 and the inset of Figure 6-5), the role of creep in the measured indentation modulus was assessed. In order to evaluate this effect, the additional displacement accumulated during the hold time was deducted from the unloading curve of each indent (mean values are shown in Figure 6-6), and was then analyzed using the Oliver-Pharr method. This method assumed that all displacement during the hold period was due to plastic or anelastic deformation. This assumption would overestimate the effect that eliminating the plastic/anelastic deformation would have on the elastic modulus. However, this analytical method had little effect on the reduced moduli (Figure 5- 6-4): The slower loading rate still had a reduced elastic modulus that was 20 GPa lower than the faster loading rate at the maximum indentation depth (a 13 percent difference).   This invariance in the "corrected" reduced elastic moduli of the platinum films suggests that the apparent strain rate sensitivity was not an artifact of the accumulated creep during the hold time.

It has been suggested that strain rate sensitivity in a nanocrystalline FCC film could be explained by the grain boundary affected zone (GBAZ) model [45]. However, the GBAZ model only explains strain rate sensitivity of the plastic deformation processes, and not in elastic moduli values [45]. Additionally, high-resolution TEM revealed that the platinum was crystalline and contamination-

free at the grain boundaries. Thus, the structure of the film did not show the presence of a weak or amorphous grain boundaries that would be necessary for the GBAZ model. Finally, if the deformation mechanism was confined to grain boundaries, one would expect an intergranular failure mode during a tensile overload. Instead, Meirom et al. have shown that plastic deformation and failure in these nanograined platinum films occurs via a dislocation slip mechanism, and final ruptures have transgranular fracture surfaces [49]. While the GBAZ model can explain trends in hardness values over a range of loading rates, which were not noted in this material system, it cannot explain the low elastic modulus value obtained during the indentation testing of platinum.

One possibility for the low elastic moduli values was that the material was either strain-rate sensitive or behaved in a viscoelastic manner, so that time-dependent elastic and plastic deformations are possible. Strain-rate sensitivity is time-dependent plastic deformation, which is described by a correlation of the strain rate with either yield or flow stress. Viscoelastic behavior is time-dependent elastic deformation, in which the elastic constants are a function of loading history and time. During the loading portion of the experiments, the response for the faster loading rate (100 μN/s) was stiffer (Figure 6-5). The discrepancy between the two curves continued in the hold period of the indentation test (Figure 6-5 inset). The faster loading rates showed evidence of transient, rapid, time-dependent deformation during the initial part of the hold period that transitioned to a steady-state rate. In contrast, the initially high deformation-rate and transition were not observed during the hold period of the slower loading rate experiments (10 μN/s) because it had already accumulated during the loading phase of the experiment (i.e., before the onset of the hold period). Additionally, the steady-state deformation rates for the faster loading rate indents were higher than that for the slower loading rates. The average steady-state deformation rates for the shallowest indentation depth were only 4 percent different (0.077 and 0.080 nm/s for the 10 and 100 μN/s loading rates, respectively), but were 42 percent different at the deepest indentation depth (0.160 and 0.246 nm/s for the 10 and 100 μN/s loading rates, respectively). Therefore, more time-dependent deformation was accumulated during the hold period for the faster loading rate indents (Figure 6-6). It is important to note that these steady-state deformation rates, while very small, were larger than the displacement drift rates of the system for a given indent. During the unloading portions of the curves there was a distinct difference in slope between the two loading rates (Figure 6-5). As seen in the loading portion, the faster unloading rates also had a stiffer response that is reflected in the apparent elastic moduli of the material (Figure 6-5). Moreover, the time-dependent deformations were reversible (i.e., were anelastic), as demonstrated by the invariance of penetration depth (Figure 6-2) and hardness

(Figure 6-4) with loading rate, and the ineffectiveness of the "creep corrected" Oliver-Pharr calculation performed above (Figure 6-4).

There are a variety of models based on various arrangements of springs and dashpots that have been used to evaluate the viscoelastic response of materials during instrumented indentation. For example, Ngan et al. employed a model that corrected the stiffness using a Maxwell system viscoelastic response [50]. Similarly, Fischer-Cripps devised a solution where lumped parameters for two, three, and four element viscoelastic systems (denoted as Maxwell, Voigt, and Maxwell-Voigt by Fischer-Cripps, elsewhere as Maxwell, Standard Linear Solid, and Burgers systems) were derived for both conospherical and Berkovich indenter tips [51]. Ogbonna et al. created a model to determine the strain hardening exponent and the strain rate sensitivity [52]. Given the viscoelastic response of the platinum films, we attempted to apply these established models. The shape of the force versus displacement curves in this work suggested that the Maxwell model applied by Ngan et al. would not be able to describe the behavior occurring in the platinum film. The Ngan et al. model allowed them to account for deformation that occurred during the hold period, but it did not capture the general viscoelastic response of the material and could not have predicted the response of the material system as a function of strain rate [50]. As a result, when we used the Ngan et al. model to evaluate the response of the platinum films, the already low reduced elastic moduli found for the shallowest penetration depths in the Oliver-Pharr analysis (after correction for pile-up and machine compliance) decreased further and the loading rate effect was preserved (the original analysis was 20 percent larger than the Ngan solution which predicted 180 and 135 GPa for 100 and 10 μN/s loading rates). Moreover, the depth dependence of the elastic modulus was amplified, with reduced elastic moduli values that decreased to approximately 50 GPa, which was far below the elastic modulus of the (100) silicon substrate. Similarly, the Fischer-Cripps models also failed to describe the viscoelastic response of the platinum films. The Fischer-Cripps models provided unrealistic values for the spring constants in the models that were orders of magnitude larger than that of diamond. Finally, too few loading rates were sampled in our work to effectively use the model developed by Ogbonna.

Since none of these models could capture the viscoelastic behavior of the platinum films, we postulated that the material response should be that of the four element, spring-dashpot Maxwell-Voigt (as denoted by Fischer-Cripps) system shown in Figure 6-7. It was assumed that in this case, spring k_1 was much greater than k_3, and that dashpot η_2 was much greater than η_3. These assumptions lead to an equation of the general form

$$h_c = v \cdot t + \frac{P_0}{k_3}\left[1 - \exp\left(-\frac{k_3}{\eta_3}t\right)\right].$$

6-1

where k_3 and η_3 were the respective parallel spring and dashpot in the Maxwell-Voigt system, as shown in Figure 6-7, v was the tip velocity, and h_c was the displacement due to creep. Since this model did not account for the loading history, differences in both k_3 and η_3 between the fast and slow loading rates were expected. While this general model did not allow for the calculation of either the elastic modulus value or the viscosity constants, it allowed insight into general features of the viscoelastic material response. The values found for the spring constant k_3 are shown in Figure 6-8 and those found for the viscosity constant η_3 are shown in Figure 6-9. The second spring was quite stiff, requiring hundreds to thousands of micronewtons to have moved one nanometer, and the dashpot was not very viscous. Additionally, the k_3 spring was stiffer during unloading for the slower loading rate because there was less displacement during hold period since the rapid portion of the time-dependent displacement had been exhausted. In contrast, the faster loading rate hold time still showed evidence of this initial transient, and a more pronounced viscoelastic response. Thus, the values found for the spring and dashpot were consistent with a slight viscous response in the material, and that a complex elastic modulus associated with anelastic behavior could explain the generally low elastic moduli values.

Recently, a fatigue test conducted by Meirom et al. showed evidence of grain coarsening under stress [53]. The fatigue test was stopped before film failure so that both sides of the crack front could be examined. Grains immediately surrounding and ahead of the crack front had grown to approximately significantly (5-10 times their original size). Elsewhere in the film, the grain size was as reported before testing (20-50 nm). Additionally, the grains immediately around and in front of the crack tip appeared to have reoriented [53]. This is in agreement with indentation and compression tests performed on highly pure, nanocrystalline films [54-57]. Zhang et al. found that 10 s of indentation dwell time on nanocrystalline nickel was enough to induce grain growth [56]. Longer dwell times caused more grain growth, with grains increasing from approximately 20 to 250 nm at 30 minutes. Additionally, when the tests were repeated at cryogenic temperatures, they found the grain growth occurred more quickly. This increased grain growth at lower temperatures eliminated thermal diffusion as the mechanism [56]. Instead, it appears that grain growth can occur under tensile or compressive stress fields when the original grain size is less than 100 nm. Since TEM images of the grain structure around the indents had not been performed for this sample, it is unclear if grain growth is a possible mechanism causing the time dependent behavior of the platinum film. However, it is possible to assume it occurred, since it

was noted in very fine grained, pure aluminum, copper, and nickel [54-56, 58]. If grain growth did occur and the microstructure under the indenter tip was evolving during the test, both the modulus and hardness could have been significantly affected.

Despite the mechanism, the platinum film showed time dependent behavior in the reduced modulus only. The hardness was found to be invariant with indentation loading rate. This behavior suggests that an anelastic response is occurring underneath the indenter tip. This anelastic behavior could explain the low moduli values reported in the previous four studies by Mencik and Swain, Lee et al. and Hyun et al. and in this study.
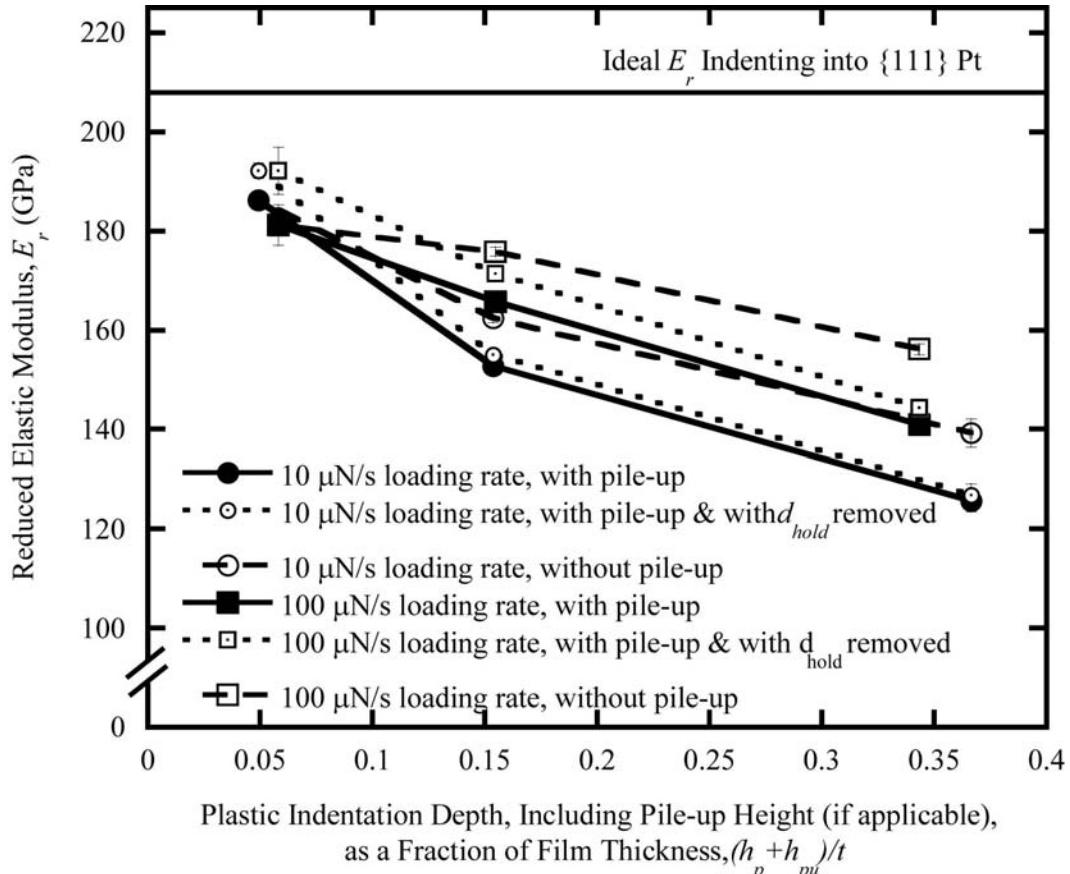
Figure 6-1 Reduced elastic modulus of platinum film as a function of indentation depth normalized by film thickness. The 10 μN/s loading rate is shown above in circles and the 100 μN/s loading rate is shown as squares. The values with pile-up are shown as closed symbols with solid connecting lines and the values without pile-up are shown as open symbols with dashed lines. The open dotted symbols with dotted connecting lines represent the Oliver-Pharr analysis with the hold time displacement removed (and pile-up height included). The error bars correspond to one standard error for a series of 10 indents at the same condition.
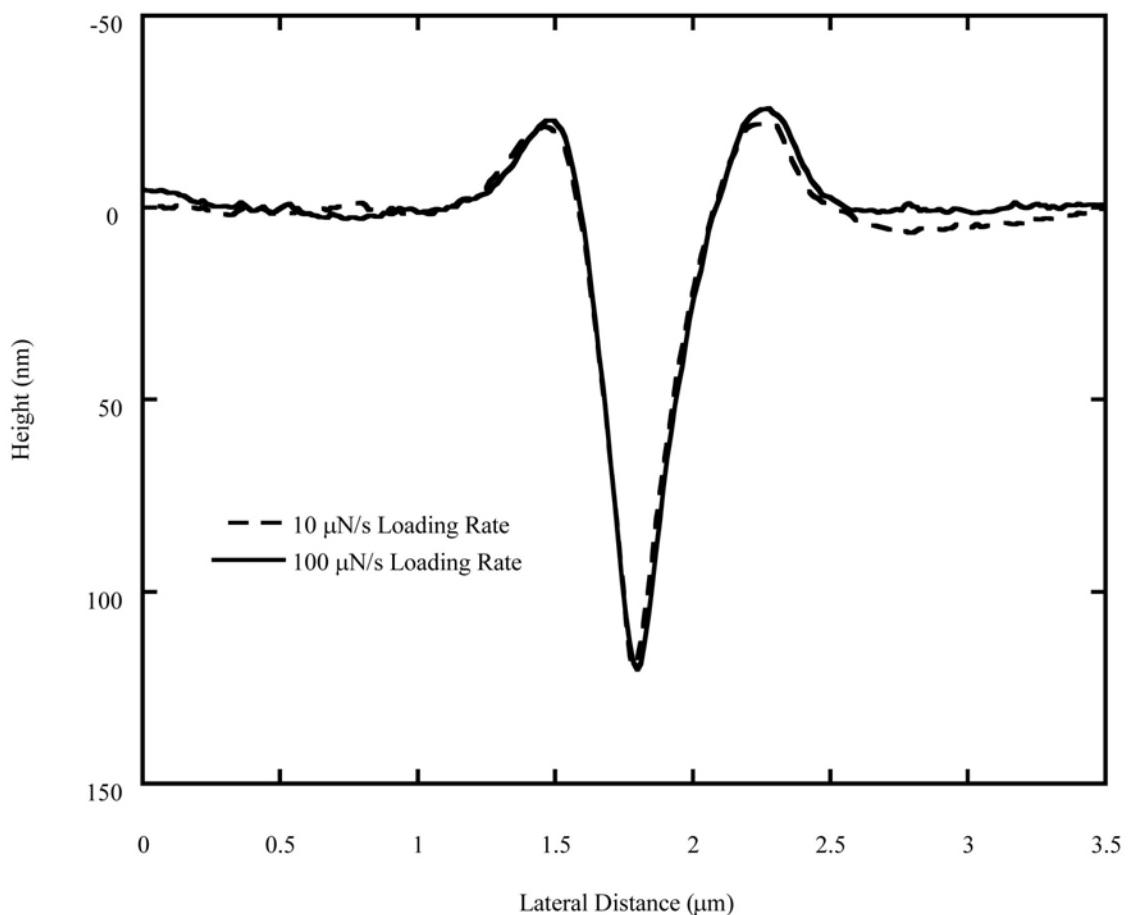
Figure 6-2 Representative line scan through maximum depth of a 3100 µN indent for both 10 µN/s (dashed line) and 100 µN/s (solid line). Positive depth values indicate depths into the platinum film, while negative values indicate heights above the mean surface of the film, to correspond with the displacement convention with instrumented indentation data.
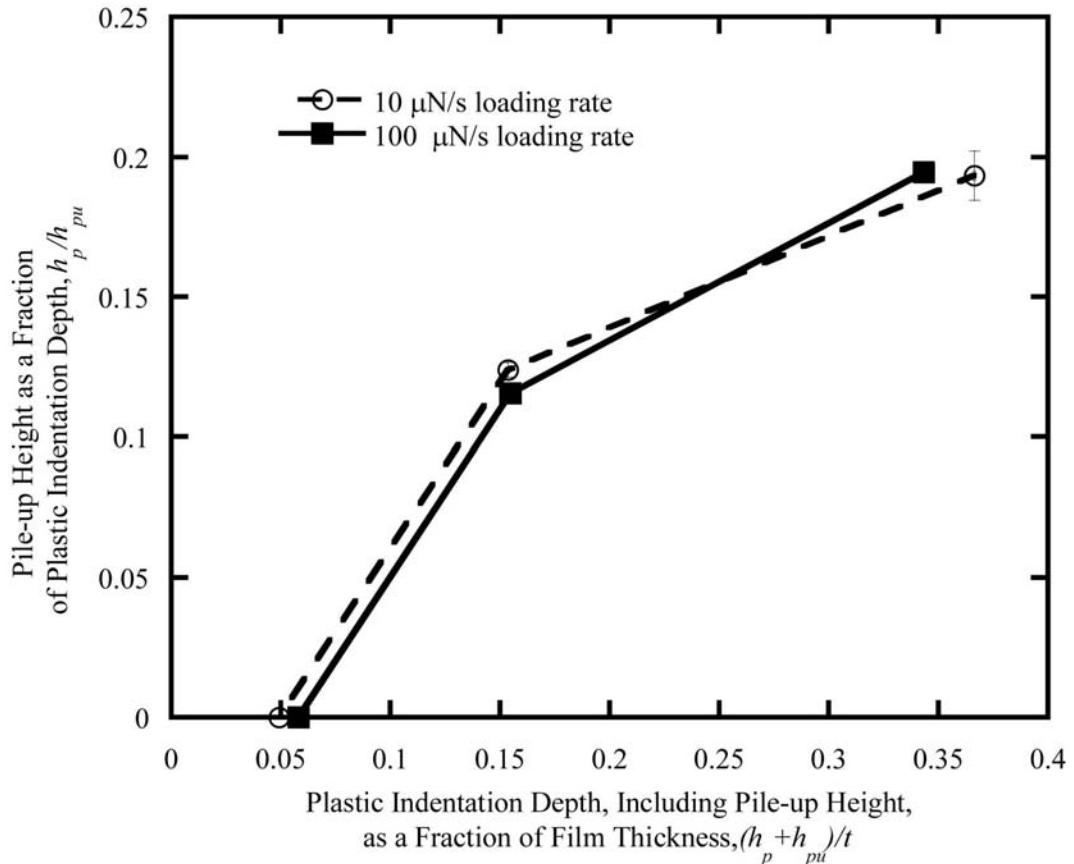
Figure 6-3 Percent pile-up as a function of plastic indentation depth. The 10 μN/s loading rate is shown as an open circle with a dashed connecting line, while the 100 μN/s loading rate is shown as a closed square with a solid connecting line. The error bars shown correspond to one standard deviation for a series of 10 indents at the same condition.
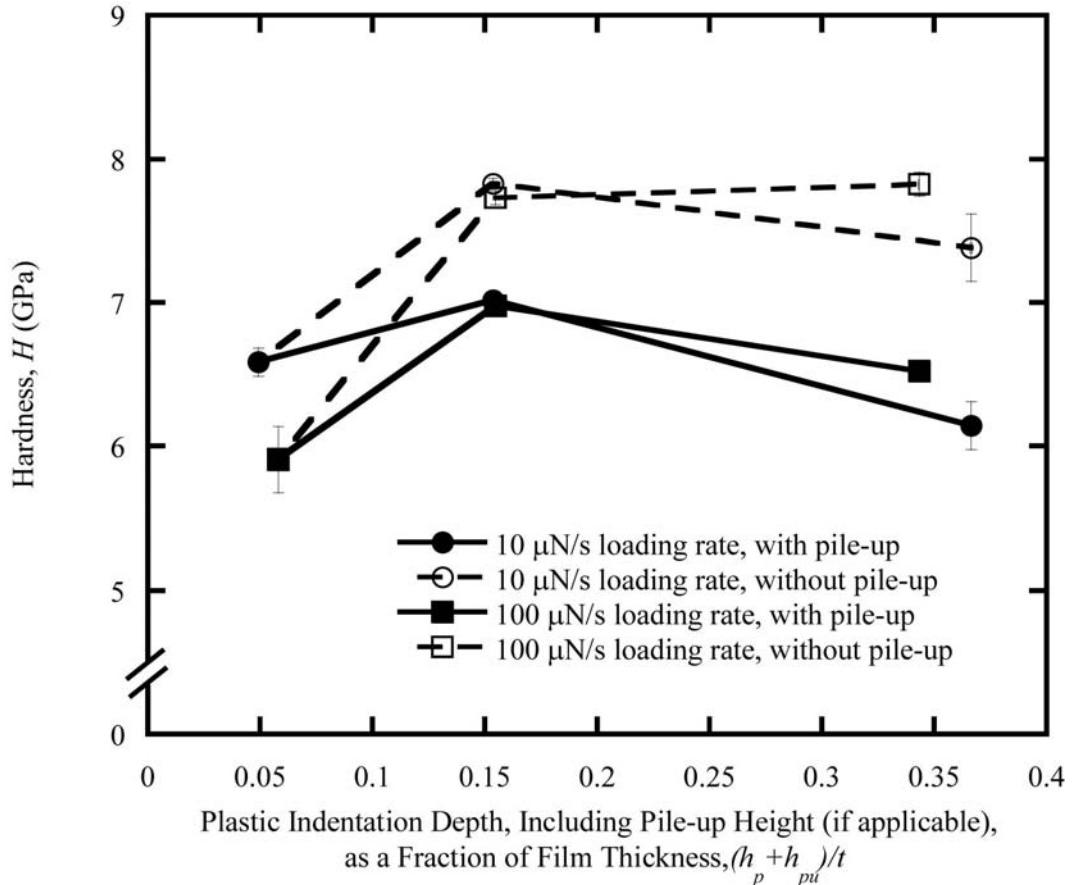
Figure 6-4 Hardness elastic modulus of platinum film as a function of indentation depth normalized by film thickness. The 10 μN/s loading rate is shown as circles and the 100 μN/s loading rate is shown as squares. The values with pile-up are shown as closed circles with solid connecting line and the values without pile-up are shown as open circles with dashed lines. The error bars correspond to one standard deviation for a series of 10 indents at the same condition. Note that the lines on the graph are shown to help highlight differences between the two different data sets and are not meant as a trendline.

.
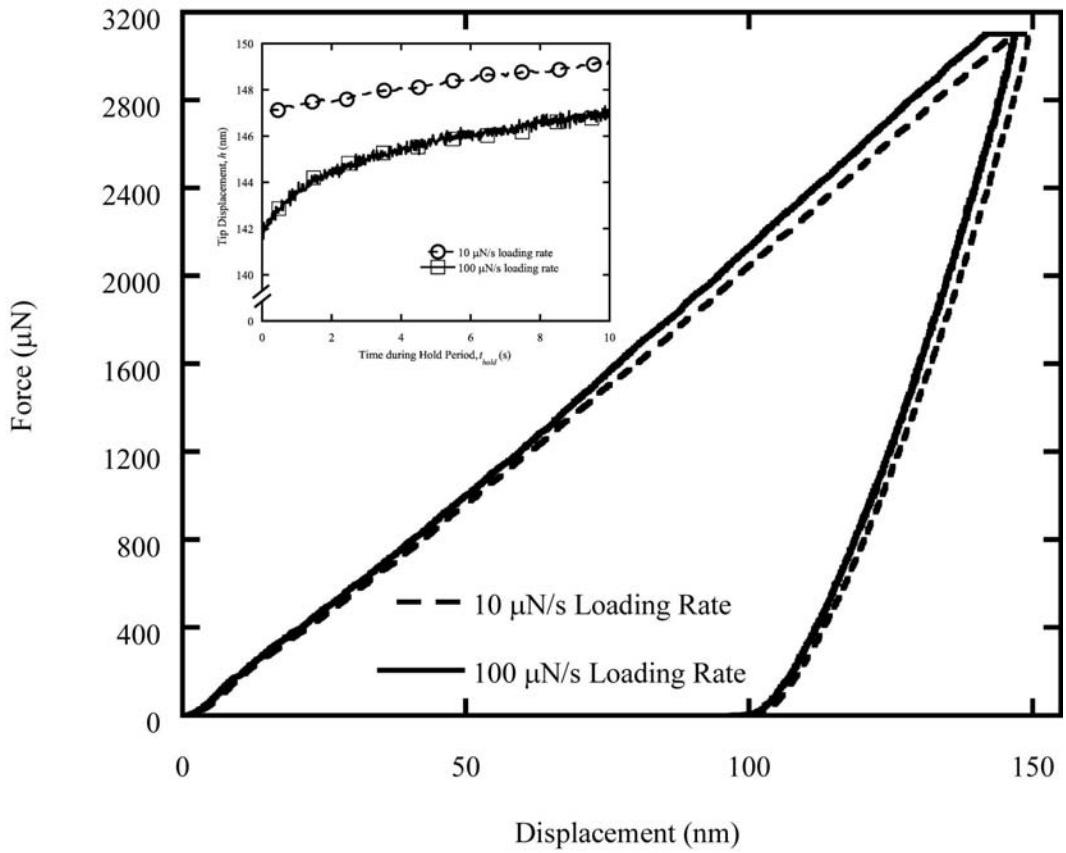
Figure 6-5 A representative force versus displacement curves for indents with a maximum load of 3100 μN. The inset shows displacement versus time for the hold period of both loading rates. The 10 μN/s loading rate is shown as a dashed connecting line (with circles in the inset), while the 100 μN/s loading rate is shown as solid connecting line (with squares in the inset).

.
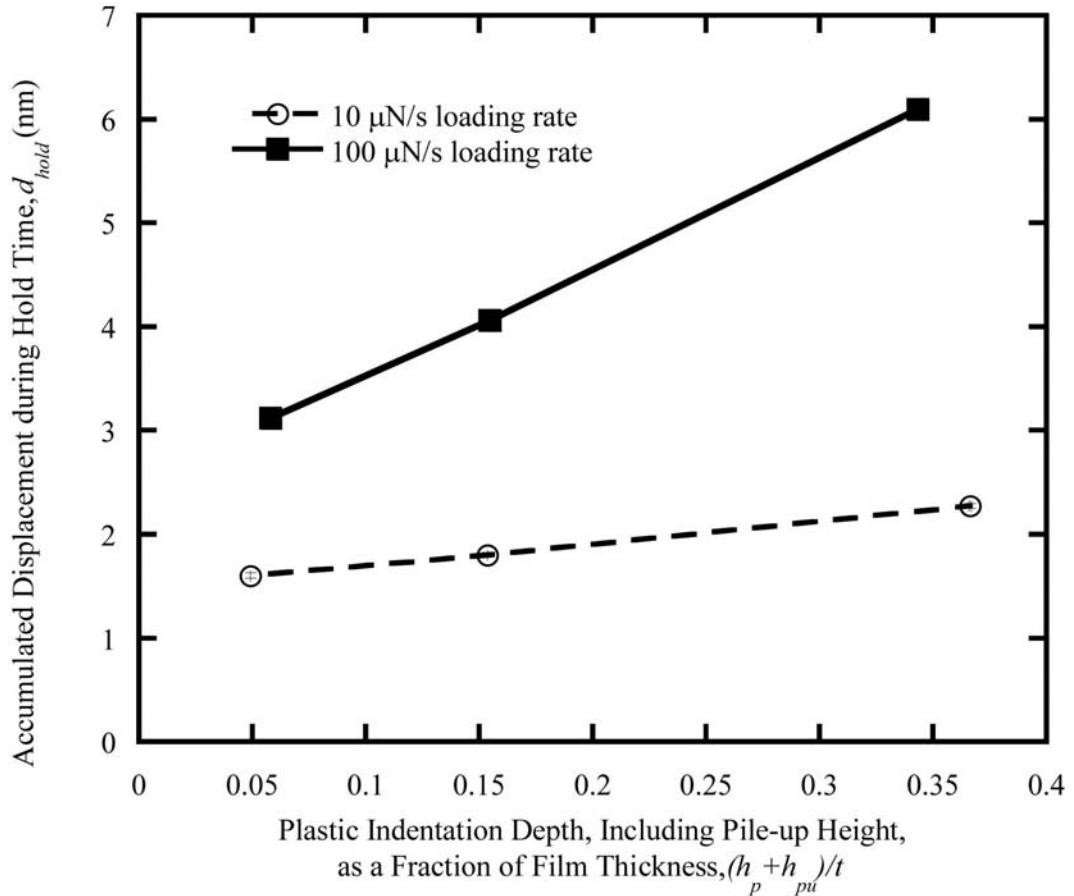
Figure 6-6 Accumulated displacement during the hold period of indentation tests as a function of indentation depth normalized by film thickness. The 10 μN/s loading rate is shown as open circles with dashed connecting lines, and the 100 μN/s loading rate is shown as closed squares with solid connecting lines.

.
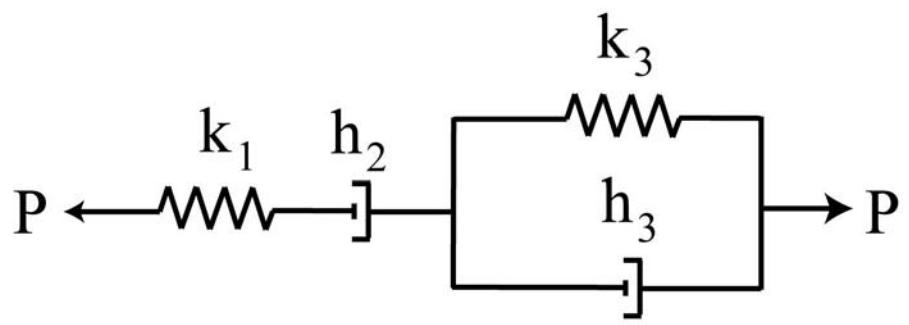
Figure 6-7 Maxwell-Voigt (4 element) spring/dashpot system model.
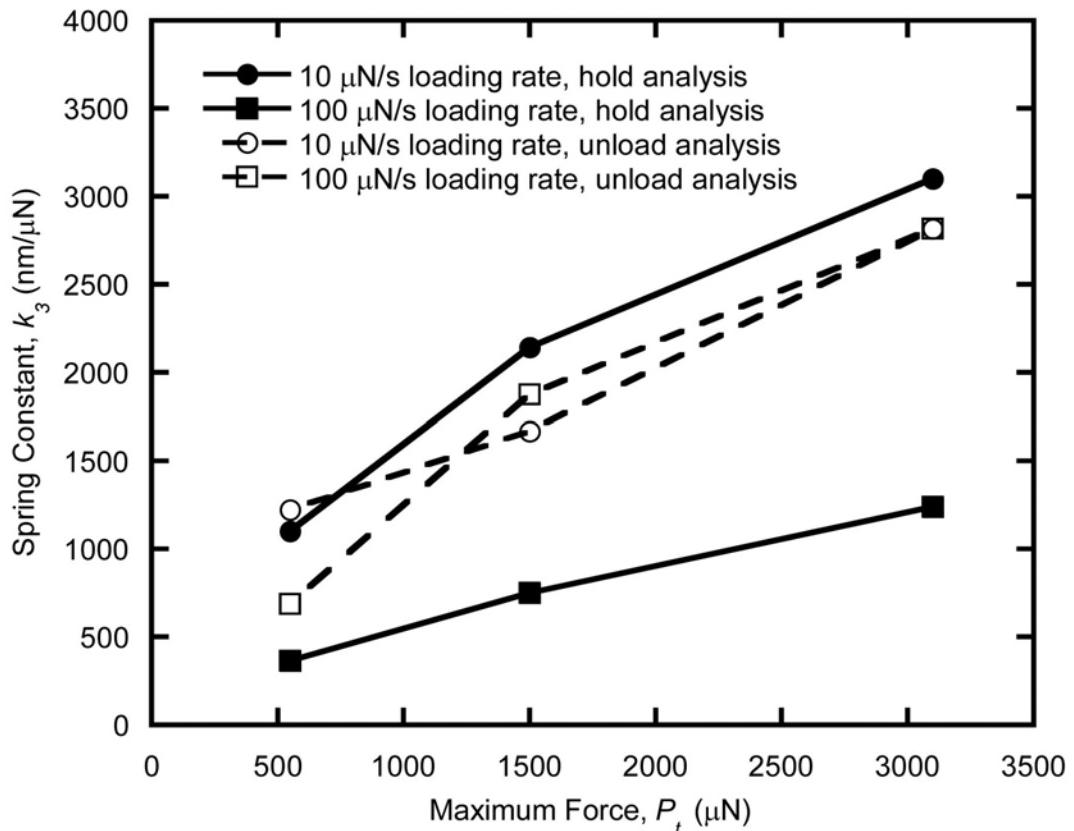
Figure 6-8 Spring constant k_3 versus maximum indentation load for emperical viscoelastic solution. The 10 μN/s loading rate is shown as circles and the 100 μN/s loading rate is shown as squares. The solutions for the holding period are shown as closed circles with solid connecting lines and the solutions for the unloading period are shown as open circles with dashed lines.
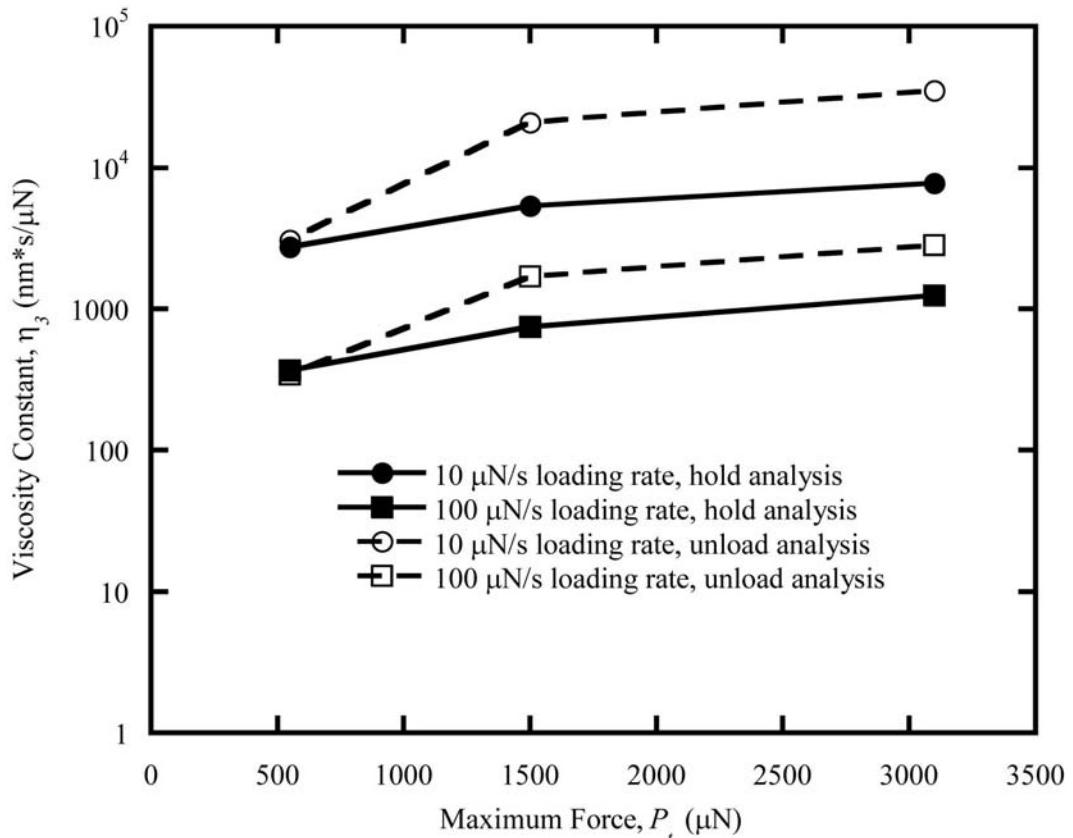
Figure 6-9 Viscosity constant η_3 versus maximum indentation load for emperical viscoelastic solution. The 10 μN/s loading rate is shown as circles and the 100 μN/s loading rate is shown as squares. The solutions for the holding period are shown as closed circles with solid connecting lines and the solutions for the unloading period are shown as open circles with dashed lines.

6.1.2   Region "B" findings

To confirm whether the time dependent behavior was strain rate sensitivity or anelasticity, additional loading rates were explored to more fully characterize the response of the material. Symmetric tests with loading/unloading rates of 25, 50, and 75 µN/s were evaluated in region "B" as shown in Figure 5-1. These additional loading rate tests would also allow for the application of the Ogbonna solution, which requires several loading rates to apply.

However, when the elastic moduli and hardness values from the additional loading rate tests were evaluated, it was found that the data was not consistent with trends seen in the tests performed in region "A." In region "A," there was no discernible trend in the hardness data with respect to indentation depth (Figure 6-4). In region "B," there was again no discernible trend in the hardness with respect to indentation depth (Figure 6-10). For the shallowest indentation depths, the hardness increases with increasing loading/unloading rate. However, at 1500 µN, there is no trend in the hardness, with the 50 µN/s loading/unloading rate showing the lowest hardness value. Finally, at the deepest indents, the hardness values did not vary significantly with changes in loading rate. The average hardness in region "A" is also very similar to that in region "B." (Figure 6-3) The hardness over all loading rates and depths is 6.47±0.01 GPa for region "A" and is 6.20±0.01 GPa for region "B."

Unlike the hardness results which correlated well between regions "A" and "B," the reduced elastic modulus showed distinct differences between the two regions (Figure 6-11). The slower loading rate (10 µN/s) had the higher reduced modulus value in region "A." In region "B," the slower loading rates had the lower reduced moduli values, inverting the trend seen in region "A." Additionally, region "B" had larger reduced moduli than region "A." The highest elastic modulus found in region "B" actually exceeded that expected for <111> oriented bulk platinum [30-32], with the highest reduced modulus of 221±6 GPa (five percent above the <111> bulk platinum value of 211 GPa). In region "A," the reduced modulus was 10 percent below the <111> bulk platinum value.

The region "B" trends were more consistent with what would be expected from a material displaying a viscoelastic response. A quicker loading/unloading rate should decrease the time-dependent deformation. This will increase the apparent stiffness of the material, and increase the reduced modulus found from the Oliver-Pharr analysis, which was seen with the region "B" tests performed at 25, 50, and 75 µN/s loading rates (Figure 6-11Figure 6-2). Because the trends were those that were expected from a viscoelastic material, the region "B" tests were fitted to the Ogbonna solution to determine if the response in region "B" was due to strain rate sensitivity.

However, the Ogbonna solution produced negative strain hardening and strain rate sensitivity exponents. While a negative strain hardening exponent can be found, there have been no reports of a metal with a negative strain rate sensitivity. Therefore, it is unlikely that the response exhibited by the 25, 50, and 100 μN/s loading/unloading rate tests was due to strain rate sensitivity.

Because the results seen in the region "B" tests showed different trends from those in region "A," the 10 and 100 μN/s loading/unloading rate tests performed in region "A" were repeated in region "B." All controllable testing conditions were the same from region "A" to region "B," but the 10 and 100 μN/s tests performed in region "B" were found to be significantly different than those performed in region "A." (Figure 6-13Figure 6-4) The smallest difference between identical tests was 20 percent, while the largest was 48 percent. These differences between identical tests seemed to suggest spatial variation within the material. This spatial variation could be due to processing controls, differences in residual stresses from region to region, or the process used to etch the platinum or silicon to create the tensile bars on the sample. Although the film was found to be <111> columnar nanograined through most of the thickness through TEM studies, the surface was found to have grain sizes of less than 10 nm that did not correlate with those found in the TEM studies. The different morphology of the surface layer could vary from region to region, causing the spatial variations seen in the indentation test results. However, one would expect that the differences would be the largest for the shallowest indents where the surface layer comprises a larger percentage of the indentation depth. However, the differences are the greatest for the deepest indentation depths that are approximately 35 percent through the film thickness, which should be fully into the <111> columnar nanograined portion of the film. Residual stresses have been found to change the shape of the force-displacement (*P-h*) curve and to change the maximum depth for a force controlled indent [59]. Thus, changes in residual stress could cause anomalies in the reduced modulus, since the shape change in the *P-h* curve could cause changes in stiffness measurements. Additionally, the process used to etch the platinum or silicon could have also caused local variations within the film, but these should mostly be surface effects again. The etching processes could have created small pockets where the platinum film was no longer continuously attached to the silicon substrate. These areas would be expected closer to the edge of the film or near the etch regions for the tensile bars. An area that was locally delaminated from the substrate before indentation would not have the same pop-in events that would occur if the film delaminated from the substrate during the test. The additional displacement that would have occurred due to the strain energy release during delamination would not have occurred if the film was already delaminated prior to the indentation test. Instead, the film would appear less stiff

than would be expected. There would also not be large delaminations apparent in the pre and post *in-situ* images. All of this is consistent with what was seen in both region "A" and "B" testing. Those tests that were closest to the edge of the film had the lowest stiffness values. Additionally, no distinct signs of delamination were seen in the in-situ images. However, care was taken to indent in areas that did not appear to be free from the silicon substrate. The platinum film showed distinctive ridging due to the large residual compressive stresses in the regions where the film was free from substrate. All indentation tests were at least two times the length of these ridges away from the platinum film edges to ensure that the film was properly adhered to the substrate. Further, there was no evidence of ridging in the areas where indentation tests were performed, which would be expected if large areas were substrate free.

However, spatial variation does little to explain the differences between indentation tests that were less than 300 μm away from each other. The trends seen in the 10 and 100 μN/s tests performed in region "B" did not show similar trends to those seen in the 25, 50, and 75 μN/s tests in region "B," which were less than 300 μm apart from each other. While the 100 μN/s tests had reduced moduli larger than the respective 25, 50, and 75 μN/s tests, the 10 μN/s test moduli were also larger. This meant that the viscoelastic response was stiffer at the lowest loading/unloading rate, then the stiffness decreased significantly for the next faster rate, and then steadily increased to the original stiffness found with the slowest rate. Spatial variations may explain this effect, but the fact that the material properties can vary so significantly in such a short distance is disconcerting and requires further study of other possible effects. Besides the indents being performed in a different area, the indents were also performed at different times. The tests in region "A" were started on August 16, 2007. The 25, 50, and 75 μN/s tests in region "B" were performed on July 22, 2008 and the 10 and 100 μN/s tests in region "B" were performed on August 8, 2008. The 25, 50 and 75 μN/s tests were performed in a separate run than the 10 and 100 μN/s tests, and drift measurement tests described in Section 5.3.3 were performed in between the two test sets. Environmental factors such as humidity and temperature were not monitored during the course of the tests and could have changed. These environmental factors could have caused differences in stiction and friction between the indenter tip and the platinum surface. It also could have caused elevated creep levels or changes in the equipment performance.
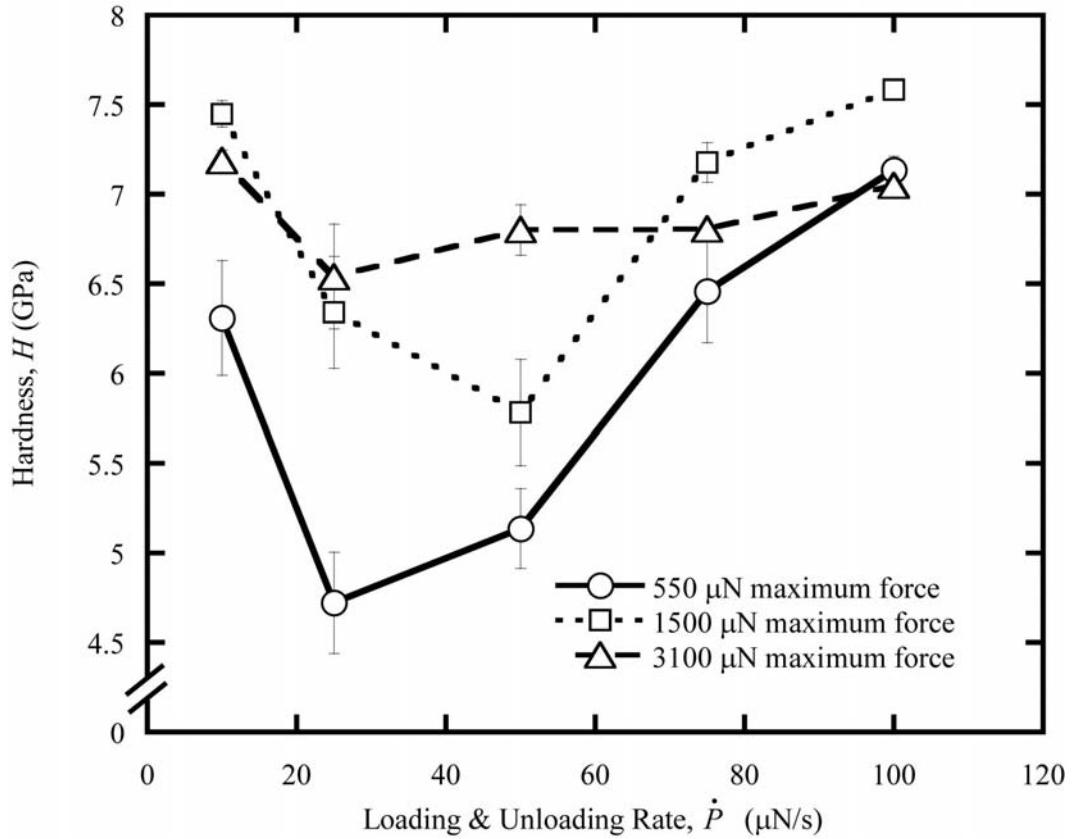
Figure 6-1 Hardness versus loading rate for tests performed in region "B." Tests with a maximum force of 550 μN are shown with solid lines and open circles. Those with a maximum force of 1500 μN are shown with dotted lines and open squares, and maximum forces of 3100 are shown with dashed lines and open triangles.
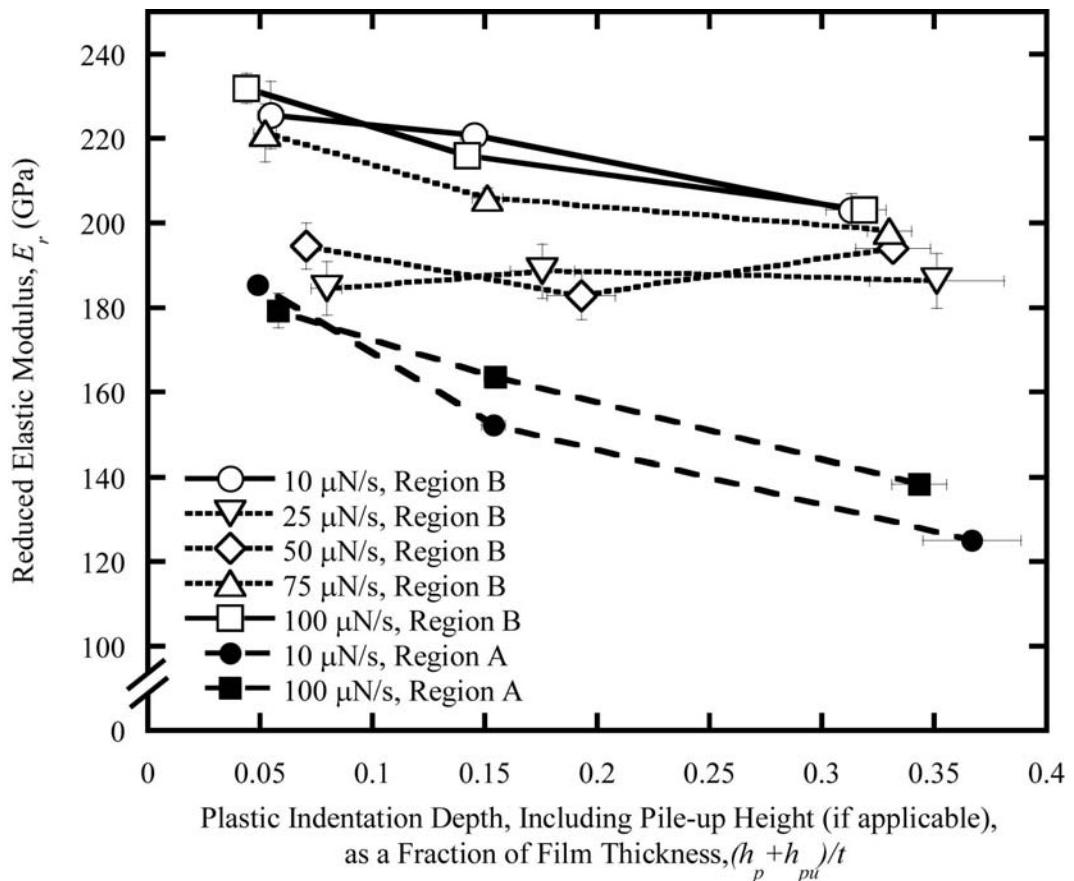
Figure 6-2 Reduced elastic modulus versus percent indentation depth for symmetric loading rate tests. Tests performed in region "A" are shown with solid symbols and dashed lines; the 10 μN/s tests are shown with solid circles and the 100 μN/s tests are shown with solid squares. The 10 and 100 μN/s in region "A" were performed at the same time. The 25, 50, and 75 μN/s tests are shown with dotted lines and and open downward triangles, diamonds, and upward triangles, respectively. The 25, 50, and 75 were all performed at the same time. Finally, the 10 and 100 μN/s tests in region "B" were shown with solid lines and open circles and squares, respectively. Again, the 10 and 100 μN/s tests in region "B" were performed at the same time. All tests with the same interconnecting lines were performed at the same time.

Figure 6-3 Hardness versus percent indentation depth for symmetric loading rate tests. Tests performed in region "A" are shown with solid symbols and dashed lines; the 10 μN/s tests are shown with solid circles and the 100 μN/s tests are shown with solid squares. The 10 and 100 μN/s in region "A" were performed at the same time. The 25, 50, and 75 μN/s tests are shown with dotted lines and and open downward triangles, diamonds, and upward triangles, respectively. The 25, 50, and 75 were all performed at the same time. Finally, the 10 and 100 μN/s tests in region "B" were shown with solid lines and open circles and squares, respectively. Again, the 10 and 100 μN/s tests in region "B" were performed at the same time. All tests with the same interconnecting lines were performed at the same time.

Figure 6-4 Reduced elastic modulus versus loading rate for tests performed in region "B." Tests with a maximum force of 550 μN are shown with solid lines and open circles. Those with a maximum force of 1500 μN are shown with dotted lines and open squares, and maximum forces of 3100 are shown with dashed lines and open triangles.

6.2   Asymmetric Test Results

In addition to the symmetric tests performed, asymmetric tests were also completed in region "B." One test at 10 μN/s loading rate, 100 μN/s unloading rate, 1500 μN maximum force was eliminated from data analysis because the surface was not sensed properly by the indenter. Over 200 nm of displacement was obtained before the load even reached 10 μN. Additionally, the residual indentation depth , h_r, was 270 nm, while *in-situ* post indentation images show the depth to be approximately 35 nm.

Due to the issues about possible spatial and environmental variations causing significant differences in the indentation results, it is difficult to say what, if any, impact the loading and unloading rate had upon the results from the Oliver-Pharr analysis. Although the asymmetric tests were performed within 100 μm of the region "B" 10 and 100 μN/s symmetric tests, they were performed almost 2 weeks apart, with drift measurement tests described above performed in between the two sets of tests. Still, it was interesting to note that the two asymmetric tests had results very similar to each other and to the symmetric 10 and 100 μN/s tests performed in region "B." (Figure 6-14) This suggested that the viscoelastic response of the material may be smaller than originally suspected. Instead, the supposed "viscoelastic" response may be due to spatial and environmental variations between tests. However, the real effect that loading and unloading rate may have on the Oliver-Pharr solution for this material cannot be deconvoluted from the spatial and environmental effects and can only be guessed at by tests performed as close as possible to each other both in time and in location.
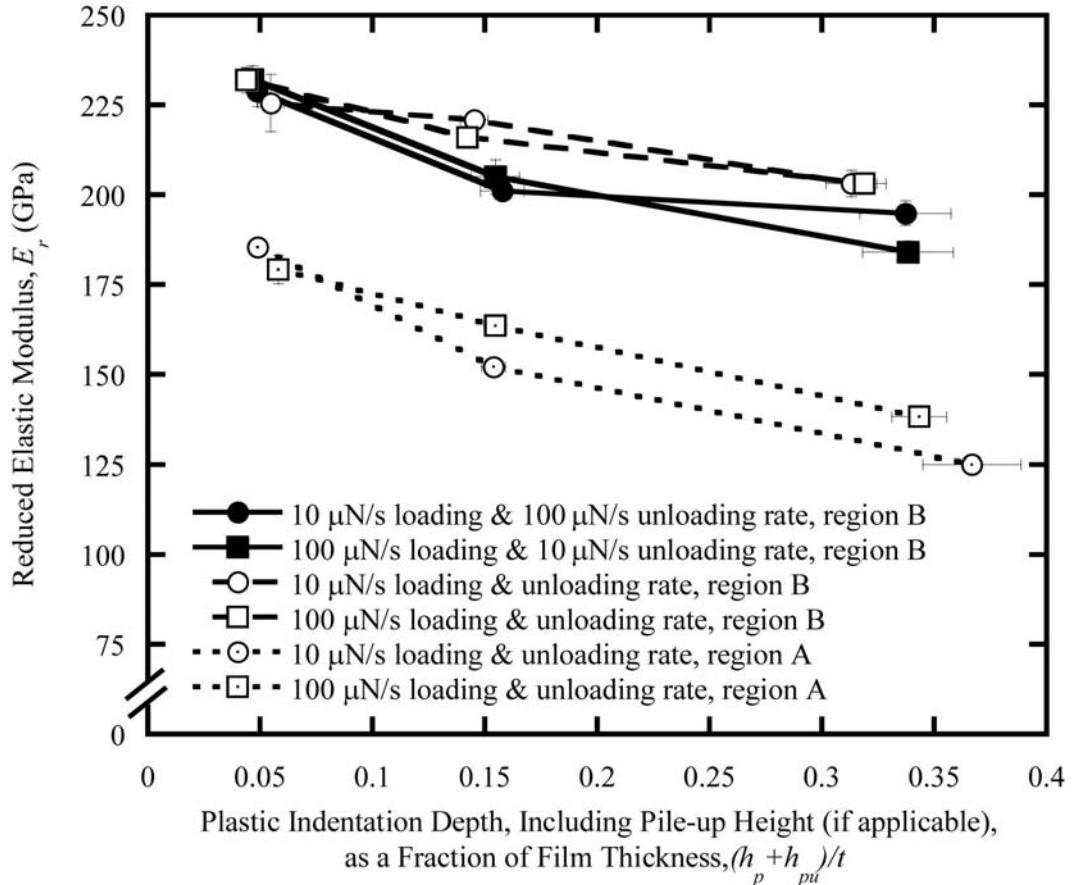
Figure 6-5 Reduced elastic modulus versus percent indentation depth for symmetric loading rate tests. Tests performed in region "A" are shown with open symbols with a dot inside and dotted lines; the 10 μN/s tests are shown with circles and the 100 μN/s tests are shown with squares. The 10 and 100 μN/s tests in region "B" were shown with dashed lines and open circles and squares, respectively. The asymmetric tests were shown with solid symbols and lines. The solid circles show tests performed with a 10 μN/s loading rate and a 100 μN/s

Ĥ   9

s at 100 μN/s loading rate and 10 μN/s unloading rate.

6.3 Drift measurement

Figure 6-15 shows the representative force-displacement behavior of the {111} platinum thin films. Section 5.1 established that at shallow penetration depths (~7% of the film thickness) the Young's modulus of the film as 153 GPa, and the hardness was 5.9 GPa. The study also found that the films showed rate dependence for the elastic modulus but not for the hardness, suggesting the material response was anelastic. This anelasticity caused the apparent elastic modulus to decrease with increasing loading rate and with maximum indentation force [60]. Representative data from the higher loading rate tests (Figure 6-15) illustrated the weak, but measurable viscoelastic response of the nanograined metal that was consistent with results from other researchers [51]. The viscoelastic response made the loading and unloading curves appear more compliant for slower loading rates, a trend that was expected to continue for slower loading rates. For most of the 1 μN/s tests this trend continued, as demonstrated in Figure 6-6 for the 0.014508 nm/s Hysitron calculated displacement drift rate data. However, several tests showed an inverse trend, with the loading curve being initially stiffer than the faster loading rates (10 and 100 μN/s). Additionally, the unloading curve showed characteristics of a highly viscoelastic material as evidenced by the bulging, or "nosing", outward of the unloading curve.

The shape of the unloading curve prevented traditional power law relationships from being fit to the data. Since the Oliver-Pharr method calculated the stiffness of the material by taking the displacement derivative of the power law fit to the unloading curve and evaluating at the maximum indentation depth, the stiffness had to be determined using an alternate technique. Where the unloading curve could not be fit reliably to a traditional power law relationship, the stiffness was calculated by manually calculating the slope for the top 80-95 percent of the unloading curve. This had to be done for 6 total curves (5 at 1500 μN maximum force, 1 at 3100 μN maximum force). Because the abnormalities in the loading and unloading curve were both intermittent (in only 6 of 30 total indents) and the in-situ surface scans did not indicate abnormal surface conditions, it was hypothesized that the peculiar force-displacement curves were a byproduct of experimental artifact.

Experimental artifacts such as pile-up, substrate effects, anisotropy, and delamination and/or microcracking can lead to errors in the interpretation of force-displacement curves measured during nanoindentation [38-41, 61-63]. As detailed in [60], pile-up was empirically evaluated and corrected using the in-situ scan images. Similarly, substrate and anisotropy effects were too weak to account for the low reduced moduli and limited strain rate sensitivity of the platinum films. However, delamination of the film from the silicon substrate could, in principle, lead to

abnormalities seen in the force-displacement data. In such a case, one would expect that delamination to cause discontinuities in both the loading and unloading portions of the experiment. Since no discontinuities were observed in any of the indentation curves (Figure 6-15), delamination was an unlikely cause of the anomalous *P-h* data.

Two possible experimental artifacts, non-constant drift rates and large accumulated drift, could have given rise to the erratic behavior observed at slow loading rates Figure 6-15). In order to determine how constant the drift rate was over a long test time, long-term displacement drift measurements were performed (Figures 6-16 to -18). It is interesting to note that the displacement rate was not constant, and did not reach a steady-state until approximately 500 s (approximately 8 minutes) after the test began. Additionally, a linear curve fit of the steady state region (for the raw, uncorrected data) established that the displacement drift rate was 0.0287 nm/s. In contrast, the displacement drift rate calculated immediately prior to the long hold period was 0.0217 nm/s. This ~32% change in displacement drift rate only causes an uncertainty in the displacement measurement of ±0.4 nm for a 60 s experiment (hence the accuracy of many previously published results is assured). However, the uncertainty in the location of the indenter tip is much greater in the slow loading rate tests (±13 nm for a 30 min test). When this experiment was repeated an additional four times, it was found that the neither the steady state drift rate or the change between the initial measured drift rate and the final steady state drift rate were constant across tests, as shown in Table 6-1.

Because the preload, drift monitor time, drift analysis time, and maximum force can alter how accurate a drift measurement is, additional drift measurement tests were done by varying the above conditions (Figures 6-17 and 6-18). However, it was found that these conditions did not decrease the change in drift rate between the Hysitron measured value before the start of the test and the steady state drift rate (Table 6-1). Tests that were performed with a 1 or 2 μN maximum force that mimiced the Hysitron drift rate measurement (except for a longer time). For the first 500 s of the indentation test, the displacement was approximately zero (Figure 6-18). After the first 500 s, the drift rate changed substantially, and there was 30-40 nm of tip displacement above the drift rate. Therefore, it was clear that drift rates were not constant over the length of a test. This variation would be expected to cause large errors, especially as the test time increases.

It is interesting to note that most of the tests did not display large abnormalities in the force versus displacement curves (i.e., negative slopes and lower moduli). One would expect the longest test times to have had the most anomalous force versus displacement curves. Instead, the abnormal curves were associated with the highest displacement drift rates measured immediately prior to

indentation, and occurred most frequently in the intermediate maximum load condition (1500 μN). This suggested that the phenomena was more complicated than just non-constant drift rates, and was instead also tied to the amount of accumulated displacement drift in the system. The tip displacement into the specimen was described by the raw displacement minus the drift displacement. This means that for tests where the drift rate was high and the testing time was long, the accumulated drift was large. The accumulated drift at the start of unloading was given

$$h_{drift} = \dot{h}_{drift} \cdot t_{unloading,\ start}$$

6-2

where h_{drift} is the accumulated drift displacement and t_{total} is the total test time. When the total accumulated displacement drift was larger than 200 percent of the maximum corrected penetration depth, gross abnormalities were seen in the force versus displacement curves, which produced either extremely small or negative (i.e., non-physical) stiffness values, and therefore small or negative contact moduli (Figure 6-6). The case was worse for the contact modulus, which is a function of stiffness and contact area, both of which are calculated from displacement values. The stiffness, S, can be described as the unloading rate, $\dot{P}$, over the displacement rate of the tip with respect to the sample surface, $\dot{h}_{tip-sample}$. The displacement rate is a function of the total tip displacement, $\dot{h}_{total}$ minus the tip displacement due to drift, $\dot{h}_{drift}$, causing stiffness to be a function of both, as described in the equation below.

$$S = \frac{dP}{dh} = \frac{\dot{P}}{\dot{h}_{tip-sample}} = \frac{\dot{P}}{\dot{h}_{total} - \dot{h}_{drift}}$$

6-3

Although the relationship between stiffness and accumulated drift is more empirical, it is not as easy to identify an anomalous stiffness value. However, since the contact modulus of the material can be determined via other methods, it provided a better criterion for examining anomalous data. Additionally, the error in the elastic modulus was compounded by the error inherent in both the stiffness and contact depth from large amounts of drift. In order to accurately calculate contact depth, the actual tip location at any given time must be well known. Large amounts of drift and a varying drift rates prevent the actual tip displacement into the sample surface from being known. As shown in Table 6-2, there is a strong correlation (-0.495) between the contact modulus and the accumulated drift at the start of unloading, with less than a 0.1 percent chance that the data was uncorrelated. The correlation between the contact modulus and drift rate is weaker (-0.381). The correlation of the stiffness with both the drift rate and the

accumulated drift is lower still (-0.207 and -0.241, respectively). Similarly, the correlation of the contact depth with both the drift rate and accumulated drift are lower than that of the contact modulus (0.0766 and 0.151, respectively). While contact depth does not correlate well with drift rate, there is only a 16 percent chance that the contact depth and accumulated drift were uncorrelated. The correlations were calculated using data from the 89 indentation tests performed at 1, 10, and 100 μN/s (including results from reference [60]).

Naturally, smaller total accumulated displacement drifts may not lead to abnormal curves but would still yield inaccurate data, due to variable drift rates. Long test times, which are more susceptible to varying drift rate, show a larger variation in both stiffnesses and contact moduli. The 1 uN/s loading rate had standard errors between 12 and 59 GPa, while the faster loading rates had standard errors that were less than 3 GPa. Additionally, for the faster loading rate tests, the standard error decreased as the maximum force increased because of a decrease in noise. For the slower loading rate test, the standard error increased with increasing force, suggesting an increased uncertainty in displacement measurements with time. This increased uncertainty in displacement would increase the uncertainty in the contact depth, contact area and stiffness, thus increasing uncertainty in the contact modulus. Moreover, these large-scale system displacement drifts cannot be eliminated by "continuous stiffness" measurement strategies [64-66] because of the need to measure the absolute position of the indenter tip reliably. While the continuous stiffness measurements may improve the reliability of the stiffness measurements by calculating the drift rate immediately prior to unloading, they cannot improve measurements of h_p, causing a large uncertainty in both contact area and contact modulus. The implications of these observations are crucial when evaluating the accuracy of instrumented indentation data. Drift rates that produce accumulated drift equal to or larger than the maximum tip displacement cannot be tolerated. Additionally, due to the variable nature of the drift rate, the raw data cannot be accurately corrected for long test times without further information about how the drift rate varies with temperature changes. While some studies disclose the displacement drift rate associated with their measurements, we have shown that the total accumulated drift as a fraction of the maximum penetration depth is a more appropriate indicator of data quality that should be explored during future standard development.

Max Force (μN)	Preload (μN)	Drift Measurement Time (s)	Drift Analysis Time (s)	Initial Drift Rate (nm/s)	Steady State Drift Rate (nm/s)	Difference in Drift Rates (nm/s)
0	1	60	30	0.0217	0.0287	0.0070
0	1	60	30	0.00180	0.0205	0.0187
0	1	60	30	-0.0168	-0.00537	0.0114
10	1	60	30	-0.0202	-0.0141	0.0061
10	1	60	30	-0.0208	-0.0187	0.0021
10	1	500	60	-0.0367	-0.0265	0.0102
10	1	500	60	-0.0409	-0.0383	0.0026
10	1	500	60	-0.0330	-0.0277	0.0053
10	2	60	30	-0.0329	-0.0110	0.0219
10	2	60	30	-0.0408	-0.0294	0.0114
10	2	60	30	-0.0462	-0.0444	0.0018
1	2	60	30	-0.0363	-0.0580	-0.0218
1	1	60	30	0.00361	0.0212	0.0176

Table 6-1 Initial and steady state drift rates for several long-term displacement drift measurement tests performed with varying maximum force, preload, drift measurement time and drift analysis time.

	Stiffness, S (µN/nm)	Contact Modulus, E^* (GPa)	Contact Depth, h_p (nm)
Drift Rate, $\dot{h}_{drift}$ (nm/s)	-0.207	-0.381	0.0766
Accumulated Drift at Start of Unloading, h_{drift} (nm)	-0.241	-0.495	0.151

Table 6-2 Correlation of drift related parameters to both stiffness and contact modulus.
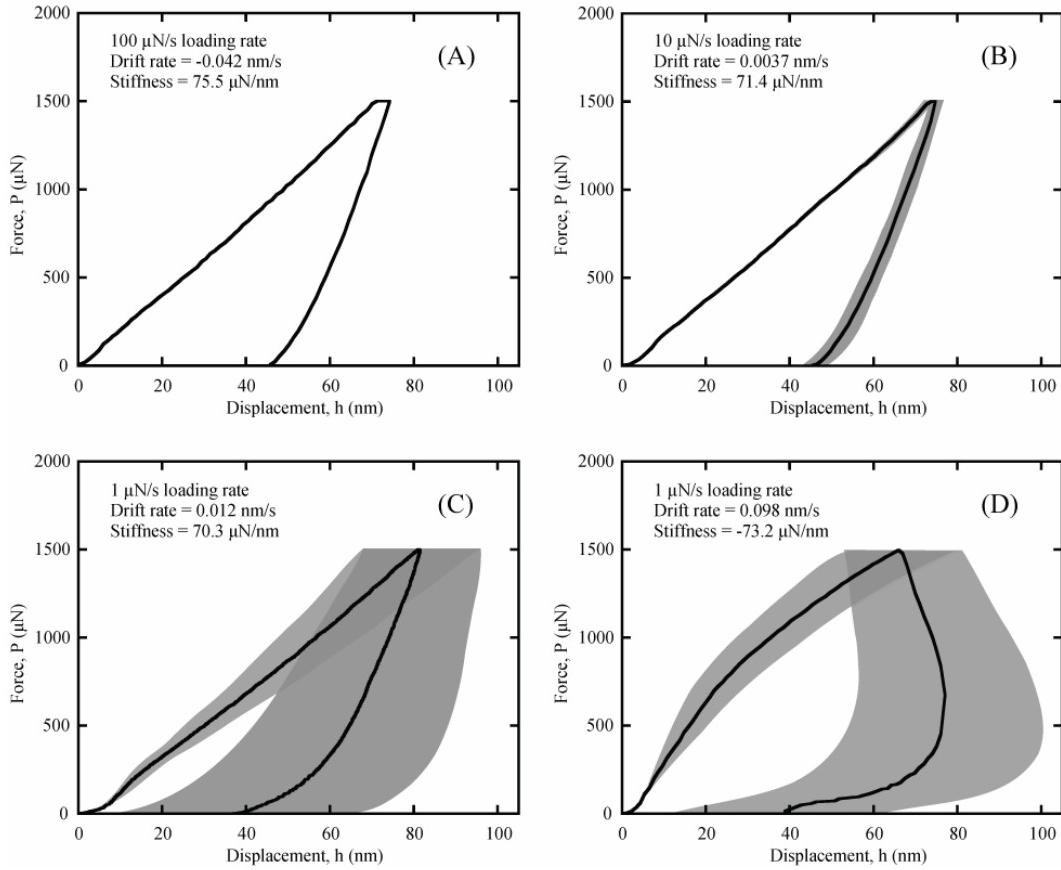
Figure 6-6 A representative force versus displacement curves for indents with a maximum load of 1500 μN: A.) 100 μN/s loading rate (MDR = -0.042 nm/s). B.) 10 μN/s loading rate (MDR = 0.0037 nm/s). C.) 1 μN/s loading rate with the smaller MDR (0.012 nm/s). D.) 1 μN/s loading rate with the high MDR (0.098 nm/s). Gray shading indicates uncertainty in displacement due to an estimated 0.01 nm/s MDR uncertainty. Uncertainty in force is within the line width.
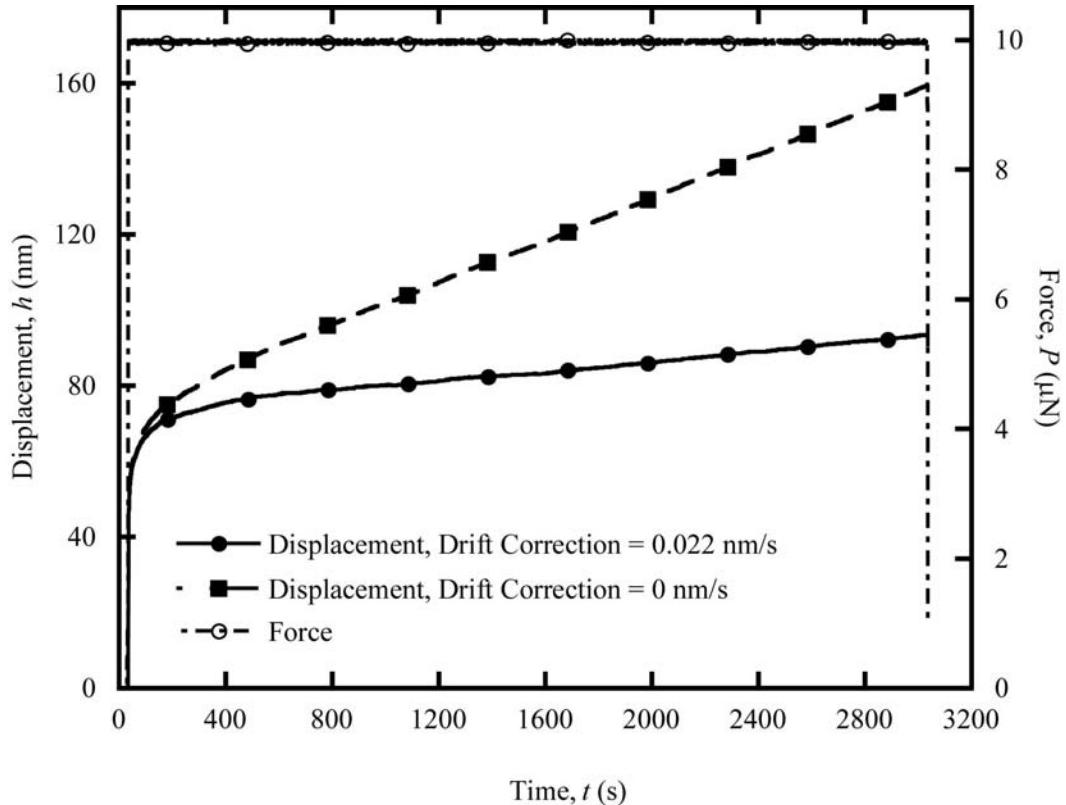
Figure 6-7 Displacement and force versus time for the drift measurement test. The solid symbols correspond to the left-hand axis (displacement), while the open symbols correspond to the right-hand axis (force). Displacement with the Triboscan drift correction rate of 0.022 nm/s is shown as closed circles with a solid line. Displacement with no drift correction rate (0 nm/s) is shown as closed squares with a dashed line. Force as a function of time is shown with open circles with a dashed-dotted line.
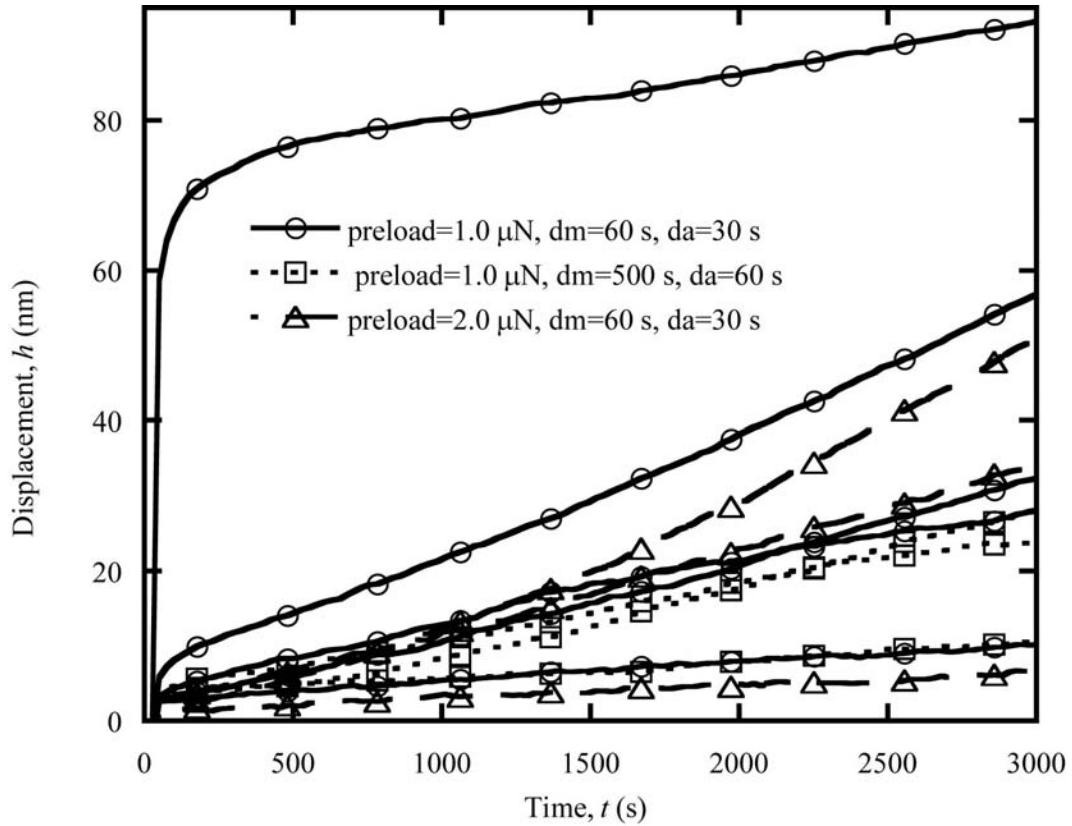
Figure 6-8 Displacement versus time for the drift measurement tests where the maximum force was 10 μN. The open circles with the solid lines correspond to tests where the preload for drift measurement was 1.0 μN, the drift monitoring (DM) time was 60 s, and the drift analysis (da) time was 30 s. The open square symbols with the dotted line shows tests where the preload was 1.0 μN, DM was 500 s, and DA was 60 s. The final line set with the open triangles and dashed lines are for tests where the preload was 2.0 μN, DM was 60 s, and DA was 30 s.
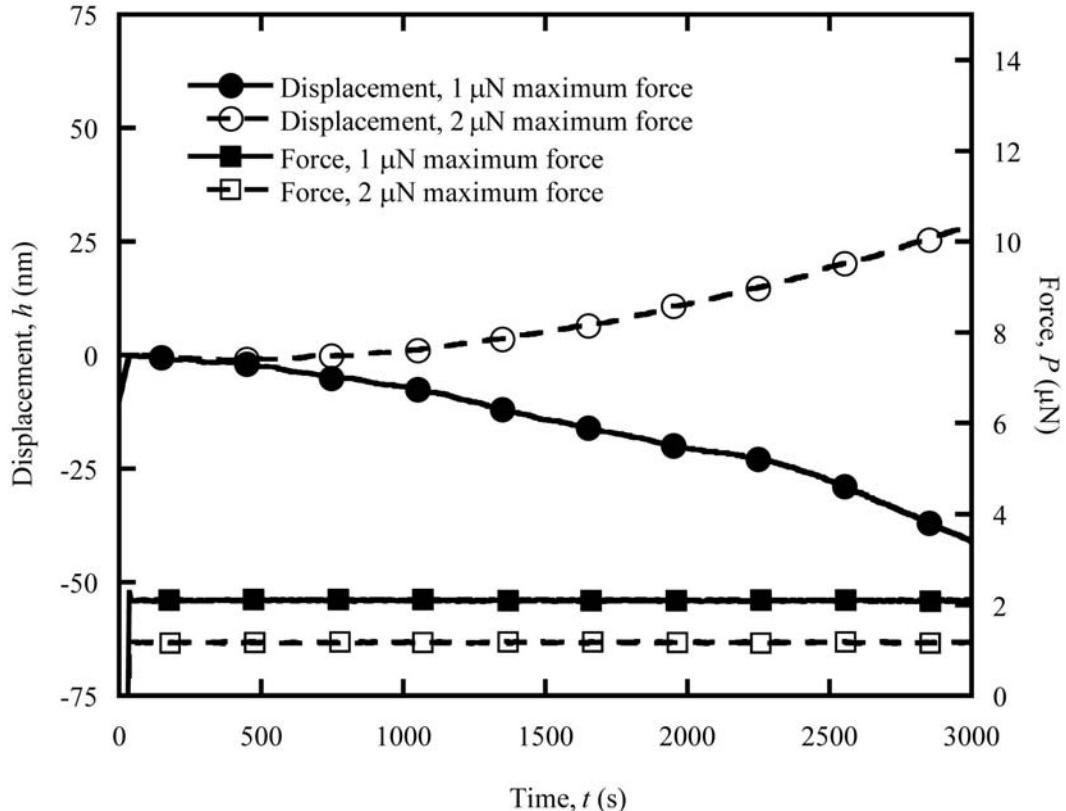
Figure 6-9 Displacement and force versus time for the drift measurement test at 1 and 2 μN maximum force. The circle symbols correspond to the left-hand axis (displacement), while the square symbols correspond to the right-hand axis (force). Both the displacement and force versus time plots for the 2.0 μN maximum force drift test are shown with solid lines and symbols, while the 1.0 μN maximum force drift test plots are shown with open symbols and dashed lines. For both tests, the drift rate is non-constant after 500 s.
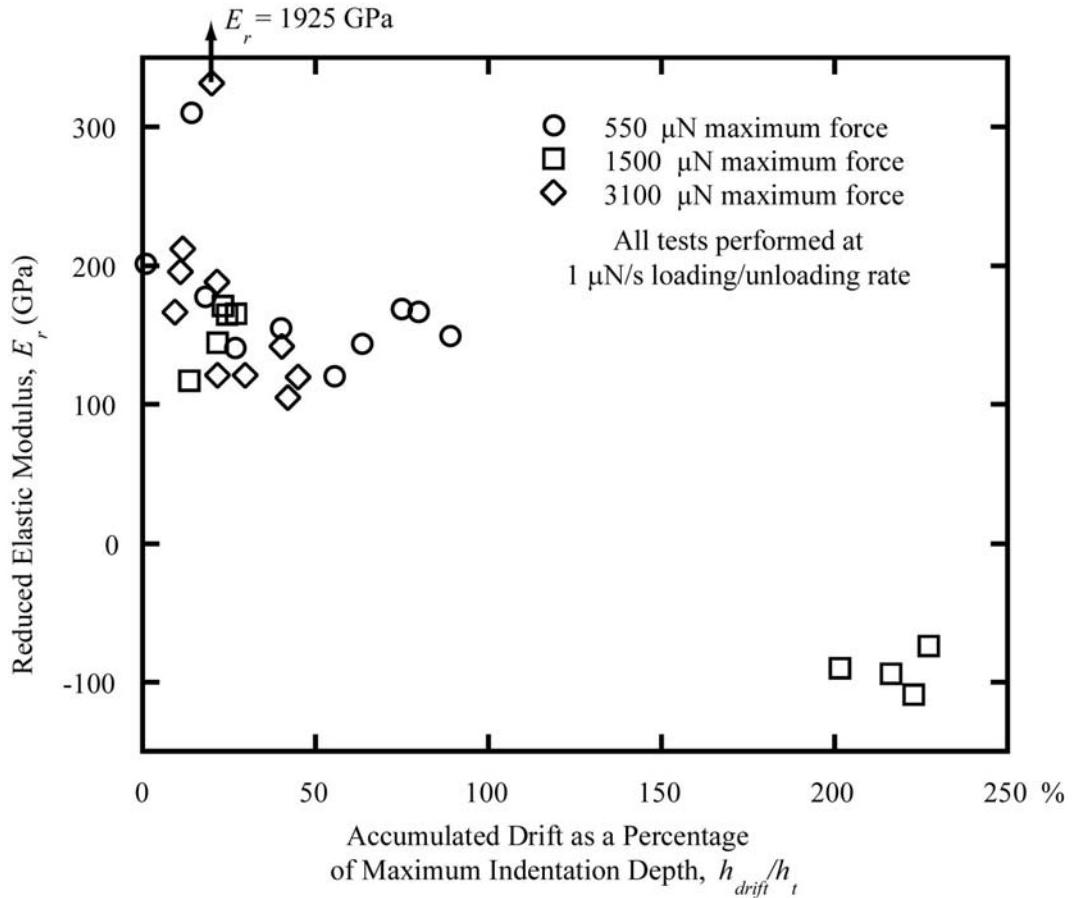
Figure 6-10 Reduced elastic modulus E_r as a function of the percent accumulated drift for a 1 μN/s loading and unloading rate test. The circles correspond to 550 μN maximum load, squares to 1500 μN, and diamonds to 3100 μN. The percent accumulated drift is the total accumulated drift over the maximum indentation depth, h_t. The total accumulated drift is calculated by taking the drift rate measured prior to the start of the test and multiplying that by the indentation test time to the start of unloading. This value assumes a constant drift rate over the entire test.

7   Nanoindentation Summary and Conclusions

Through symmetric and asymmetric tests, information was gained about the mechanical behavior of thin film platinum. The effect of factors such as material pile-up, anisotropy, microcracking and/or delamination, loading and unloading rates, and spatial variation were explored. Additionally, anomalous behavior in extremely slow loading rate tests (1 μN/s) prompted an examination of the role of drift in instrumented indentation and the subsequent induced error.

7.1   Mechanical behavior of thin film platinum

The deviation of the elastic properties of thin film metals from the behavior that would be expected based on anisotropic elasticity theory has been routinely reported. This work evaluated if additional control over experimental parameters and corrections during the analysis of the data could account for the anomalous response. Even after careful correction for pile-up and machine compliance during both the area function calibration and the indentation of the metallic film, platinum films were found to have regions where the reduced modulus (~181 GPa) was low compared to what would be expected based on anisotropic elasticity and indentation theories (~211 GPa). While the origins of this behavior are still unclear, it is apparent that the low elastic moduli of thin films measured during nanoindentation are not a result of shortfalls in the experimental technique. Other regions showed much higher reduced modulus (~221 GPa), above that predicted by anisotropic elasticity and indentation theories.   While the more compliant regions with low reduced moduli showed sensitivity to loading and unloading rate, the higher reduced moduli regions were much less affected by the loading and unloading rate. This suggests that the material has spatial variations within the material, which could be due to changes in surface chemistry and morphology, regions of substrate free platinum film, or localized processing effects.   In regions where there are low moduli, there may be a localized time dependent behavior of the material, such as grain coarsening, which is likely a result of anelastic, or reversible and linear viscoelastic, phenomena, since the load versus displacement curves show a loading rate dependency, but the residual indentation depths do not.

7.2   Drift methodology

When extremely slow loading rate tests (1 μN/s) were examined, six out of 30 tests showed anomalous behavior: some of the loading curves bulged outward and appeared abnormally stiff, and all of the unloading curves stiffnesses were either extremely small or negative, and thus non-physical. These anomalies could not be explained by anisotropy, pile-up, substrate constraint effects, or microcracking and/or delamination. Instead, system displacement drift was found to

be an important factor in the data quality of slow loading rate, long duration experiments. The drift rate was found to vary throughout experiments, and produced large uncertainties in the actual tip displacement value in the long term experiments. Additionally, since the drift rate varied, data cannot be corrected for drift for test times longer than the time constant, where the drift rate cannot be assumed as constant. For tests performed at room temperature without active temperature control, the time constant is frequently on the order of a few minutes, thus limiting acceptable test time and testing rates. More importantly, it was determined that accumulated drift as a percentage of maximum indentation depth was a good criterion for identifying reliable data. When the accumulated drift percentage was larger than 100 percent, the elastic moduli values were non-physical due to gross abnormalities in the force-displacement curves. It is likely that more stringent requirements will be necessary to insure that creep and strain-rate sensitivity results are accurate. The authors recommend the following for instrumented indentation tests:

1. Tests should be limited to be shorter than the temperature time constant to avoid variable drift rates

2. Tests longer than the temperature time constant cannot be accurately corrected for drift without further studies into how the drift rate changes with temperature

3. Tests with accumulated drift greater than 100 percent of the maximum indentation depth produce unreliable results and should be discarded, even if the drift rates are within standard acceptable limits (less than 0.1 nm/s)

4. Continuous stiffness approaches do not completely solve the problem of variable drift rates, since actual tip displacement, and therefore contact depth, cannot be accurately known.

8   References

1.   Speidel, M.O., *Resistance to Fatigue Crack Growth of the Platinum Metals.* Platinum Metals Review, 1981. **25**(1): p. 24-31.
2.   *MinCryst - Crystallographic and Crystallochemical Database for Minerals and their Structural Analogues.* 2008 [cited; Available from: http://database.iem.ac.ru/mincryst/s_carta.php?PLATINUM+3719.
3.   Wilson, R.G., F.A. Stevie, and C.W. Magee, *Secondary Ion Mass Spectroscopy*. 1989: John Wiley & Sons.
4.   *E 647 - Standard Test Method for Measurement of Fatigue Crack Growth Rates*, in *ASTM Standards*. 2005.
5.   Laura, P.A., J.A. Reyes, and R.E. Rossi, *Numerical experiments on the determination of stress concentration factors.* Strain, 1974. **10**(2): p. 58-61.
6.   Tada, H., P.C. Paris, and G.R. Irwin, *The stress analysis of cracks handbook*. 2000, New York: ASME Press.
7.   Ritchie, R.O., *Mechanisms of fatigue-crack propagation in ductile and brittle solids.* International Journal of Fracture, 1999. **100**(1): p. 55-83.
8.   Suresh, S., *Fatigue of Materials*. Second ed. 1998: Cambridge University Press.
9.   Romasco, A., *Nanoindentation of Platinum Thin Films*, R. Meirom, Editor. 2008.
10.   Sharpe, W.N., Jr., *ARO Symposium #3*. 2006.
11.   Callister, W.D.J., *Materials Science and Engineering, An Introduction*. Seventh Edition ed. 2007: John Wiley & Sons, Inc.
12.   Agnew, S.R., et al., *Microstructure and mechanical behavior of nanocrystalline metals.* NSF Symposium on Micromechanic Modeling of Industrial Materials: In Honor of the 65th Birthday of Professor T. Mori, Jul 20-Jul 22 1998, 2000. **285**(1): p. 391-396.
13.   Lin, H.T., et al., *Characterization of erosion and failure processes of spark plugs after field service in natural gas engines.* 15th International Conference on Wear of Materials, 2005. **259**(7-12): p. 1063-1067.
14.   Hugo, R.C., et al., *In-situ TEM tensile testing of DC magnetron sputtered and pulsed laser deposited Ni thin films.* Acta Materialia, 2003. **51**(7): p. 1937-43.
15.   Christ, H.-J., *On the orientation of cyclic-slip-induced intergranular fatigue cracks in face-centred cubic metals.* Materials Science & Engineering A: Structural Materials: Properties, Microstructure and Processing, 1989. **A117**(1-2): p. 25-29.
16.   Liang, F.-L. and C. Laird, *Control of intergranular fatigue cracking by slip homogeneity in copper. II. Effect of loading mode.* Materials Science & Engineering A (Structural Materials: Properties, Microstructure and Processing), 1989. **A117**: p. 103-13.
17.   Liang, F.-L. and C. Laird, *Control of intergranular fatigue cracking by slip homogeneity in copper. I. Effect of grain size.* Materials Science & Engineering A (Structural Materials: Properties, Microstructure and Processing), 1989. **A117**: p. 95-102.
18.   Zhang, Z.F. and Z.G. Wang, *Dependence of intergranular fatigue cracking on the interactions of persistent slip bands with grain boundaries.* Acta Materialia, 2003. **51**(2): p. 347-64.
19.   Liu, W., et al., *Crystallographic features of intergranular crack initiation in fatigued copper polycrystals.* Acta Metallurgica et Materialia, 1992. **40**(7): p. 1763-71.
20.   Tromans, D. and S. Ruhong1, *Intergranular/transgranular fatigue of copper: influence of environment on crack path and propagation rates.* Materials Science & Engineering A (Structural Materials: Properties, Microstructure and Processing), 1996. **A219**(1-2): p. 56-65.
21.   Yim, T.H., S.C. Yoon, and H.S. Kim, *Tensile properties of electrodeposited nanocrystalline nickel.* Proceedings of the 12th International Conference on Rapidly Quenched & Metastable Materials, 2007. **449-451**: p. 836-840.

22.   Wang, L. and B.C. Prorok, *Characterization of the strain rate dependent behavior of nanocrystalline gold films.* Journal of Materials Research, 2008. **23**(1): p. 55-65.

23.   Noskova, N.I., *Deformation of nanocrystalline pure metals and alloys based on Fe and Al.* Journal of Alloys and Compounds, 2007. **434-435**(SPEC ISS): p. 307-310.

24.   Nieman, G.W., J.P. Weertman, and R.W. Siegel, *Mechanical behavior of nanocrystalline metals.* Nanostructured Materials, 1992. **1**(2): p. 185.

25.   Caruana, D.J. and J.V. Bannister, *Surface properties of fractured and polished platinum microelectrodes.* Journal of Electroanalytical Chemistry, 1997. **424**(1-2): p. 197-205.

26.   Taylor, J.R., *An Introduction to Error Analysis : the Study of Uncertainties in Physical Measurements* 2nd ed. 1997, Sausalito, California: University Science Books.

27.   Jaluria, Y., *Computer methods for engineering*. 1996, Washington, DC: Taylor & Francis.

28.   *Corning 1737 AMLCD Glass Substrates: Material Information*. 2004, Corning.

29.   Oliver, W.C. and G.M. Pharr, *Measurement of hardness and elastic modulus by instrumented indentation: Advances in understanding and refinements to methodology.* Journal of Materials Research, 2004. **19**(1): p. 3-20.

30.   Simmons, G. and H. Wang, *Single Crystal Elastic Constants and Calculated Aggregate Properties: A Handbook*. 1971, Cambridge, MA: The M.I.T. Press.

31.   Vlassak, J.J. and W.D. Nix, *Indentation modulus of elastically anisotropic half spaces.* Philosophical Magazine A (Physics of Condensed Matter, Defects and Mechanical Properties), 1993. **67**(5): p. 1045-56.

32.   Vlassak, J.J. and W.D. Nix, *Measuring the elastic properties of anisotropic materials by means of indentation experiments.* Journal of the Mechanics and Physics of Solids, 1994. **42**(8): p. 1223-1245.

33.   Lee, K.W., et al., *An international round-robin experiment to evaluate the consistency of nanoindentation hardness measurements of thin films.* Surface and Coatings Technology, 2003. **168**(1): p. 57-61.

34.   Lee, H., et al., *Characterization of metal and metal alloy films as contact materials in MEMS switches.* Journal of Micromechanics and Microengineering, 2006. **16**(3): p. 557-563.

35.   Swain, M.V. and J. Mencik, *Mechanical property characterization of thin-films using spherical tipped indenters.* Thin Solid Films, 1994. **253**(1-2): p. 204-211.

36.   Mencik, J. and M.V. Swain. *Mechanical properties of platinum films on silicon and glass determined by ultra-microindentation*. 1995. Boston, MA, USA: Materials Research Society, Pittsburgh, PA, USA.

37.   Sharpe, W., C. Muhlstein, Editor. 2008.

38.   Hyun, S., O. Kraft, and R.P. Vinci, *Mechanical behavior of Pt and Pt-Ru solid solution alloy thin films.* Acta Materialia, 2004. **52**(14): p. 4199-4211.

39.   Gao, H., C.-H. Chiu, and J. Lee, *Elastic contact versus indentation modeling of multi-layered materials.* International Journal of Solids and Structures, 1992. **29**(20): p. 2471-2492.

40.   Doerner, M.F. and W.D. Nix, *A method for interpreting the data from depth-sensing indentation instruments.* Journal of Materials Research, 1986. **1**(4): p. 601-9.

41.   Han, S.M., R. Saha, and W.D. Nix, *Determining hardness of thin films in elastically mismatched film-on-substrate systems using nanoindentation.* Acta Materialia, 2006. **54**(6): p. 1571-1581.

42.   Fischer-Cripps, A.C., ed. *Nanoindentation*. 2nd ed. Mechanical Engineering Series, ed. F.F. Ling. 2004, Springer-Verlag: New York. 1-263.

43.   Tabor, D., *The Hardness of Metals*. Monographs on the Physics and Chemistry of Materials, ed. W. Jackson, H. Frohlich, and N.F. Mott. 1951, New York: Oxford University Press.

44. Lu, L., et al., *Nano-sized twins induce high rate sensitivity of flow stress in pure copper.* Acta Materialia, 2005. **53**(7): p. 2169-2179.

45. Schwaiger, R., et al., *Some critical experiments on the strain-rate sensitivity of nanocrystalline nickel.* Acta Materialia, 2003. **51**(17): p. 5159-5172.

46. Jayaganthan, R., K. Mohankumar, and A.A.O. Tay, *Nanoindentation study of nanocrystalline nickel.* International Journal of Nanoscience, 2005. **4**(2): p. 197-205.

47. Gu, C.D., et al., *Experimental and modelling investigations on strain rate sensitivity of an electrodeposited 20 nm grain sized Ni.* Journal of Physics D: Applied Physics, 2007. **40**(23): p. 7440-7446.

48. Mueller, J., et al. *Local investigations of the mechanical properties of ultrafine grained metals by nanoindentations.* 2006. Fukuoka, Japan: Trans Tech Publications Ltd, Stafa-Zuerich, CH-8712, Switzerland.

49. Meirom, R.A., et al., *Velocity-dependent fatigue crack paths in nanograined Pt films.* 2008.

50. Ngan, A.H.W., et al., *Correcting power-law viscoelastic effects in elastic modulus measurement using depth-sensing indentation.* International Journal of Solids and Structures, 2005. **42**(5-6): p. 1831-1846.

51. Fischer-Cripps, A.C., *A simple phenomenological approach to nanoindentation creep.* Materials Science and Engineering A, 2004. **385**(1-2): p. 74-82.

52. Ogbonna, N., N.A. Fleck, and A.C.F. Cocks, *Transient creep analysis of ball indentation.* International Journal of Mechanical Sciences, 1995. **37**(11): p. 1179-1202.

53. Meirom, R.A. and C.L. Muhlstein. 2009.

54. Jin, M., et al., *Study of deformation behavior of ultrafine-grained materials through in situ nanoindentation in a transmission electron microscope.* Journal of Materials Research, 2005. **20**(7): p. 1735-1740.

55. Gai, P.L., K. Zhang, and J. Weertman, *Electron microscopy study of nanocrystalline copper deformed by a microhardness indenter.* Scripta Materialia, 2007. **56**(1): p. 25-28.

56. Zhang, K., J.R. Weertman, and J.A. Eastman, *Rapid stress-driven grain coarsening in nanocrystalline Cu at ambient and cryogenic temperatures.* Applied Physics Letters, 2005. **87**(6): p. 061921.

57. Brandstetter, S., et al., *Grain coarsening during compression of bulk nanocrystalline nickel and copper.* Scripta Materialia, 2008. **58**(1): p. 61-64.

58. Jin, M., A.M. Minor, and J.W. Morris Jr, *Strain-induced coarsening in nano-grained films.* Thin Solid Films, 2007. **515**(6): p. 3202-3207.

59. Tsui, T.Y., W.C. Oliver, and G.M. Pharr, *Influences of stress on the measurement of mechanical properties using nanoindentation: Part I. Experimental studies in an aluminum alloy.* Journal of Materials Research, 1996. **11**(3): p. 752-759.

60. Romasco, A., et al., *Deformation behavior of nanograined platinum films.* 2008.

61. Bouzakis, K.D., et al., *The effect of specimen roughness and indenter tip geometry on the determination accuracy of thin hard coatings stress-strain laws by nanoindentation.* Materials Characterization, 2002. **49**(2): p. 149-156.

62. Kim, J.-Y., et al., *Influence of surface-roughness on indentation size effect.* Acta Materialia, 2007. **55**(10): p. 3555-3562.

63. Walter, C., et al., *Finite element simulation of the effect of surface roughness on nanoindentation of thin films with spherical indenters.* Surface and Coatings Technology, 2007. **202**(4-7): p. 1103-1107.

64. Rar, A., et al. *On the measurement of creep by nanoindentation with continuous stiffness techniques.* 2005. Boston, MA, United States: Materials Research Society, Warrendale, PA 15086, United States.

65. Li, X. and B. Bhushan, *A review of nanoindentation continuous stiffness measurement technique and its applications.* Materials Characterization, 2002. **48**(1): p. 11-36.

66.   Syed Asif, S.A. and J.B. Pethica. *Proceedings of the 1996 MRS Spring Meeting*. 1996. San Francisco, CA, USA.